Aus dem Pathologischen Institut der

Ludwig-Maximilians-Universität München

Direktor: Prof. Dr. med. Frederick Klauschen

in der DKTK-Arbeitsgruppe „Oncogenic Signaling Pathways in Colorectal and Pancreatic Cancer"

Leiter: Dr. rer. nat. Peter Jung

Dissertation

zum Erwerb des Doctor of Philosophy (Ph.D.)

an der Medizinischen Fakultät der

Ludwig-Maximilians-Universität München

Disease modeling on tumor organoids implicates AURKA as a therapeutic target in liver metastatic colorectal cancer

---

vorgelegt von

Sophie Luise Boos

aus Gehrden, Deutschland

im Jahr 2021

Gedruckt mit der Genehmigung der Medizinischen Fakultät

der Ludwig-Maximilians-Universität München

Erstgutachter: Prof. Dr. rer. nat. Heiko Hermeking

Zweitgutachter: Dr. rer. nat. Peter Jung

Dekan: Prof. Dr. med. Thomas Gudermann

Tag der mündlichen Prüfung: 06.12.2021

To everyone who supported me.

Affidavit

Boos, Sophie Luise
Thalkirchner Str. 36
80337 Munich
Germany

I hereby declare that the submitted thesis entitled

"Disease modeling on tumor organoids implicates AURKA as a therapeutic target in liver metastatic colorectal cancer"

is my own work. I have only used the sources indicated and have not made unauthorized use of services of a third party. Where the work of others has been quoted or reproduced, the source is always given.
I further declare that the submitted thesis or parts thereof have not been presented as part of an examination degree to any other university.

Munich, 12.12.2021	Sophie Luise Boos
Place, date	Signature doctoral candidate

Confirmation of congruency between printed and electronic version of the doctoral thesis

Boos, Sophie Luise
Thalkirchner Str. 36
80337 Munich
Germany

I hereby declare that the electronic version of the submitted thesis, entitled

"Disease modeling on tumor organoids implicates AURKA as a therapeutic target in liver metastatic colorectal cancer"

is congruent with the printed version both in content and format.

Munich, 12.12.2021	Sophie Luise Boos
Place, date	Signature doctoral candidate

Publications

The results of this thesis have been submitted and accepted for revision:

Sophie L. Boos, Leon P. Loevenich, Sebastian Vosberg, Thomas Engleitner, Rupert Oellinger, Jörg Kumbrink, Marlies Michl, Philipp A. Greif, Andreas Jung, Heiko Hermeking, Jens Neumann, Thomas Kirchner, Roland Rad, Peter Jung. 2021. "Disease modeling on tumor organoids implicates AURKA as a therapeutic target in liver metastatic colorectal cancer." CMGH

In addition, I contributed to the following articles, which are not further described here:

Dietinger, Vanessa, Cira R. García de Durango, Svenja Wiechmann, **Sophie L. Boos**, Marlies Michl, Jens Neumann, Heiko Hermeking, Bernhard Kuster, and Peter Jung. 2020. "Wnt-Driven LARGE2 Mediates Laminin-Adhesive O-Glycosylation in Human Colonic Epithelial Cells and Colorectal Cancer." Cell Communication and Signaling 18(1):102. doi: 10.1186/s12964-020-00561-6.

Baumann, Daniel, Tanja Hägele, Julian Mochayedi, Jennifer Drebant, Caroline Vent, Sven Blobner, Julia Han Noll, Irena Nickel, Corinna Schumacher, **Sophie Luise Boos**, Aline Sophie Daniel, Susann Wendler, Michael Volkmar, Oliver Strobel, and Rienk Offringa. 2020. "Proimmunogenic Impact of MEK Inhibition Synergizes with Agonist Anti-CD40 Immunostimulatory Antibodies in Tumor Therapy." Nature Communications 11(1):2176. doi: 10.1038/s41467-020-15979-2.

Brandl, Lydia, Yina Zhang, Nina Kirstein, Andrea Sendelhofert, **Sophie Luise Boos**, Peter Jung, Florian Greten, Roland Rad, and Antje Menssen. 2019. "Targeting C-MYC through Interference with NAMPT and SIRT1 and Their Association to Oncogenic Drivers in Murine Serrated Intestinal Tumorigenesis." Neoplasia 21(10):974–88. doi: 10.1016/j.neo.2019.07.009.

Jaeckel, Stephanie, Markus Kaller, Rene Jackstadt, Ursula Götz, Susanna Müller, **Sophie Boos**, David Horst, Peter Jung, and Heiko Hermeking. 2018. "Ap4 Is Rate Limiting for Intestinal Tumor Formation by Controlling the Homeostasis of Intestinal Stem Cells." Nature Communications 9(1):3573. doi: 10.1038/s41467-018-06001-x.

Lubeseder-Martellato, Clara, Katharina Alexandrow, Ana Hidalgo-Sastre, Irina Heid, **Sophie Luise Boos**, Thomas Briel, Roland M. Schmid, and Jens T. Siveke. 2017. "Oncogenic KRas-Induced Increase in Fluid-Phase Endocytosis Is Dependent on N-WASP and Is Required for the Formation of Pancreatic Preneoplastic Lesions." EBioMedicine 15:90–99. doi: 10.1016/j.ebiom.2016.12.013.

Table of contents

List of abbreviations

5-FU	5-fluorouracil
AfaSel	Afatinib + Selumetinib
APC	Adenomatous polyposis coli
APC/C	Anaphase promoting complex/cyclosome
AURKA	Aurora kinase A
AURKB	Aurora kinase B
AURKC	Aurora kinase C
bp	Base pair
cDNA	Complementary DNA
CI	Confidence interval
CIMP	CpG island methylator phenotype
CIN	Chromosomal instability
CK1	Casein kinase 1
Cmab	Cetuximab
CNA	Copy number alteration
COAD	Colorectal adenocarcinoma
CRC	Colorectal cancer
CRISPR	Clustered regularly interspaced short palindromic repeats
crRNA	CRISPR-RNA
CTNNB1	Catenin beta 1, gene encoding β-catenin
CT-PDTO	Chemotherapy tolerant PDTOs
CT-PDTO eKRAS	Chemotherapy tolerant PDTOs with CRISPR/Cas9-mediated genetically engineered KRAS
DKFZ	German Cancer Research Center
DLL4	Delta like canonical Notch ligand 4
DMEM	Dulbecco's modified eagle medium
DMSO	Dimethylsulfoxide
dNTP	Deoxynucleotidetriphophates
DTT	Dithiothreitol
dUTP	Deoxyuridine triphosphate
EDTA	Ethylenediaminetetraacetic acid
EdU	5-ethynyl-2'-deoxyuridine
EE	Enteroendocrine cell
EGF	Epidermal growth factor
EGFR	Epidermal growth factor receptor
eKRAS	CRISPR/Cas9-mediated genetically engineered KRAS
EN medium	EGF and noggin-containing medium
ERBB	Erythroblastic oncogene B
ERK	Extracellular-signal regulated kinase
FACS	Fluorescence-activated cell sorting
FBS	Fetal bovine serum
FDR	False discovery rate
FdUMP	Fluorodeoxyuridine monophosphate

FdUTP	Fluoro-deoxyuridine triphosphate
FFPE	Formalin-fixed and paraffin embedded
FGFR1	Fibroblast growth factor receptor 1
FLT1	Fms related receptor tyrosine kinase 1
FPKM	Fragments per kilobase million
FOLF	Folinic acid, 5-fluorouracil
FOLFIRI	Folinic acid, 5-fluorouracil, Irinotecan or folinic acid, 5-fluorouracil, SN-38
FOLFOX	Folinic acid, 5-fluorouracil, Oxaliplatin
FUTP	Fluorouridine triphosphate
FZD	Frizzled
GDC	National Cancer Institute's Genomic Data Commons
GSEA	Gene set enrichment analysis
GSK3	Glycogen synthase kinase
HE	Hematoxylin-eosin
HER	Human epidermal growth factor receptor
HRP	Horseradish peroxidase
IHC	Immunohistochemistry
INDEL	Insertion or deletion
IQR	Interquartile range
ISC	Intestinal stem cell
kDa	Kilo dalton
KRAS	Kirsten rat sarcoma
LB	Lysogeny broth
LMU	Ludwig-Maximilians-University
LRP	Low density lipoprotein receptor related protein
LV	Leucovorin
M0	Non-metastatic
M1-HEP	Exclusive liver metastatic
M1-PUL	Exclusive lung metastatic
MAPK	Mitogen-activated protein kinase
MAPKK	Mitogen-activated protein kinase kinases, also known as MEK
mCRC	Metastatic colorectal cancer
MLH	MutL homolog 1
MMR	Mismatch repair
MSH	MutS homolog
MSI	Microsatellite instability
MSigDB	Molecular Signatures Database
MSS	Microsatellite stability
mTOR	Mechanistic target of rapamycin
mut	Mutant
n	Replicate number
NM	Normal mucosa of the colon
NM-D	Patient-derived organoids of normal colonic mucosa, under differentiation-inducing culture conditions

NM-S	Patient-derived organoids of normal colonic mucosa, under stemness-inducing culture conditions
OLFM4	Olfactomedin 4
PAGE	Polyacryamide gel electrophoresis
PAM	Protospacer adjacent motif
PARP	Poly-(ADP-ribose)-polymerase
PBS	Phosphate-buffered saline
PCR	Polymerase chain reaction
PDTO	Patient-derived tumor organoid
PGE2	Prostaglandine E2
PI3K	Phosphatidyl-inositol 3 kinase
PIK3CA	Phosphatidyl-inositol 3 kinase catalytic subunit α
PMSF	Phenylmethylsulfonyl fluoride
POLE	Polymerase ε
PROTAC	Proteolysis targeting chimera
qRT-PCR	Quantitative real time polymerase chain reaction
RAF	Rapidly accelerated fibrosarcoma
RAS	Rat sarcoma
READ	Rectal adenocarcinoma
RIPA	Radioimmunoprecipitation assay
RNP	Ribonucleoprotein
RTCA	Real-time cell analyzer
SD	Standard Deviation
SDS	Sodium dodecyl sulfate
SNV	Single nucleotide variant
TA	Transit amplifying cell
TBS	Tris-buffered saline
TBS-T	Tris-buffered saline with Tween20
TCF	T cell factor
TCGA	The Cancer Genome Atlas
TEAD2	TEA domain transcription factor 2
TEMED	Tetramethylethylendiamin
TGFBR2	TGF-β receptor 2
TGF-α	Transforming growth factor alpha
TP53	Tumor protein p53
tracrRNA	Trans-activating crRNA
Tris	Tris(hydroxymethyl)aminomethane
TSO	Template switch oligo
UMI	Unique molecular identifiers
VEGF	Vascular endothelial growth factor
VUS	Variant of unknown significance
WES	Next generation whole exome sequencing
WREN medium	Wnt, R-spondin, EGF, noggin containing medium
wt	Wild type

List of figures

List of tables

1 Introduction

1.1 Cancer

With almost 10 million cancer-related deaths in 2020 worldwide[1], this class of diseases is the second leading cause of deaths and has become a major health problem[2].

On a molecular level, primary tumors are of monoclonal origin and develop when a cell accumulates genetic defects that allows it to proliferate uncontrollably[3]. In 2000, Hanahan and Weinberg compiled six hallmarks of cancer that are necessary for tumor development and maintenance[4]. These include a sustained tumor cell intrinsic proliferate signaling, resistance against cell death, and activation of invasion and metastasis promoting features[4]. A decade later, Hanahan and Weinberg updated their groundbreaking review and added two more hallmarks, the deregulation of cellular energetics and the avoidance of the immune destruction, as well as two "enabling characteristics" that allow the generation of the hallmarks: genomic instability and tumor promoting inflammation[3]. Together, these ten characteristics of cancers build the fundament for tumor growth and progression (Figure 1).

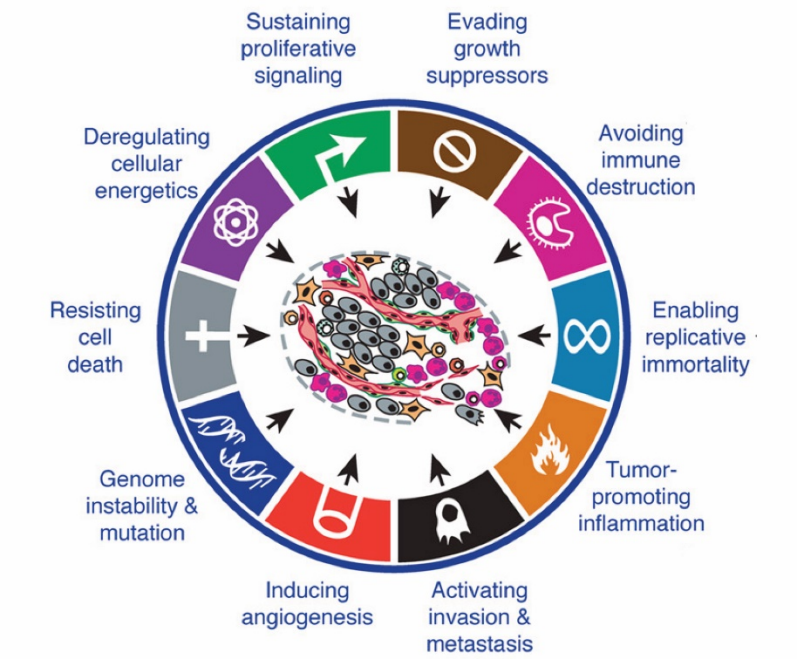

Figure 1: The hallmarks of cancer

Hanahan and Weinberg described the hallmarks of cancers that enable the development and maintenance of tumors. Figure is taken and adjusted from Hanahan and Weinberg[3].

1.2 Colorectal cancer

Even though the treatment of colorectal cancer (CRC) has improved considerably in the last decade, it remains a major health issue as therapy resistance and metastasis formation limit the success of therapy[5,6]. It was the cancer with the third-highest number of new cases (Figure 2A) and the second-highest cause of cancer-related deaths worldwide in 2020[1] (Figure 2B). Incidence and mortality are higher in males than females[1].

With 70 – 80 % of cases, the majority of CRCs develop sporadically, which signifies that they do not have a hereditary component but develop spontaneously. In addition, approximately 2 % develop as a consequence of inflammatory bowel disease[7]. The remaining 20 – 30 % of CRCs are hereditary forms, partly due to Lynch syndrome (also known as hereditary non-polyposis colorectal cancer syndrome) or familial adenomatous polyposis, making a family history of CRC a major risk factor[8]. Other risk factors for the development of CRC include age[9] as well as lifestyle and dietary choices such as alcohol abuse[10], obesity[11], and the consumption of red meat[12,13].

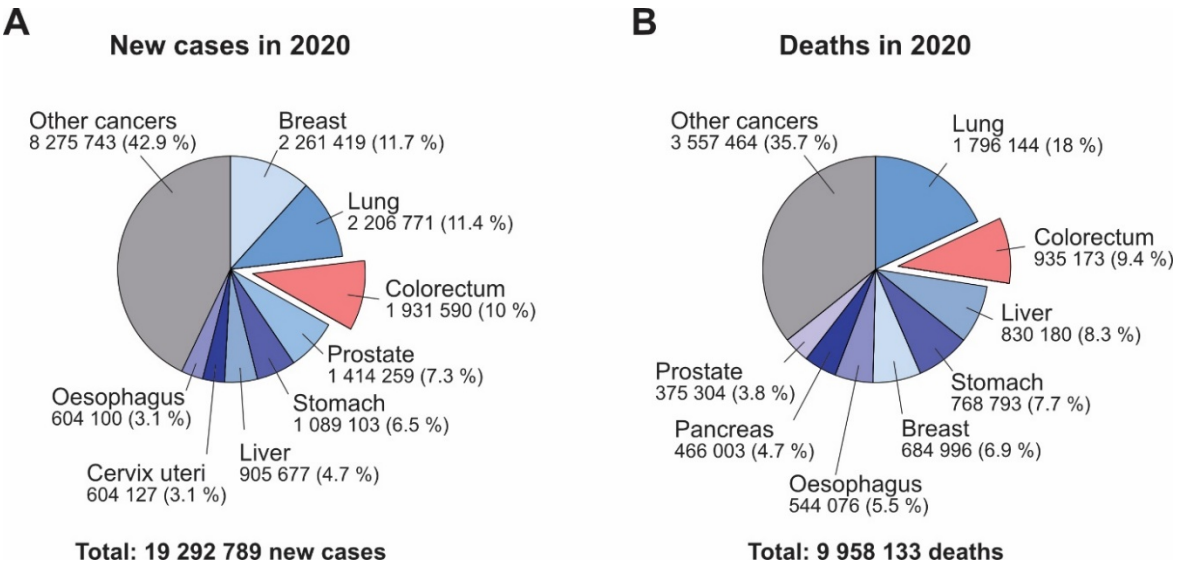

Figure 2: New cancer cases and deaths in 2020

New cancer cases and cancer deaths according to tumor entities in 2020, worldwide. Numbers are taken from Sung *et al.*[1] based on the GLOBOCAN estimates produced by the International Agency for Research on Cancer / World Health Organization.

1.2.1 Stages of colorectal cancer

Abnormal growth of colorectal cells can be divided into the precursor lesion carcinoma *in situ* and four stages of CRC[14].

The carcinoma *in situ* is sometimes also referred to as stage 0, where cancer cells accumulate in the innermost layer of the colorectum, the mucosa. Stage I CRCs are restricted to the submucosa or the underlying muscle layer of the colorectal wall but have not spread to lymph nodes or any other organs. Stage II CRCs are characterized by growth through the colorectal wall and potentially into neighboring organs. If the CRC has spread to nearby lymph nodes, it is classified as stage III. Stage IV CRCs have metastasized to distant organs, most commonly the liver and lung[14].

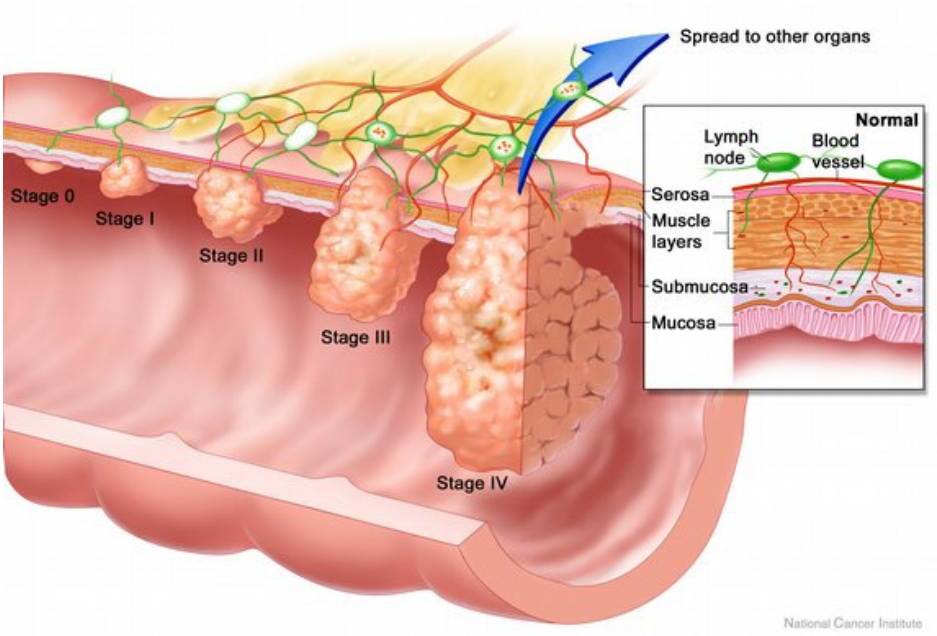

Figure 3: Stages of colorectal cancer

The stages of colorectal cancer (CRC). Stage 0: restriction to the mucosa of the colorectum, stage I: restriction to the submucosa or underlying muscle layer, stage II: colorectal wall and neighboring organs are affected, stage III: spread to local lymph nodes, stage IV: metastasis to distant organs. Figure was derived from Sinkovics[15].

1.3 The human intestine

The human intestine extends from the pyloric sphincter of the stomach to the anus and can be divided into the small intestine (upper intestine) and the large intestine (lower intestine)[16]. The small intestine consists of the duodenum, jejunum, and ileum while the large intestine is made up of the caecum, colon, rectum, and anal canal[16].

The main tasks of the intestine are the digestion and absorption of nutrients and water as well as the production of mucus and antimicrobial substances[16]. Mammalian evolution has selected a set of strategies that increase the surface of the intestine for more efficient nutrient uptake. One is the formation of invaginations of the columnar epithelium into the underlying lamina propria, which leads to the formation of crypts. These are also called crypts of Lieberkühn, after their discoverer Johann Lieberkühn (1711 – 1756). Besides the crypts, the small intestine also contains villi, which are protrusions of the epithelium and the lamina propria into the intestinal lumen (Figure 4)[16].

At the bottom of the crypts reside self-renewing, multipotent stem cells that constantly repopulate the upper crypt compartments and thereby renew them every four to five days. The stem cells divide to give rise to transit amplifying cells, which are localized in the compartment above the stem cells and proliferate faster. They divide four to five times to spawn daughter cells that terminally differentiate into the specialized cell types of the intestine while moving up the crypt. Once these cells reach the lumen of the intestine, they undergo apoptosis and are shed into the lumen of the intestine[17,18].

The most common cell of the intestinal epithelium is the enterocyte, which is responsible for the uptake of nutrients (glucose, amino acids, and fatty acids) and water. Interspersed are goblet cells that produce mucins and at a lower frequency enteroendocrine cells for the secretion of hormones such as serotonin[16].

Besides the presence or absence of villi, there is one other major difference between the small and large intestine, which are otherwise very similar in their architecture: in the small intestine, a second population of cells is interspersed between the stem cells at the bottom of the crypts, the so-called Paneth cells. These cells play an important role in the innate immune system since they secrete antimicrobial enzymes such as lysozyme and α-defensine[16]. Moreover, they are in direct contact with the stem cells and help to maintain their stem cell properties by producing niche factors such as epidermal growth factor (EGF), transforming growth factor alpha (TGF-α), WNT3, and the NOTCH ligand DLL4 (delta like canonical Notch ligand 4)[19].

High Wnt signaling in the base of the crypts maintains the stem cell phenotype and drives proliferation. For instance, inhibition of the Wnt pathway by homozygous deletion of the T cell factor 4 (Tcf4) in mice[20], the depletion of the β-catenin gene *Ctnnb1* in the epithelium of the small intestine[21], or adenoviral expression of the Wnt inhibitor Dickkopf-1[22] leads to no or reduced proliferation. In contrast, hyperactivation of the Wnt pathway by transgenic expression of the Wnt agonist R-Spondin-1 induces hyperproliferation of intestinal crypts[23].

Moving upwards the crypt, the Wnt signaling activity decreases, which allows the differentiation of progenitors into the other specialized cell types[17]. One exception are the Paneth cells that differentiate upon the high Wnt signaling in the crypt base[24].

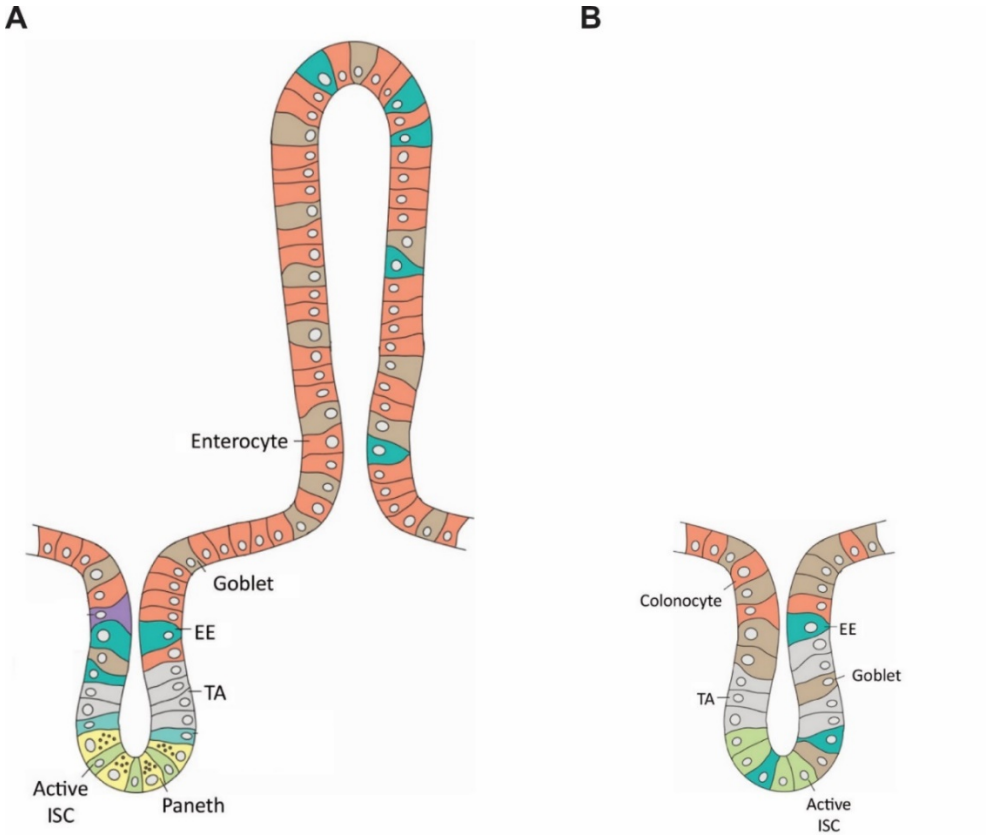

Figure 4: Schematic of the intestinal epithelium

A) Crypt and villus of the small intestine. **B)** Crypt of the large intestine. **A, B)** ISC: intestinal stem cell, TA: transit amplifying cell, EE: enteroendocrine cell. Images are derived and adapted from Santos *et al.*[25]

1.4 Colorectal cancers develop via the adenoma-carcinoma sequence

In 1990, Fearon and Vogelstein suggested the adenoma-carcinoma sequence: CRCs develop from normal epithelium via pre-cancerous adenomas by the acquisition of sequential mutations in pathways that regulate DNA repair and cell proliferation[26]. Since then, this model has been confirmed and refined[27,28] (Figure 5). Normal intestinal cells move upwards along the vertical crypt axis towards the intestinal lumen, where they undergo apoptosis and are shed into the lumen of the intestine. If the terminal differentiation and apoptosis, which limit the life cycle of crypt cells to 3 – 5 days, are disrupted due to oncogenic mutations, an adenoma can form: The Wnt pathway is aberrantly activated in more than 90 % of CRCs, mostly by inactivation of both adenomatous polyposis coli (*APC*) alleles or activating

mutations in *CTNNB1*, the gene encoding β-catenin[29]. The resulting hyperactivation of the Wnt pathway is considered the initiating event in classic adenomas[30,31]. The gain of further mutations is necessary for the malignant transformation of an adenoma into a carcinoma *in situ* and at a later stage a carcinoma capable of local or distant metastasis formation. Typically, these driver mutations occur in *KRAS* (Kirsten rat sarcoma), *SMAD4*, and *TP53* (tumor protein p53)[26,32].

In the Wnt pathway's "off"-status, β-catenin is bound by a destruction complex composed of AXIN, APC, GSK3α/β (glycogen synthase kinase 3α/β), and CK1α/δ (casein kinase 1α/δ), leading to its proteasomal destruction[33,34]. The Wnt pathway in normal cells is activated when Wnt ligands bind to their heterodimeric receptor of FZD (Frizzled) and LRP5/6 (low density lipoprotein receptor related protein 5/6) on the cell surface which recruits AXIN to the receptor[35–39]. This inhibits the proper functionality of the destruction complex, which leads to the reduced degradation of β-catenin[37]. Instead, β-catenin accumulates and translocates into the nucleus where it activates transcription of Wnt target genes via DNA-bound TCF transcription factors[40,41]. In particular, β-catenin switches TCF from a transcriptional repressor into an activator by complex formation on the chromatin and by relieving TCF of its interaction with the repressing Groucho proteins[37]. Wnt target genes include *LGR5*, *AXIN2*, and *MYC* and enhance the proliferative and non-differentiated progenitor phenotype[42,43].

The Wnt target gene *MYC* is often aberrantly expressed in human cancers, including CRC[44]. It is also called cellular *MYC* (*c-MYC*) because it was first described as the cellular homolog of the retroviral v-myc, which was known to induce tumorigenesis in infected cells[45]. Later, the two other family members *MYCN* and *MYCL* were identified[46,47]. MYC is a central transcription factor that regulates a wide range of cellular processes, including proliferation, apoptosis, and DNA damage repair[44].

Another commonly mutated gene in CRC is *KRAS*, which in its oncogenic form leads to the aberrant activation of the mitogen-activated protein kinase (MAPK) pathway[29]. This clinically relevant pathway is described below in more detail.

Additionally, the loss of chromosome 18q is a frequent aberration in CRC and occurs in approximately 70 % of the cases[29,48,49]. This chromosomal arm contains the *SMAD4* gene, a component of the TGF-β and BMP signaling pathway. It regulates a plethora of cellular functions, including proliferation, differentiation, and apoptosis. In CRCs, the TGF-β pathway is frequently deregulated not only due to the absence of SMAD proteins but also

due to a mutation of the TGF-β receptor 2 (*TGFBR2*) gene[50,51]. *SMAD4* mutations have also been associated with metastasis formation and chemotherapy resistance in CRC[52,53].

The tumor suppressor p53 is called the "guardian of the genome", a term coined by David Lane in 1992[54]. As a transcription factor, it regulates the DNA damage checkpoint and can halt the cell cycle progression for DNA repair or induce senescence or apoptosis in case of irreparable DNA damage[55–57]. It is frequently lost in CRCs due to inactivating mutations or loss of its locus on chromosome 17p[29].

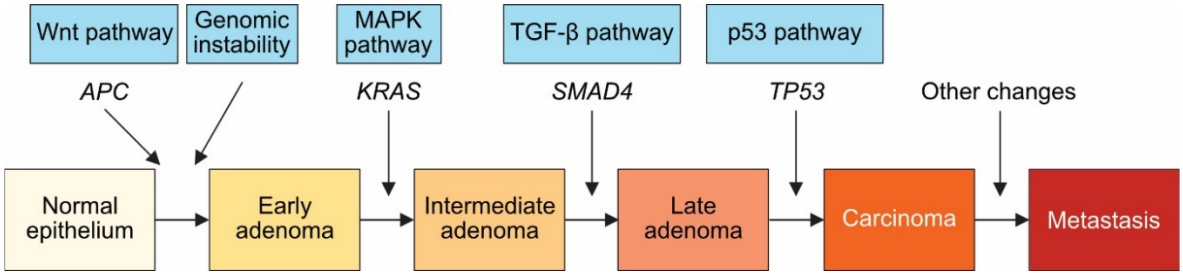

Figure 5: The adenoma-carcinoma sequence of colorectal cancer

Genetic model of colorectal cancer development. Frequently affected pathways are shown in blue with commonly mutated proteins of these pathways below. The figure was adapted from Fearon and Vogelstein[26] as well as Pinto and Clevers[27].

1.5 The EGFR-MAPK pathway

One of the therapeutically most relevant pathways, which are frequently activated in CRC, is the EGFR-MAPK pathway (Figure 6). This signaling cascade is activated upon binding of growth factors of the EGF family to their receptors on the cell surface, the ERBB family (erythroblastic oncogene B) of receptor tyrosine kinases. The ERBB family consists of four members, ERBB-1 to ERBB-4 (which are also called HER1 to HER4, short for human epidermal growth factor receptor). ERBB-1 is also known as EGFR (EGF receptor) and is activated by binding of EGF or TGF-α[58].

Binding of a ligand leads to EGFR dimerization and subsequent autophosphorylation of its cytoplasmic tail. Downstream signaling activates RAS proteins[58]. This family of small GTPases consists of KRAS, NRAS, and HRAS. Activation of RAS proteins can trigger a plethora of different pathways, regulating many different cellular processes[59,60]. Examples for downstream signaling of RAS include the MAPK pathway and the phosphatidyl-inositol 3 kinase (PI3K) pathway[60]. Due to considerable crosstalk, the PI3K pathway can also be directly activated by EGFR[58].

Very recently, computational models predicted that in the colonic epithelium, RAF proteins (rapidly accelerated fibrosarcoma) are the most common interaction partner of RAS for downstream signaling[61]. The RAF family of serine/threonine kinases comprises RAF1, BRAF, and ARAF proteins and is part of the MAPK pathway[59,60]: This three-tiered pathway is initiated when a RAS family member activates a RAF protein – classically KRAS and BRAF. In the next step, RAF phosphorylates the mitogen-activated protein kinase kinase (MAPKK, also known as MEK). Downstream of MEK, the extracellular-signal regulated kinase (ERK, also known as MAPK) activates several cytoplasmic and nuclear substrates by phosphorylation and thereby regulates proliferation, metabolism, and survival[59,60].

Several proteins of these pathways can be affected in cancer. Most importantly, *KRAS* is mutated in 40 % of CRCs, typically in codons 12 or 13. These mutations, the most prominent being $KRAS^{G12D}$, constitutively activate the KRAS protein by locking it in its activated GTP-bound state[59]. In addition, *EGFR*, *BRAF*, and *PIK3CA* (phosphatidyl-inositol 3 kinase catalytic subunit α) mutations can drive colorectal tumorigenesis[62]. While mutations in *RAS* and *PIK3CA* often occur in the same tumor cell, *BRAF* and *KRAS* mutations are mutually exclusive[29].

Targeted inhibitors against several pathway members were developed. For instance, EGFR can be inhibited with the clinically approved antibodies Cetuximab (Cmab) and Panitumumab or the small molecule inhibitor Afatinib, which is currently evaluated in clinical trials[63,64]. In addition, the MEK inhibitor Selumetinib has also entered clinical testing[64].

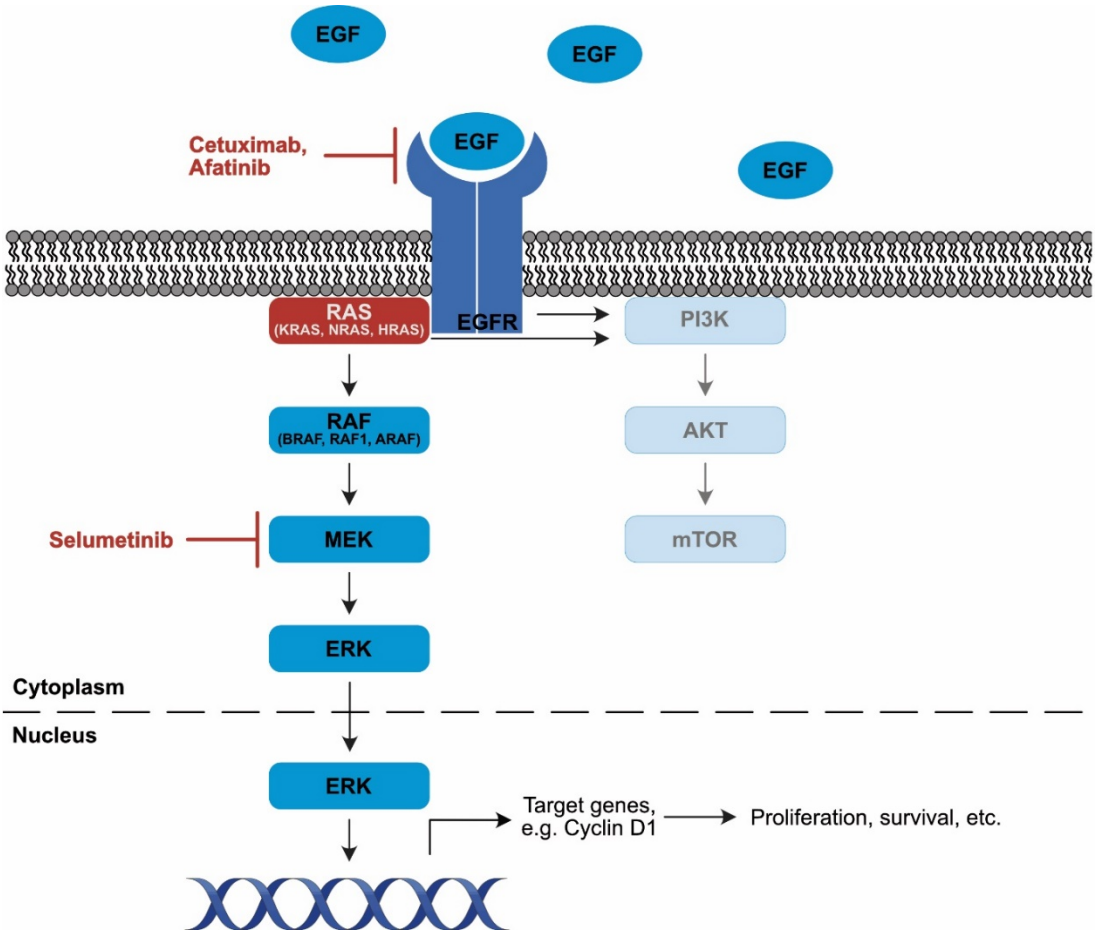

Figure 6: EGFR-MAPK signaling

Binding of epidermal growth factor (EGF) to its receptor (EGFR) can activate RAS proteins and the downstream mitogen-activated protein kinase (MAPK) pathway with its three-tiered kinase activation of RAF, MEK, and ERK proteins. Transcription of target genes leads to proliferation and survival. Alternatively, EGFR and RAS proteins can also activate the phosphatidyl-inositol 3 kinase (PI3K) pathway. Inhibitors of EGFR (Cetuximab and Afatinib) and MEK (Selumetinib) are indicated. RAS: rat sarcoma, RAF: rapidly accelerated fibrosarcoma, MEK: mitogen-activated protein kinase kinase, ERK: extracellular-signal regulated kinase, mTOR: mechanistic target of rapamycin.

1.6 Genomic instability in colorectal cancer

Hanahan and Weinberg described the acquisition of genome instability as an "enabling characteristic" that might be a prerequisite for the generation of the hallmarks of cancer[3]. Mutations in several pathways are necessary for the formation of a tumor but the probability of these specific mutations to occur sporadically is very low due to the efficient DNA damage repair machinery. Therefore, Hanahan and Weinberg suggested that tumor cells acquire random mutations at a higher rate than normal cells via deregulated damage repair or genomic instability[3].

In CRC, two major pathways lead to the acquisition of genome instability: Chromosomal instability (CIN) and microsatellite instability (MSI). While CIN CRCs show gross chromosomal changes and lower numbers of base pair mutations (non-hypermutated, fewer than 8.24 mutations per million bases), microsatellite instable CRCs are hypermutated (more than 12 mutations per million bases)[29]. In general, MSI tumors show approximately ten times more somatic mutations than microsatellite stable (MSS) tumors[29,65,66].

Approximately 65 – 84 % of sporadic CRCs are chromosomally instable, which is characterized by gross chromosomal changes such as aneuploidy and structural changes, including deletions, gains, and translocations. These changes lead to somatic copy number alterations rather than an increase in single base pair mutations[8,9,62]. The CIN tumors arise via the classical adenoma-carcinoma sequence with a hyperactivation of the Wnt signaling pathway in combination with *TP53*-inactivating mutations, activating mutations of the oncogenes *KRAS* and / or *PIK3CA,* and LOH at chromosome 18q, which contains the *SMAD4* gene[26,27].

Approximately 15 % of sporadic CRCs develop MSI as their mechanism of genomic instability[67]. These tumors are hypermutated due to faults in mismatch repair (MMR) genes: most cases have methylated and therefore inactivated *MLH1* (mutL homolog 1) promoters but other MMR genes such as mutS homolog (*MSH*) 2, *MSH6*, *PMS2*, or the MSH2-regulating *EPCAM* can also be affected[8,62,67,68]. Inactivation of these genes causes single base mismatches and a compromised replication at DNA microsatellites, which consist of one to four base pair tandem repeats. The malfunctioning MMR causes further mutations in oncogenes and tumor suppressor genes, giving the tumors an advantage. Promoters of *MLH1* and other genes can be methylated in the CpG island methylator phenotype (CIMP) which is associated with MSI tumors[8,62]. In contrast to CIN CRCs, sporadic MSI tumors are often wild type in *TP53*[29]. Furthermore, *APC* mutations are present in only 35 to 50 % of MSI tumors, but 80 to 90 % show an oncogenic activating $BRAF^{V600E}$ mutation, which is considered an alternative initiating event of MSI tumor formation[29,62,69]. Other common mutations include *TGFBR2*, which contains nucleotide repeat sequences, and other genes that regulate proliferation, cell cycle arrest, apoptosis, and DNA repair[29,62].

MSI tumors cannot only develop sporadically but also as a consequence of the Lynch syndrome which is caused by a germline mutation in one of the MMR genes, mostly *MSH2* or *MLH1*[70,71]. Loss of the second allele during the lifetime of the patient by mutation or promoter methylation leads to a corrupted MMR, causing MSI and CRCs[72]. In contrast to

sporadic MSI tumors, CRCs that are caused by the Lynch syndrome do not carry mutations in *BRAF*[9].

More recently, The Cancer Genome Atlas project analyzed CRCs and normal epithelium of 276 patients[29]. Whole exome sequencing, somatic copy number alteration, promoter methylation, mRNA, and miRNA analyses of these samples as well as whole genome sequencing of 97 samples were performed. This study confirmed the stratification of CRCs into hypermutated and non-hypermutated cases (Figure 7). Moreover, the consortium also detected a rather small fraction (3 % of CRC cases) with mutations in polymerase ε (POLE), which coincided with an even higher mutational load and hence has been designated ultramutated[29].

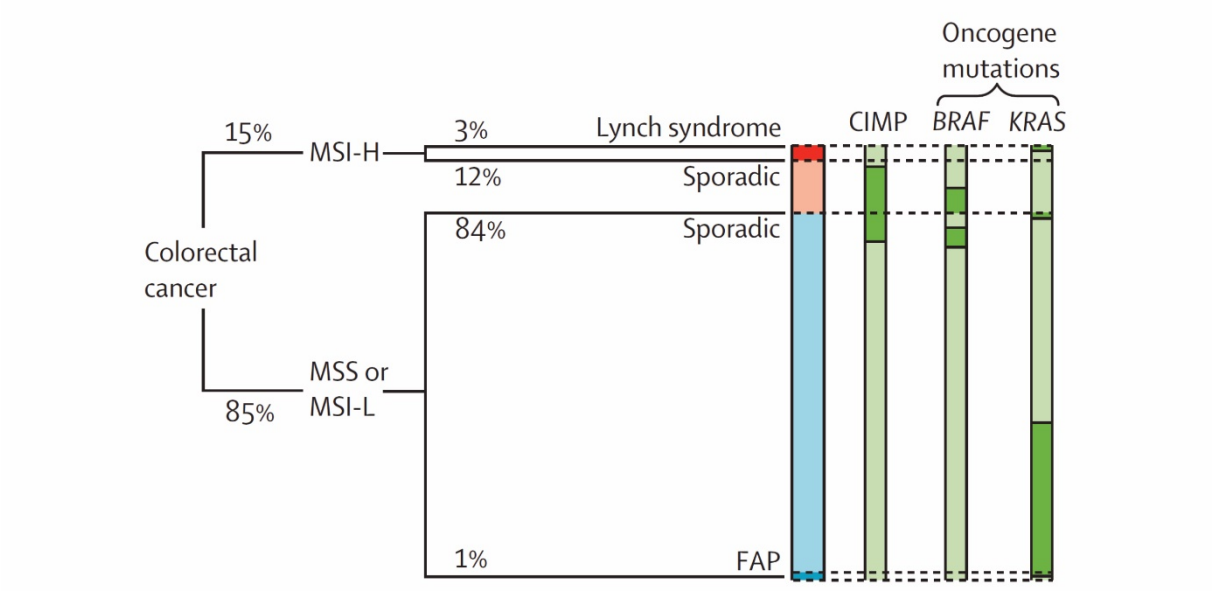

Figure 7: Frequency of mutated oncogenic drivers in dependence of the mechanism of genomic instability in colorectal cancer

Schematic showing the percentages of CRCs with the different types of genomic instability and the associating characteristics. MSI-H: high level microsatellite instability, MSS: microsatellite stability, MSI-L: low level microsatellite instability, FAP: familial adenomatous polyposis, CIMP: CpG-island methylator phenotype. Figure is taken from Brenner *et al.*[9]

1.7 Therapy of colorectal cancer

1.7.1 Therapeutic agents and their mechanisms of action

The first chemotherapeutic agent successfully used in the treatment of CRC was 5-fluorouracil (5-FU)[73]. Its metabolite fluorodeoxyuridine monophosphate (FdUMP) acts as an inhibitor of the thymidylate synthase[73–75]. This enzyme is necessary for the *de novo*

pyrimidine synthesis and its inhibition results in replication stress induced by an imbalance in deoxynucleotides[76]. The replication stress is exacerbated by the erroneous incorporation of another metabolite of 5-FU (fluorodeoxyuridine triphosphate) into the DNA[76]. In addition, RNA is destabilized by the incorporation of a third 5-FU derivative (fluorouridine triphosphate)[77] (Figure 8A, B). In the 1980s, studies showed that addition of Leucovorin (folinic acid) induces the cytotoxicity of 5-FU by enhancing its inhibitory effect on the thymidylate synthase[73,78–80].

Topoisomerase I is another cellular component that can be targeted by chemotherapeutic agents such as camptothecins, including Irinotecan (also known as CPT-11)[77,81]. The prodrug Irinotecan is metabolized into its active derivative SN-38 by esterases in liver cells and normal intestinal tissue[82]. During normal DNA replication, the enzyme topoisomerase I induces temporary single strand DNA breaks[77]. This DNA break releases the pressure of the DNA and allows unwinding of the DNA ahead of the replication fork. If topoisomerase I is inhibited by SN-38, the pressure of the coiled DNA cannot be relieved by single strand breaks. Instead, double strand DNA breaks occur when the replication fork and the topoisomerase I complex collide. The DNA double strand breaks lead to cell death, either by apoptosis or necrosis[77,83,84] (Figure 8C).

Subsequently, several studies examined the combination of different chemotherapeutic agents, especially folinic acid/5-FU plus either Irinotecan (FOLFIRI) or plus Oxaliplatin (FOLFOX), a platinum-containing cytotoxic agent[73,85,86]. FOLFIRI and FOLFOX achieved similar improved progression-free and overall survival[73,87].

In 2004, a phase III clinical trial showed that anti-angiogenic therapy can improve the outcome of CRC when combined with FOLFIRI: addition of the monoclonal antibody Bevacizumab, which targets the vascular endothelial growth factor (VEGF), led to a prolonged progression-free and overall survival[88]. Another protein that can be targeted for therapy of CRC is EGFR. Two different inhibitory monoclonal antibodies are approved: Cmab and Panitumumab[73,89,90] (Figure 8A).

The FIRE-3 study compared FOLFIRI plus Bevacizumab with FOLFIRI plus Cmab in *KRAS* wild type metastatic CRCs. It was shown that FOLFIRI plus Cmab was superior with regard to overall survival, the percentage of patients with an objective response, as well as the frequency of early tumor shrinkage[91]. However, later analyses of the data revealed that this benefit of Cmab compared to Bevacizumab was only seen in patients with a left-sided primary tumor[92].

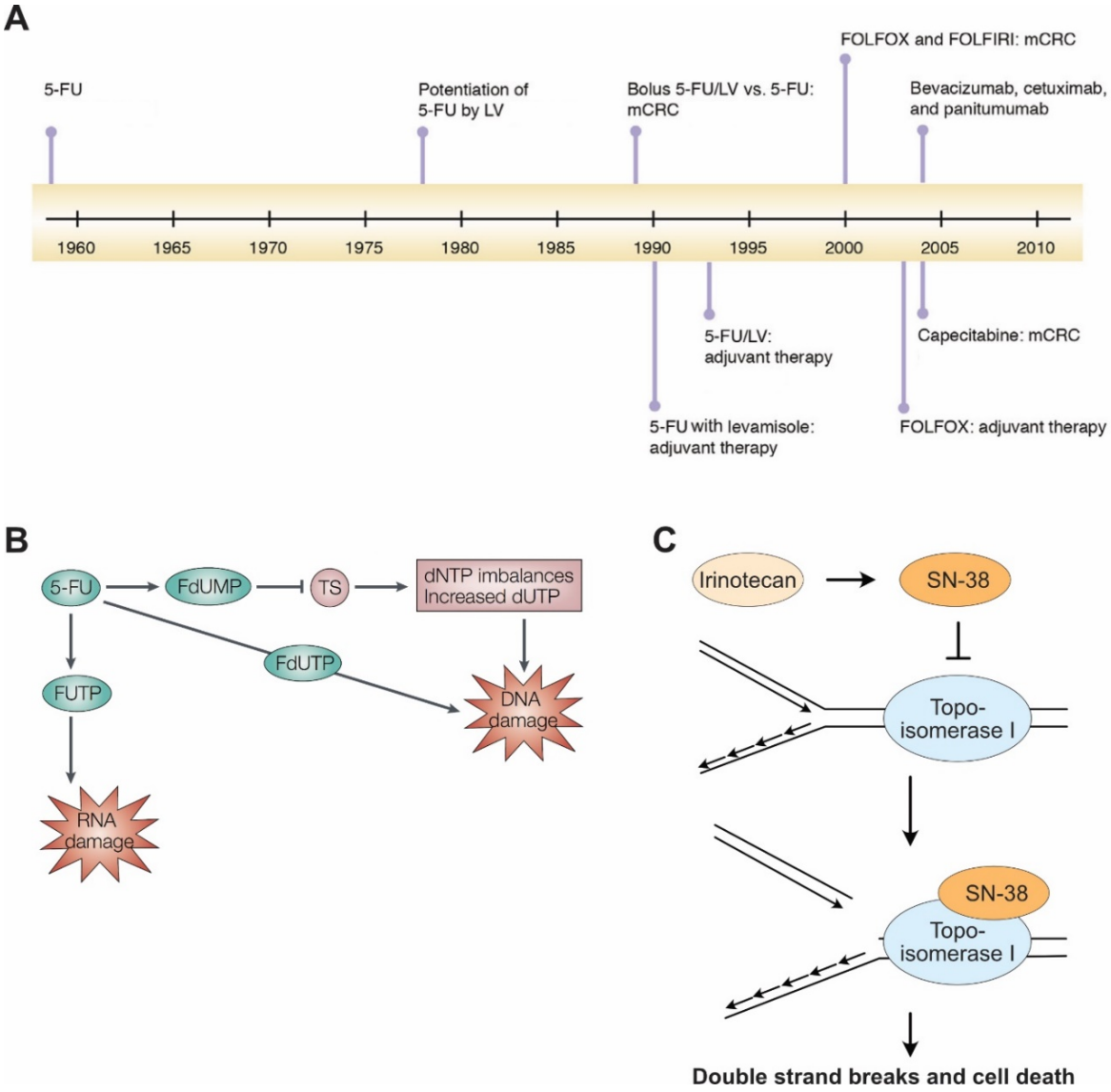

Figure 8: Advances in the treatment of colorectal cancer patients

A) Timeline of chemotherapeutic developments of colorectal cancer therapy. **B)** Mechanism of action of 5-FU. **C)** Mechanism of action of Irinotecan. A-C) 5-FU: 5-fluorouracil, LV: Leucovorin (folinic acid), FOLFIRI: 5-FU/LV with Irinotecan, FOLFOX: 5-FU/LV with Oxaliplatin, mCRC: metastatic colorectal cancer. FdUMP: fluorodeoxyuridine monophosphate, FdUTP: fluorodeoxyuridine triphosphate, FUTP: fluorouridine triphosphate, dNTPs: deoxynucleotidetriphophates, dUTP: deoxyuridine triphosphate. Figures were taken and adapted from A) Gustavsson *et al.*[73], B) Longley *et al.*[93], C) Hsiang *et al.*[84], and Warren and Eastman[94].

1.7.2 Current approaches in the therapy of colorectal cancer

In Germany, the German Cancer Society, the German Cancer Aid, and the Association of the Scientific Medical Societies in Germany specify the ideal treatment of CRCs in the "S3-Guideline for Colorectal Cancer" as follows[63]: Benign polyps, adenomas, and CRCs should be surgically removed, if possible. From stage II to stage IV, the resection of the affected

colonic segment (colectomy) is combined with other treatment options as soon as possible after surgery. These options include radiation (mostly stages II and III), chemotherapy (stages II to IV), and targeted agents in combination with chemotherapy (stage IV). Common chemotherapeutics include 5-FU (or its prodrug Capecitabine) plus its adjuvant Leucovorin, Irinotecan, Oxaliplatin, or combinations of these. Targeted agents include the anti-VEGF antibody Bevacizumab or the EGFR-targeted antibodies Cmab or Panitumumab[63] (Table 1).

Table 1: Approved and investigational therapeutics for the treatment of colorectal cancer

Chemical compound	Trade name	Mechanism of action	Approved for CRC
5-FU/Leucovorin	Several	Thymidylate synthase inhibitor	First-line
Irinotecan	Several	Topoisomerase I inhibitor	First-line
Oxaliplatin	Eloxatin®	DNA crosslinking	First-line
Cetuximab	Erbitux®	EGFR inhibiting antibody	First-line
Panitumumab	Vectibix®	EGFR inhibiting antibody	First-line
Bevacizumab	Avastin™	VEGF inhibiting antibody	First-line
Regorafenib	Several	Multikinase inhibitor	Later lines
Trifluridine/tipiracil (TAS-102)	Lonsurf®	Nucleoside analogue, thymidine phosphorylase inhibitor	Later lines
Afatinib	Giotrif®	EGFR/HER2 inhibitor	No
Selumetinib	Koselugo™	MEK inhibitor	No
Alisertib	None	AURKA inhibitor	No

In case of liver metastatic CRC, the resection of the primary CRC and the metastases in combination with an adjuvant therapy is aimed at if the physical condition of the patient allows it. This first-line therapy can consist of a chemotherapy plus anti-VEGF or plus anti-EGFR agents. The chemotherapy should be comprised of combinations including 5-FU such as FOLFIRI. The choice between anti-VEGF and anti-EGFR depends on factors such as the *RAS* and *BRAF* mutational status and the localization of the primary tumor in the colorectum[63]. Activating mutations in *KRAS*, *NRAS*, or *BRAF* confer resistance to EGFR-targeted therapeutics such as Cmab because they elicit signaling downstream of EGFR[95,96]. For this reason, *KRAS* mutant liver metastatic CRC is currently treated with chemotherapy plus Bevacizumab[63].

Second-line therapy can include first-line therapeutics that were not already used in the patient during initial treatment, such as Bevacizumab in patients previously treated with Cmab. Later lines of therapy include the chemotherapeutic TAS-102 (trifluridine/tipiracil)

and the multikinase inhibitor Regorafenib[63]. However, these therapeutic regimen lead to more adverse events than the first-line therapeutics and second- and later line therapies are usually less effective than first-line therapy[63,97]. Therefore, intensive research to find new treatment options is of the utmost importance.

1.7.3 Therapy resistance

Even though the treatment options of CRC have improved during the last decade, resistance towards chemotherapy and targeted drugs drives relapse and thereby still limits the success of therapy[5,6]. Several different mechanisms to acquire resistance are well described, especially those affecting the efficacy of targeted drugs such as EGFR/MAPK pathway targeting inhibitors.

For instance, alternative activation of the EGFR and MAPK pathways can drive the resistance via diverse mechanisms: First, the targeted protein itself can be amplified or mutated, rendering it irresponsive to the inhibiting agent. $EGFR^{T790M}$ mutations are commonly detected in tumors that relapsed from Erlotinib treatment in lung cancer[98,99]. Second, mutations in downstream signaling can confer resistance. For instance, activating mutations in *RAS* or *BRAF*, but also *PIK3CA* lead to a reduced sensitivity towards EGFR-inhibiting agents[95,96]. Third, feedback mechanisms can restore MAPK signaling, independent of known mutations[100,101].

Moreover, other compensatory signaling pathways can be activated and can render cells irresponsive to the treatment. MEK inhibition can lead to the activation of the related PI3K pathway in breast cancer cell lines or Yap/Tead2 (TEA domain transcription factor 2) signaling can compensate for the loss of Kras-mediated Mapk signaling in a murine pancreatic ductal adenocarcinoma model[101,102].

Treatment with targeted inhibitors can induce the emergence of a drug tolerant subpopulation, so-called drug persister cells. These are characterized by global epigenetic and transcriptional alterations rather than mutational changes[103–106]. Liau *et al.* showed that treatment with the multikinase inhibitor Dasatinib kills most glioblastoma stem cells *in vitro*, while a small subpopulation of cells remains viable[103]. These cells proliferate only slowly under drug treatment and adapt their gene expression profile in a way that leads to an increased drug tolerance[103]. Moreover, even single cell-derived clones showed the evolution of a drug tolerant persister subpopulation during targeted treatment in this study while the majority of the cells died[105]. This observation stands against a genetically predetermined, rigid division of cells into a majority of treatment sensitive and a minority of pre-existing

drug tolerant cells. Instead, these observations suggest a treatment-induced switch towards a drug persister phenotype in a small fraction of cancer cells[105].

Drug persister cells can eventually acquire mutations in clinically relevant genes during prolonged selection pressure by the treatment[104]. These mutations could then confer a complete resistance towards treatment followed by the selection and expansion of the mutated cells, ultimately resulting in the regrowth of a completely resistant tumor.

1.7.4 Drugging the undruggable: KRAS and MYC

Both *KRAS* and *MYC* are frequently mutated or upregulated in human cancers, respectively[29]. However, the development of direct inhibitors of these proteins has been challenging.

The structure of KRAS does not contain unique binding pockets that can be used for the development of small molecule inhibitors[44,107]. Nevertheless, recent studies have described inhibitors that specifically target $KRAS^{G12C}$ by forming a covalent disulfide bridge with the cysteine at position 12 of the mutated KRAS protein[108]. Some of these $KRAS^{G12C}$ inhibitors have already entered clinical trials[109,110].

Without the possibility of direct targeting, other mechanisms to inhibit these proteins indirectly need to be established. One possibility is to inhibit one or more proteins in the same pathway of the undruggable protein. While targeting of MEK alone in *KRAS* mutant tumors showed no effect, the combined treatment with MEK plus EGFR inhibitors seems to be more efficient in some models of *KRAS* mutant CRCs[111]. However, other studies reported that this treatment combination achieves efficient eradication only of tumor organoids of *KRAS* wild type but not mutated CRC cells[112].

Another possibility is to target compensatory pathways or proteins that are upregulated in response to the undruggable protein itself or to inhibitors of these pathways. For instance, MEK inhibitors cannot only be combined with EGFR inhibitors but also with inhibitors of the closely related PI3K pathway[101]. Moreover, *Kras* tumors have been shown to be dependent on Yap1/Tead2 signaling, especially when acquiring RAS-independence after targeted deletion of the oncogenically activated Kras variant in a murine pancreatic ductal adenocarcinoma model[102].

However, so far, these treatment combinations have suffered from great toxicity in clinical trials, which strongly limits their application in patients and underlines the need for further research[113,114].

Targeting MYC has also been problematic: Since it is localized in the nucleus it is less accessible compared to kinases or receptors in the cytoplasm or at the cell surface[115]. In addition, it plays a role in essential physiological processes[115]. Moreover, since MYC is not an enzyme, it does not have an active site that could be inhibited. Instead, targeting its functionality is limited to either downmodulating its expression levels (e.g. impairing MYC transcription or translation, or to augment its degradation) or to prevent its dimerization with MAX or the binding of this heterodimer to the target DNA. The latter approach recently entered clinical trials: A dominant negative MYC peptide, called Omomyc, can block the binding of MYC to its target DNA[115,116]. This Omomyc peptide has shown great anti-tumor effects in various cancer entities *in vivo*[117–119]. In 2021, the first phase I/II clinical trial with this peptide was initiated in different tumor entities, including *RAS* mutant CRC (NCT04808362, clinicaltrials.gov, accessed on May 26, 2021)[115].

1.8 Aurora kinase A

Errors in mitosis can lead to aneuploidy, which in turn can result in malignant transformation of the cell. Therefore, mitosis needs to be tightly controlled by mitotic kinases[120]. One of the major mitotic kinase families is the Aurora kinase family, consisting of Aurora kinase A (AURKA), Aurora kinase B (AURKB), and Aurora kinase C (AURKC) [121]. While AURKA plays an important role in the regulation of the G_2/M transition, AURKB is active in later phases of mitosis (metaphase to cytokinesis), and AURKC functions in meiosis[121].

Starting in the late S phase and peaking at the G_2/M transition, AURKA accumulates in the cell via transcriptional activation[122]. In the different stages during the G_2/M phases, AURKA activates different co-factors (including BORA[123], AJUBA[124], and TPX2[125]) which in turn mediate and maintain autophosphorylation at threonine 288 in the kinase domain of AURKA. This allows a conformational change of AURKA and triggers additional phosphorylations, leading to its full activation[126–128]. AURKA has many different tasks in the regulation of G_2/M phases of the cell cycle, such as the regulation of the mitotic entry, centrosome maturation, and the mitotic spindle formation[121]. At the end of mitosis and the beginning of the G1 phase, AURKA is ubiquitinated and subsequently degraded by the E3 ligase anaphase promoting complex/cyclosome (APC/C)[129,130].

The transcription of *Aurka* has been shown to be activated by MYC in the murine fibroblast line Balb/c-3T3[131]. This was also confirmed in the human hepatocellular carcinoma cell lines HepG2 and BEL-7402: MYC activates the transcription of *AURKA* by binding to the CpG-islands in the promoter region of the *AURKA* gene[132]. Interestingly, AURKA was also

described to activate *MYC* transcription as a transcriptional cofactor. Moreover, the overexpression of *AURKA* was partially able to rescue the detrimental effects of *MYC* knockdown on colony formation. Simultaneously, MYC overexpression rescued the reduced colony formation evoked by AURKA knockdown[132].

Intriguingly, Dauch *et al.* showed that Myc and Aurka form a complex that prevents proteasomal degradation of Myc in a murine hepatocellular carcinoma model[133]. Treatment with Alisertib, a conformation changing inhibitor of Aurka, prevented the *de novo* generation of this complex and led to the degradation of Myc. Subsequently, cell viability and tumor growth of subcutaneously injected hepatocellular carcinoma cells was reduced[133]. In thyroid cancer, this complex of MYC and AURKA could be confirmed[134]. Treatment with Alisertib also reduced MYC levels and subcutaneous tumor growth of highly MYC expressing cell lines[134].

Together, these data suggest a reciprocal transcriptional activation of *AURKA* and *MYC* and a direct interaction of the AURKA and MYC proteins, which is important for MYC functionality and stability in cancer cells.

1.8.1 Aurora kinase A in cancer

Overexpression of AURKA results in multipolar spindle formation, faulty chromosome segregation, and aneuploidy, which can favor tumor development. This is supported by the frequent amplification of chromosome 20q13.2, which contains the *AURKA* gene, or other mechanisms that culminate in the overexpression of *AURKA* in different tumor entities, including CRC[135–138]. Increased levels of AURKA are also associated with poor prognosis in cancers[139–142]. However, also the pharmacologic inhibition of AURKA can lead to aneuploidy because of defective spindle formation, which indicates that balanced levels of AURKA are necessary for successful G_2/M progression[143].

Interestingly, genomic instability does not seem to be the only phenotype AURKA overexpression confers to a tumor cell: AURKA also crosstalks with other signaling pathways and interacts with proteins that are frequently deregulated in various tumor entities such as p53[144,145], MYC[133], and Wnt[146,147] and MAPK[147] signaling.

For instance, AURKA disrupts the β-catenin destruction complex by direct phosphorylation of GSK3β in gastric cancer cells and by binding to AXIN in glioma cells. The resulting stabilization and hence accumulation of β-catenin activates the Wnt pathway[146,148].

Moreover, the genomic instability caused by AURKA would normally trigger a mitotic DNA damage checkpoint and eventually lead to apoptosis of the cell. In cancer cells with loss of

p53, this checkpoint is abolished, which results in the progression of the cell cycle instead of apoptosis, emphasizing the cooperation of p53 loss and AURKA[149,150]. Furthermore, AURKA phosphorylates p53 at Ser215 and Ser315, which leads to the inactivation of its transcriptional activity or its ubiquitination and subsequent degradation, respectively[144,145]. Conversely, p53 has also been reported to inhibit AURKA activity[151].

1.8.2 Targeting of Aurora kinase A

Since AURKA is amplified or overexpressed in different tumor entities and plays a role in regulating oncogenic pathways, it would be of great interest to pharmacologically inhibit the AURKA protein. Several AURKA isoform-specific and pan-Aurora kinase inhibitors are in development and certain candidate drugs have already entered clinical testing[152].

One of these AURKA-specific inhibitors is Alisertib (MLN-8237). It is an ATP-competitive small molecule inhibitor that binds AURKA, changes its conformation, and prevents its phosphorylation at Thr288[153–155]. It has a 150-fold stronger specificity for AURKA than AURKB[153].

It was and currently is evaluated in several clinical trials: ClinicalTrials.gov lists sixty-two studies for MLN-8237 (as of April 10, 2021). Forty-two of these have been completed, nine are still active or recruiting, and six have been terminated (plus one with the status “no longer available”, one suspended, and three withdrawn). Except for one clinical phase III study, all other studies are in phase I, II, or I/II.

In general, Alisertib is well tolerated. Most observed toxicities were hematologic or affected the gastrointestinal tract. Grade 3 (severe) and 4 (potentially life-threatening) adverse events included neutropenia, anaemia, and diarrhea[156–160]. Different phase II clinical trials have reported that Alisertib alone or in combination with chemotherapy is efficient at feasible drug doses in different tumor entities and the respective phase III clinical studies are planned or already initiated[156,158–161]. The only completed phase III trial showed similar progression-free survival of Alisertib- and comparator-treated patients, while Alisertib was better tolerated than the comparators[157]. These clinical trials support the feasibility of Alisertib treatment of patients and encourage further research with this inhibitor.

1.9 The patient-derived tumor organoid model in cancer research

To find new vulnerabilities of tumors, classical cancer cell lines and mouse models have been the gold standard for a long time. In recent years, the use of patient-derived tumor organoids (PDTOs) has been increasingly recognized as a valuable alternative because they

recapitulate the disease characteristics and heterogeneity of different cancer entities very well[162,163].

Moreover, e*x vivo* disease modeling using PDTOs recapitulates the spatial interactions between the tumor cells better than classical cell lines in two-dimensional culture. Especially oncogenic signaling pathways whose activation state strongly depends on the stiffness of the extracellular matrix and the diverse interactions of tumor cells with its components are represented better by PDTO cultures. For instance, Hippo pathway and Integrin-dependent signaling might exert their physiological effects on tumor growth only in this three-dimensional cancer model[164].

In contrast to mouse models, the PDTOs are less expensive, less time-consuming, and easier scalable. Another advantage is that normal tissue and tumors of the same patient can be used to derive organoids, which makes the development of personalized therapy more feasible. Furthermore, state-of-the art laboratory methods such as CRISPR/Cas9-mediated (clustered regularly interspaced short palindromic repeats/CRISPR-associated protein 9) genome editing have been successfully established in organoid cultures to analyze the impact of a specific set of cancer- or organ-specific mutations in isogeneic wild type-mutant pairs of cancer organoids or benign organoid lines, respectively[165–167]. For several different tumor types, PDTO models and biobanking libraries have been successfully established, including CRC[162,163], breast cancer[168,169], and pancreatic ductal adenocarcinoma[170].

However, one disadvantage of classical cancer stem cell- or adult stem cell-derived organoid models is the lack of interaction with other cell types like immune cells, stromal cells, and blood vessels. Therefore, a lot of work is being done to establish PDTO models that combine the cancer cells with these tumor-adjacent or -infiltrating cell types[171,172].

One important application of organoids is drug testing of new therapies for cancer treatment. A prerequisite for drug screens is that the response of the organoids correlates with that of the patient from whom the organoids were derived. For CRC, Ooft *et al*. demonstrated that PDTOs indeed can be used to predict the response of patients to Irinotecan-based chemotherapeutics[173], such as FOLFIRI. In contrast, there was no correlation between the response of the patient and the PDTOs to Oxaliplatin-based therapies, such as FOLFOX. This might be due to the lack of other cell types, especially immune and stromal cells, the *in vitro* culture conditions such as the specific composition of the cell culture medium or the extracellular matrix surrounding the PDTOs. Therefore, the ability to predict therapy sensitivity might be limited to specific treatment regimen, such as Irinotecan-based chemotherapy[173].

2 Aims

Metastatic spread and therapy resistance still diminish the treatment success in a large fraction of CRC patients. Therefore, our first aim was to model chemotherapy tolerance towards first-line combination therapy with FOLFIRI/Cmab in liver metastatic CRCs *ex vivo* by performing a long-term treatment of PDTOs. In a second step, we set out to characterize the parental and the chemotherapy tolerant PDTOs using next generation gene panel sequencing and RNA sequencing.

Subsequently, we used CRISPR/Cas9-mediated genome editing to introduce a $KRAS^{G12D}$ mutation into the tolerant PDTOs because this mutation can confer resistance to anti-EGFR targeting with Cmab. Based on the gene expression peculiarities of chemotherapy tolerant PDTOs, we aimed at establishing a second-line therapy able to overcome treatment tolerance. For FOLFIRI/Cmab tolerant PDTOs with a modelled $KRAS^{G12D}$ mutation, we applied combinations of clinically tested small molecule drugs, which act as targeted inhibitors against the signaling pathways of our interest. This approach consisted of a dual targeting of EGFR and MEK in combination with AURKA inhibition.

Since the PDTOs were derived directly from liver metastases of CRC or from a primary tumor with liver metastasis, we further assessed the AURKA protein levels in a cohort of matched non-metastatic, exclusive liver metastatic, and exclusive lung metastatic CRCs.

3 Materials

3.1 Chemicals and reagents

Application	Chemical compound	Supplier
Cell culture	Antibiotic-Antimycotic, 100×	Invitrogen, Karlsruhe, Germany
	Cell Recovery Solution	Corning, New York, NY, USA
	Collagenase IV	Biochrom AG, Berlin, Germany
	Dimethylsulfoxide (DMSO)	Sigma, Darmstadt, Germany
	Dispase	Stem Cell Technologies, Vancouver, BC, Canada
	Dithiothreitol (DTT)	Sigma
	Dulbecco's phosphate-buffered saline (PBS)	Invitrogen
	Ethylenediaminetetraacetic acid (EDTA) Disodium Salt Dihydrate	VWR International, Radnor, PA, USA
	Matrigel® Basement Membrane Matrix, phenol red-free	Corning
	Opti-MEM™ Reduced Serum Medium	Invitrogen
	TrypLE Select Enzyme	Invitrogen
	Trypsin-EDTA, 0.0 5%	Invitrogen
Western blotting	Ammonium persulfate	AppliChem, Darmstadt, Germany
	Bromophenol blue	Th. Geyer, Renningen, Germany
	DTT	Sigma
	Glycerol	Th. Geyer
	Glycine	Sigma
	Immobilon Western horseradish peroxidase (HRP) Substrate	Merck, Darmstadt, Germany

	Immobilon-P PVDF, 0.45µm Membrane	Merck
	Methanol	Carl Roth
	PageRuler ™ Prestained Protein Ladder	Invitrogen
	Phosphatase inhibitor cocktail 2	Sigma
	Phosphatase inhibitor cocktail 3	Sigma
	Polysorbate 20 (Tween20)	Th. Geyer
	RIPA buffer, including protease inhibitor cocktail, phenylmethylsulfonyl fluoride (PMSF), $NaVO_3$	Sigma
	SDS	Carl Roth
	Skim milk powder	Sigma
	Sodium chloride, NaCl	Sigma
	SuperSignal™ West Femto Maximum Sensitivity Substrate	Thermo Scientific, Waltham, MA, USA
	Tetramethylethylenediamine (TEMED)	Carl Roth
	Tris(hydroxymethyl)aminomethane (Tris)	Sigma
	Tris-Bis Acrylamide (30 %)	Carl Roth
Cloning	Ampicillin sodium salt	AppliChem
	LB agar (powder mix)	Carl Roth
	LB medium (powder mix)	Carl Roth
Hematoxylin-eosin stain	Eosin	Carl Roth
	Ethanol	Carl Roth
	Hematoxylin	Sigma
	Xylene	Carl Roth

3.2 Kits

Application	Kit	Supplier
DNA isolation	GenElute Mammalian Genomic DNA Miniprep Kit	Sigma
RNA isolation	High Pure RNA Isolation Kit	Roche, Penzberg, Germany
DNA concentration	Qubit ds DNA HS Assay	Invitrogen
RNA concentration	Qubit RNA HS Assay	Invitrogen
cDNA Transcription	High-Capacity cDNA Reverse Transcription Kit	Applied Biosystems, Foster City, CA, USA
qRT-PCR	primaQUANT 2× qPCR SYBR Green Master Mix	Steinbrenner, Wiesenbach, Germany
Genotyping	CloneJET PCR Cloning Kit	Thermo Scientific
	Phusion High Fidelity PCR Master Mix	Life Technologies, Carlsbad, CA, USA
Plasmid purification	NucleoSpin Plasmid EasyPure	Macherey Nagel GmbH, Düren, Germany
Mycoplasma detection	LookOut Mycoplasma PCR detection Kit	Sigma
Cell viability	CellTiter-Glo® 2.0	Promega, Madison, USA
	CellTiter-Glo® 3D	Promega
Cell cycle distribution	Click-iT™ EdU Alexa Fluor™ 488 Flow Cytometry Assay Kit	Invitrogen
	FxCycle™ Far Red Stain	Invitrogen
Protein concentration	Micro BCA™ Protein Assay Kit	Thermo Scientific
Immunohistochemistry	Ventana UltraView DAB IHC Detection Kit,	Roche
	Cell Conditioning Solution	Roche
Transfection of ribonucleoproteins (RNPs)	Alt-R CRISPR-Cas9 CRISPR RNA (crRNA)	IDT, Coralville, IA, USA

	Alt-R CRISPR-Cas9 trans-activating crRNA (tracrRNA)	IDT
Next generation gene panel sequencing	Oncomine Comprehensive Assay Plus	Thermo Scientific
	Ion AmpliSeq Library Kit	Thermo Scientific
	IonXpress Bacrode Adapter Kit	Thermo Scientific
	Ion Library Equalizer Kit	Thermo Scientific
	Ion 550 Chip	Thermo Scientific
Next generation whole exome sequencing	Experion™ RNA Std Sens Analysis Kit	Bio-Rad Laboratories
RNA sequencing	SureSelectXT Human All Exon V6	Agilent Technologies, Santa Clara, CA, USA
	Maxima RT polymerase	Thermo Scientific
	Nextera XT DNA Library Preparation Kit	Illumina, San Diego, CA, USA

3.3 Cytostatic compounds and small molecule inhibitors

Compound	**CAS number**	**Supplier**
5-FU	51-21-8	AppliChem
Afatinib (BIBW2992)	439081-18-2	TargetMol, Boston, MA, USA
Alisertib (MLN8237)	1028486-01-2	Selleckchem, Houston, TX, USA
Cetuximab (Erbitux®)	205923-56-4	Merck
Folinic acid	1492-18-8	Merck
Irinotecan	100286-90-6	Sigma
Selumetinib (AZD6244)	606143-52-6	TargetMol
SN-38	86639-52-3	TargetMol

3.4 Antibodies

3.4.1 Antibodies for immunoblot analysis

Target	Supplier	Order ID	Origin	Dilution
PARP	Cell Signaling Technology, Danvers, MA, USA	9542	Rabbit	1:1000
Cleaved caspase 3	Cell Signaling Technology	9661	Rabbit	1:1000
MYC	Proteintech, IL, USA	10828-1-AP	Rabbit	1:1000
Beta-actin	Sigma	A2066	Rabbit	1:2000
Alpha-tubulin	Sigma	T9026	Mouse	1:2000
Anti-mouse HRP	Dianova, Hamburg, Germany	715-035-150	donkey	1:10000
Anti-rabbit HRP	Dianova	711-035-152	donkey	1:10000

All antibodies were diluted in 5 % milk in TBS-T. HRP: horse radish peroxidase

3.4.2 Antibodies for immunohistochemical staining

Target	Supplier	Order ID	Origin	Dilution
AURKA	Cell Signaling Technology	91590	Rabbit	1:100

3.5 Oligonucleotides

3.5.1 CRISPR/Cas9 genetical engineering of *KRAS*

$KRAS^{G12D}$	5’- CATTATTTTATTATAAGGCCTGCTGAAAATGACTGAATATAAACTTGTCGTCGTTGGAGCTGATGGCGTAGGCAAGAGTGCCTTGACGATACAGCTAATTCAGAATCATTTTGT -3’
Electroporation enhancer	5’- TTAGCTCTGTTTACGTCCCAGCGGGCATGAGAGTAACAAGAGGGTGTGGTAATATTACGGTACCGAGCACTATCGATACAATATGTGTCATACGGACACG -3’

3.5.2 PCR amplification and sequencing of *KRAS*

KRAS fw	5’- ACGATACACGTCTGCAGTCAA -3’
KRAS rv	5’- TGTCACAATACCAAGAAACCCAT -3’
T7	5’- TAATACGACTCACTATAGGG -3’

3.5.3 qRT-PCR

AURKA fw	5’- GTCTACCTAATTCTGGAATATGC -3’
AURKA rv	5’- AGTTCTCTGGCTTAATGTCT -3’
B2M fw	5’- TCCATCCGACATTGAAGTTG -3’
B2M rv	5’- ACACGGCAGGCATACTCAT -3’
CDCA7 fw	5’- AGGCTCCGACTCACAATCAA -3’
CDCA7 rv	5’- CATGGGTAGAGCGTCAAGGG -3’
GAPDH fw	5’- GACAGTCAGCCGCATCTTCT -3’
GAPDH rv	5’- GCGCCCAATACGACCAAATC -3’
MT1G rv	5’- TCCTGCAAGAAGAGCTGCTG -3’
MT1G fw	5’- TTTGTACTTGGGAGCAGGGC -3’
NDRG1 fw	5’- CCCACCTTTTTGGGAAGGAAG -3’
NDRG1 rv	5’- GGTCGCTCAATCTCCAGGTC -3’
OLFM4 fw	5’- AGGTTCTGTGTCCCAGTTGT -3’
OLFM4 rv	5’- CAAGCGTTCCACTCTGTCCA -3’
PPIA fw	5’- AGCATGTGGTGTTTGGCAAA -3’
PPIA rv	5’- TCGAGTTGTCCACAGTCAGC -3’
SLC29A1 fw	5’- GCTGTATTCATGTGGCCTGG -3’
SLC29A1 rv	5’- ATCGTGCTCGAAGACCACAG -3’
SULT2A1 fw	5’- TCAGTTCCAAGGCCAAGGTGA -3’
SULT2A1 rv	5’- GGGCATCCAGCCATGAATGT -3’
TBX2 fw	5’- GCACGGCTTCACCATCCTAA -3’
TBX2 rv	5’- TTGGCAAACGGGTTGTTGTC -3’
TMEM171 fw	5’- GCCCTTGATTGTGCTTGTGG -3’
TMEM171 rv	5’- ATTATTACCGAGTCACCTACAGTG -3’

3.6 Solutions and buffers

3.6.1 Immunoblot analysis

Lower tris buffer

1.5 M Tris, pH 8.8
0.2 % SDS

Upper tris buffer

1.0 M Tris, pH 6.8
0.2 % SDS

Stacking gel, 10 mL

6.8 mL ddH_2O

1.7 mL 30 % acrylamide solution

1.25 mL upper tris buffer

0.1 mL 10 % SDS

0.1 mL 10 % ammonium persulfate

0.01 mL TEMED

Resolving gel, 12 %, 10 mL

3.3 mL ddH_2O

4 mL 30 % acrylamide solution

2.5 mL lower tris buffer

0.1 mL 10 % SDS

0.1 mL 10 % ammonium persulfate

0.004 mL TEMED

Laemmli buffer, 2×

125 mM tris/HCl, pH 6.8

4 % SDS

20 % glycerol

0.05 % bromophenol blue

2 % DTT

Tris-glycine gel running buffer for SDS-PAGE, 10×

30 g tris

140 g glycine

100 mL 10 % SDS

Ad 1 L ddH_2O

Transfer buffer, 10×

30 g tris

140 g glycine

Ad 1 L ddH_2O

Transfer buffer, 1×

100 mL 10x transfer buffer

200 mL methanol

700 mL ddH_2O

Tris-buffered saline (TBS) buffer, 10×

24.2 g tris base
80 g NaCl
Ad 1 L ddH_2O
pH: 7.6

TBS-T buffer, 1×

1x TBS

0.2 % Tween20

3.7 Cell culture media

3.7.1 SW620 cell culture medium

Component	Concentration	Supplier
Dulbecco's modified eagle medium (DMEM) High Glucose, GlutaMAX		Invitrogen
Fetal bovine serum (FBS)	10 %	Invitrogen
Penicillin-Streptomycin	100 U/mL	Invitrogen

3.7.2 PDTO cell culture medium

Component	Concentration	Supplier
Advanced DMEM/F12		Invitrogen
HEPES	10 mM	Invitrogen
GlutaMAX	10 mM	Invitrogen
Normocin	50 µg/mL	Invitrogen
B27 Retinoic acid free supplement	1x	Invitrogen
N-Acetylcysteine	1 mM	Sigma
Prostaglandin E_2	15 nM	Sigma
Noggin	25 ng/mL	Peprotech, Hamburg, Germany
LY2157299	500 nM	Selleckchem
EGF	50 ng/mL	Peprotech
SB202190	7.5 µM	Selleckchem
Y27632, for 48 hours after seeding	10 µM	Biozol Diagnostics, Eching, Germany

3.7.3 Patient-derived organoids (PDOs), WREN medium

Component	Concentration	Supplier
Advanced DMEM/F12	50 %	Invitrogen
Wnt3a, R-Spo3, and Noggin-conditioned Advanced DMEM/F12	50 %	
HEPES	10 mM	Invitrogen
GlutaMAX	10 mM	Invitrogen
Normocin	50 µg/mL	Invitrogen
N-2 Supplement	1x	Invitrogen
B27 Retinoic acid free supplement	1x	Invitrogen
N-Acetylcysteine	1 mM	Sigma
LY2157299	500 nM	Selleckchem
EGF	50 ng/mL	Peprotech
SB202190	7.5 µM	Selleckchem
Y27632, for 48 hours after seeding	10 µM	Biozol Diagnostics

3.7.4 Patient-derived organoids, EN medium

Component	Concentration	Supplier
Advanced DMEM/F12		Invitrogen
HEPES	10 mM	Invitrogen
GlutaMAX	10 mM	Invitrogen
Normocin	50 µg/mL	Invitrogen
N-2 Supplement	1x	Invitrogen
B27 Retinoic acid free supplement	1x	Invitrogen
Noggin	25 ng/mL	Peprotech
N-Acetylcysteine	1 mM	Sigma
LY2157299	500 nM	Selleckchem
EGF	50 ng/mL	Peprotech
SB202190	7.5 µM	Selleckchem
Y27632, for 48 hours after seeding	10 µM	Biozol Diagnostics

3.8 Laboratory equipment

Device	Supplier
BD LSRFortessa™	Becton Dickinson, Franklin Lakes, NJ, USA
Berthold Orion II Microplate Luminometer	Titertek-Berthold, Pfortzheim, Germany
Binder Incubator	Binder, Tuttlingen, Germany
Experion™ Automated Electrophoresis System	Bio-Rad Laboratories, Munich, Germany
Experion™ Vortex Station	Bio-Rad Laboratories
Experion™ Priming Station	Bio-Rad Laboratories
GeneAmp® PCR System 9700	Applied Biosystems, Foster City, CA, USA
Heraeus Megafuge 1.0R	ThermoFisher Scientific
HTU Soni130 Sonicator	G. Heinemann, Schwäbisch Gmünd, Germany
Ion Torrent GeneStudio S5 Prime	Thermo Scientific
Li-COR Odyssey Fc	Li-COR, Lincoln, NE, USA
LightCycler480	Roche
Mini Trans-Blot™ Cell	Bio-Rad Laboratories
Mini-PROTEAN Tetra Vertical Electrophoresis Cell	Bio-Rad Laboratories
AZ100 Multizoom Microscope	Nikon, Amsterdam, Netherlands
ND 1000 NanoDrop Spectrophotometer	NanoDrop Products, Wilmington, DE, USA
NEPA21 Electroporator	Nepagene, Chiba, Japan
Neubauer Counting Chamber	Carl Roth
NextSeq 500	Illumina
Qubit 3.0 Fluorometer	ThermoFisher Scientific
T100™ Thermal Cycler	Bio-Rad Laboratories, Munich, Germany
Varioskan™ Multimode Microplate Reader	Thermo Scientific
VectraPolaris™	Perkin Elmer, Waltham, MA, USA
Ventana Benchmark	Ventana Medical Systems, Oro Valley, AZ, USA

xCELLigence Real-Time Cell Analyzer (RTCA)	Agilent

3.9 Software

Software	Supplier
Affinity Designer 1.9.0.932	Serif (Europe) Ltd, Nottingham, UK
Affinity Publisher 1.9.0.932	Serif (Europe) Ltd
BD FACSDiva Software Version 6.2	BD Biosciences, San Diego, CA, USA
Experion™ Software version 3.20	Bio-Rad Laboratories
FlowJo v10.7.1	FlowJo LLC, Ashland, OR, USA
GraphPad Prism 7.01	GraphPad Software Inc., La Jolla, CA, USA
Image Studio Ver 5.2.5	Li-COR, Lincoln, NE, USA
Integrated Genomics Viewer	Broad Institute of MIT and Harvard, Cambridge, MA, USA
Ion Reporter System v5.16	Thermo Scientific
Microsoft Office 2016	Microsoft, Redmond, WA, USA
NIS Elements D Imaging Software, Version 5.00.00	Nikon Instruments Inc., Melville, NY, USA
Phenochart 1.0.8	Akoya Biosciences, Marlborough, MA, USA
RTCA Software Lite	Agilent
Simplicity 4.20	Titertek-Berthold
SkanIt Software 2.4.3 Research Edition Varioskan	Thermo Scientific

4 Methods

4.1 Patient-derived tissues for organoid culture and FFPE tissues

Fresh samples of normal colorectal epithelium and of tumor tissues were taken from patients in the context of curative colectomy or partial hepatectomy at the University Hospital Großhadern at the Ludwig-Maximilians-University (LMU) Munich, Germany in collaboration with Prof. Dr. Neumann and Prof. Dr. Kirchner. Samples were collected from remaining resected tissue by a pathologist and were not needed for diagnosis. The samples were irreversibly anonymized. The ethical committee of the LMU Munich classified this procedure as uncritical and specifically approved our projects (project numbers 591-16-UE and 17-771-UE).

Anonymized colorectal cancer specimens (formalin-fixed and paraffin embedded (FFPE) tissues of the M0/M1 cohort used for immunohistochemical staining of AURKA) from patients that underwent surgical resection at the LMU Munich between 1994 and 2017 were obtained from the archives of the Institute of Pathology. Follow-up data were recorded prospectively by the Munich Cancer Registry (data provided by J. Neumann, LMU Munich, Germany). Specimens were anonymized, and the study was approved by the institutional ethics committee of the Medical Faculty of the LMU (approval number 18-105-UE).

4.2 Stainings

4.2.1 Hematoxylin-eosin stain

For hematoxylin-eosin (HE) stain, 2 µm whole tissue sections of FFPE tumor samples were stained. The slides were incubated twice in xylene for 5 minutes each, followed by descending ethanol concentrations for 2 minutes each (2× 100 %, 1× 95 %). After a wash in water for 2 minutes, the slides were transferred to hematoxylin for 3 minutes and washed again in water, 3 times for 1 minute each. After an incubation in 95 % ethanol for 1 minute, the slides were stained in eosin solution for 45 seconds and again transferred to 95 % ethanol for 1 minute. Two incubation steps in 100 % ethanol for 1 minute each were followed by two steps in xylene for 2 minutes each.

4.2.2 IHC staining of AURKA

For immunohistochemistry (IHC), 2 µm whole tissue sections of FFPE tumor samples were stained using a Ventana Benchmark according to the manufacturer's instructions. Cell Conditioning Solution was used as a pretreatment and antibody binding was visualized using

the Ventana UltraView DAB IHC Detection Kit. The antibody directed against AURKA was used at a dilution of 1:100. For quantification of AURKA expression, the previously published H-score was used[174]. In short, each area of the section showing epithelial CRC tissue was assigned an intensity score from 0 to 3 (0 indicates no staining, 1 a weak staining intensity, 2 a moderate staining intensity, and 3 a strong staining intensity), and the proportion of tumor cells staining for that intensity was evaluated in 5 % increments (range from 0 to 100). The final H-score, ranging from 0 to 300, was then retrieved by adding the sum of scores obtained for each intensity and proportion of tumor areas stained.

4.3 Bacterial cell culture

For transformation of bacteria, the *Escherichia coli* strain Stbl3 was incubated with the plasmid vector on ice for 30 minutes before a heat shock for 45 seconds at 42 °C. The competent cells were then placed on ice for 2 minutes and subsequently 500 µL of LB medium without any antibiotics was added. The cell suspension was incubated for 60 minutes at 37 °C while shaking. The competent cells were grown overnight on LB plates with the appropriate antibiotic. Single colonies were cultured overnight in 5 mL LB medium supplemented with the appropriate antibiotic. The plasmid DNA was isolated and purified using the NucleoSpin Plasmid EasyPure Kit.

4.4 Mammalian cell culture

The SW620 cell line, PDTOs, and patient-derived organoids of human colonic mucosa (PDOs) were grown under standard cell culture conditions in a humidified incubator at 37 °C and 5 % CO_2.

4.4.1 Cell line culture

The SW620 cell line was purchased from ATCC (Wesel, Germany). The cells were cultured in DMEM, supplemented with 10 % FBS and 100 U/mL penicillin and 100 µg/mL streptomycin, which was exchanged every two to three days. For serial passaging when the cells reached a confluence of 70 – 80 %, the cells were incubated in 0.05 % trypsin for 5 minutes at 37 °C, then washed in culture medium and transferred to a new flask at a ratio of 1:3 to 1:10.

For cryo-preservation, the cells were incubated in trypsin and washed as for serial passaging (see above), resuspended in 50 % DMEM, 40 % FBS, and 10 % DMSO, slowly cooled to -80 °C, and then transferred to liquid nitrogen for long-term storage.

Cells were regularly tested negative for mycoplasma contamination using the LookOut Mycoplasma PCR Detection Kit.

4.4.2 Culture of patient-derived tumor organoids

PDTOs were isolated and propagated as described previously[162,175].

In short, the fresh tissue piece of primary CRC or liver metastasis was cut into pieces and incubated with Normocin and Antibiotic-Antimycotics for 15 minutes at room temperature. Afterwards, the tumor pieces were washed with PBS, minced with a scalpel, and incubated for 30 minutes at 37 °C in disaggregation solution, which consisted of Advanced DMEM/F12, supplemented with 5 U/mL dispase II, 75 U/mL collagenase IV, and 10 µM Y-27632. The cell suspension was then passed through a 1.2 mm needle with a syringe, washed in PBS, and passed through a 70 µm cell strainer. The cell suspension was subsequently incubated in ammonium chloride buffer for 5 minutes at room temperature, washed once in PBS and then in Advanced DMEM/F12 medium. The cells were embedded in Matrigel® and left to solidify for 15 minutes before the addition of PDTO medium (section 3.7.2). The PDTO medium was replaced every two to three days.

For serial passaging, PDTOs and the surrounding Matrigel® were incubated in 0.025 % Trypsin in PBS at 37 °C for 7 minutes, passed through a 0.8 mm needle with a syringe to dissociate the organoids, and washed twice in Advanced DMEM/F12. 5000 to 15000 cells were embedded in 50 µL Matrigel® drops and left to solidify for 15 minutes before the addition of PDTO medium.

Cryo-preservation was performed 4 – 6 days after seeding to ensure a small size of organoids. The Matrigel® was dismantled using Cell Recovery Solution for 30 minutes on ice, the organoids were then washed twice, resuspended in 50 % Advanced DMEM/F12, 40 % FBS, and 10 % DMSO, slowly cooled to -80 °C, and then transferred to liquid nitrogen for long-term storage.

Cells were regularly tested negative for mycoplasma contamination using the LookOut Mycoplasma PCR Detection Kit.

4.4.3 Generation of patient-derived organoids of human colonic mucosa

PDOs of human colonic mucosa were isolated and propagated by Dr. Cira García de Durango as described previously[176].

In short, the fresh tissue sample was cut into pieces and incubated in Antibiotics-Antimycotics for 15 minutes at room temperature. The tissue was then washed with PBS and

subsequently incubated in 10 mM DTT in PBS for 10 minutes at room temperature. The samples were transferred to 8 mM EDTA in PBS and incubated on ice for 1 hour. Afterwards, the supernatant was replaced with fresh, cold PBS and the tube was shaken vigorously to yield a supernatant enriched in colonic crypts. FBS was added to the sample to a final concentration of 5 % before centrifugation at 40 ×g for 5 minutes at 4 °C. The supernatant was replaced with Advanced DMEM/F12 supplemented with 2 mM GlutaMAX, 10 mM HEPES, and 5 % FBS. This washing step was repeated three times. Approximately 300 isolated crypts were seeded per 50 µL Matrigel® drop and left to solidify for 15 minutes before the addition of PDO medium (section 3.7.3). The PDO medium was replaced every two days.

For serial passaging, Matrigel® drops were washed with PBS, and incubated in TrypLE Select Enzyme for 10 – 15 minutes at 37 °C. The samples were then washed with Advanced DMEM/F12 medium, passed through a 0.8 mm needle with a syringe to dissociate the organoids, and washed again in Advanced DMEM/F12. 5000 to 10000 cells were embedded in 50 µL Matrigel drops and left to solidify for 15 minutes before the addition of PDO medium.

For *ex vivo* multi-lineage differentiation of human colonic organoids, the Wnt, R-spondin, EGF, and noggin-containing medium (WREN medium, section 3.7.3) was replaced with EGF and noggin-containing medium (EN medium, section 3.7.4), which lacks Wnt3a and RSPO-1, for at least 72 hours.

For cryo-preservation, the Matrigel® was dismantled using Cell Recovery Solution for 30 minutes on ice, the organoids were then washed twice, resuspended in 50 % Advanced DMEM/F12, 40 % FBS, and 10 % DMSO, slowly cooled to -80 °C, and then transferred to liquid nitrogen for long-term storage.

The cells were regularly tested negative for mycoplasma contamination using the LookOut Mycoplasma PCR Detection Kit.

4.4.4 Generation of chemotherapy tolerant PDTOs and cytostatic chemicals

Two days after seeding, the parental PDTO1, 2, and 5 were treated with 156 nM folinic acid, 625 nM 5-FU, 0.5 nM SN-38, and 10 µg/mL Cmab. To increase the effects of Cmab, the EGF concentration was reduced to 12.5 ng/mL. The treatment-containing PDTO medium was exchanged every two to three days. Serial passaging was performed as described above. For cell viability assays and immunoblot detections, the same FOLFIRI concentrations as for the generation of long-term chemotherapy tolerant PDTOs were used (see above), with

the following exceptions: For initial testing of the short-term response to FOLFIRI (Figure 10), the concentrations were 625 nM folinic acid, 2.5 µM 5'-FU, and 2 nM SN-38. To show that the chemotherapy tolerant PDTOs (CT-PDTOs) are more tolerant towards FOLFIRI/Cmab compared to parental PDTOs under short-term exposure via cell viability (Figure 12), the FOLFIRI concentration was increased to 312.5 nM folinic acid, 1.25 µM 5'-FU, and 1 nM SN-38. For cell cycle analysis and immunoblots showing comparisons between parental PDTOs and CT-PDTOs not involving AfaSel/Alisertib (Figure 13, Figure 14, Figure 21), the concentration was increased to 1250 nM folinic acid, 5 µM 5'-FU, 4 nM SN-38. The Cmab concentration was 10 µg/mL for all experiments.

4.4.5 Electroporation of PDTOs and genetic engineering of KRAS^{G12D}

Single cells were obtained from CT-PDTOs as described above for serial passaging (section 4.4.2). Subsequently, the cells were electroporated with DNA-free ribonucleoproteins (RNPs), consisting of the single guide RNA and the Cas9 enzyme, plus an oligonucleotide containing the *KRAS* locus of interest with the KRAS^{G12D}-encoding mutation for homology directed repair. The RNPs were assembled according to IDT's guide "Homology-directed repair using Alt-R CRISPR-Cas9 System and Ultramer Oligo". CT-PDTOs were transfected using NEPA21-electroporation as described by the manufacturer. In brief, the 10^5 single CT-PDTO cells were resuspended in 100 µL suspension of the RNP complexes in OptiMEM, supplemented with 10 µM of the Rho kinase inhibitor Y-27632. Final concentrations of the RNP complex components were: 738 nM crRNA, 738 nM tracrRNA, 369 nM Alt-R Cas9 Nuclease V3, 2.66 µM electroporation enhancer, and 2.66 µM KRASG12D HDR oligonucleotide. The cell suspension with the RNPs was transferred to a NEPA electroporation cuvette and electroporated with the following settings: two 5 ms poring pulses at 150 V with a pulse interval of 50 ms followed by five 50 ms transfer pulses at 20 V with an interval of 50 ms. After electroporation, 300 µL OptiMEM plus 10 µM Rho kinase inhibitor Y-27632 was added to the cell suspension and incubated for 30 minutes at room temperature. Subsequently, the cells were embedded in Matrigel® and left to solidify for 15 minutes before the addition of PDTO medium. Selection of successfully transfected cells was initiated three days after electroporation by reducing the EGF concentration in the PDTO medium to 12.5 ng/mL and adding 10 µg/mL Cmab.

4.5 Cell viability assay

4.5.1 SW620 cell line

For the assessment of the cell viability, SW620 cells were seeded in 80 µL cell culture medium at a density of 3000 cells/well of a flat-bottom 96-well plate. The next day, the cells were treated with 20 µL of DMSO- or drug-containing cell culture medium. Three days after treatment start, the cell viability was measured using CellTiter-Glo® according to the manufacturer's instructions. In short, the plate with the cells was incubated at room temperature for 30 minutes before 100 µL of CellTiter-Glo® was added. The plate was then incubated for at room temperature 2 minutes on a shaker, followed by 10 minutes without the use of a shaker. Luminescence was measured on a Berthold Orio II Microplate Luminometer. The cell viability was calculated as the percentage of each sample, normalized to the DMSO-treated control. Replicate numbers (n) are indicated in the respective figure legends.

4.5.2 PDTOs

2500 – 4000 single cells were seeded in 20 µL Matrigel® droplets in a flat-bottom 48-well plate and overlaid with 500 µL PDTO medium. Two or three days after seeding, treatment was started by exchanging the PDTO medium with DMSO- or drug-containing PDTO medium. The treatment duration is indicated in the respective figure legends and lasted from 4 to 18 days. On the day of the viability measurements, the PDTO medium was removed and replaced with 35 µL Advanced DMEM/F12. The Matrigel® droplets were disaggregated with a pipette and 85 µL of CellTiter-Glo® 3D was added. After 5 minutes on a shaker, the suspension was disaggregated further by pipetting up and down and then shaken for another 20 minutes. 100 µL of the suspension was transferred into a white 96-well plate. The luminescence was measured on a Berthold Orio II Microplate Luminometer. The cell viability was calculated as the percentage of each sample, normalized to the DMSO-treated control. Replicate numbers (n) are indicated in the respective figure legends.

4.6 Protein analysis

4.6.1 Protein lysate preparation and protein concentration determination

For SW620 cell, the sub-confluent cells were washed with PBS and lysed in RIPA (radioimmunoprecipitation assay) buffer (supplemented with proteinase inhibitor, PMSF, $NaVO_3$, phosphatase inhibitor cocktails 2 and 3) for 30 minutes on ice.

For PDTOs, the Matrigel® was dismantled using Cell Recovery Solution for 30 minutes on ice and subsequently washed twice in PBS. The cell pellet was resuspended in RIPA buffer (supplemented with proteinase inhibitor, PMSF, $NaVO_3$, phosphatase inhibitor cocktails 2 and 3) for 30 minutes on ice.

After incubation on ice, the SW620 or PDTO lysates were sonicated 3 times for 5 seconds each at 75 % amplitude using the HTU Soni130 Sonicator and centrifuged at 12,000 g for 20 minutes at 4 °C. The protein concentration of the supernatant was measured on a Varioskan™ multimode microplate reader using the Micro BCA™ Protein Assay Kit as described by the manufacturer.

4.6.2 Immunoblot analysis

For immunoblot analysis, 30 µg of each whole cell lysate was boiled in Laemmli buffer for 5 minutes at 95 °C, quick spun, and analyzed on a 12 % SDS-acrylamide gel via SDS-PAGE (sodium dodecyl sulfate polyacrylamide gel electrophoresis) in 1× tris-glycine gel running buffer. A wet transfer in 1× transfer buffer for 90 minutes at 100 V, with a maximum current of 350 mA transferred the proteins onto a PVDF membrane. Unspecific binding of the antibodies was prevented by blocking the membranes in 5 % milk in TBS before adding the specific primary antibody (section 3.4.1), which was diluted in 5 % milk in TBS-T. The membrane was incubated in the diluted antibody overnight at 4 °C while shaking. The membrane was then washed in TBS-T four times, 10 minutes each, on a vertical shaker. Subsequent incubation in HRP-coupled secondary antibody occurred at room temperature for 60 minutes. The membrane was then washed again as before, but with TBS without Tween20 detergent for the last washing step because Tween20 has been reported to react with enhanced chemiluminescence reagent, which can lead to higher background staining[177]. Imaging was performed on a Li-COR Odyssey Fc using Immobilon Western HRP Substrate (for actin, tubulin, and PARP (poly-(ADP-ribose)-polymerase)) or SuperSignal™ West Femto Maximum Sensitivity Substrate (for cleaved caspase 3 and MYC) for detection.

4.7 Cell cycle analysis

Cell cycle analysis was performed using the Click-iT™ EdU Alexa Fluor™ 488 Flow Cytometry Assay Kit in combination with the FxCycle™ Far Red Stain for fluorescence-activated cell sorting analysis (FACS). Established PDTOs were treated for 48 h with FOLFIRI/Cmab. Then, 5-ethynyl-2′-deoxyuridine (EdU) was added to the drug-containing PDTO medium to a final concentration of 10 µM for 2 h at 37 °C. The Matrigel® was

dismantled and the organoids were dissociated using 0.025 % trypsin in PBS for 7 minutes at 37 °C and subsequent passage through a 0.8 mm needle with a syringe. After washing the cell suspension in Advanced DMEM/F12, the samples were handled according to the manufacturer's instruction. For DNA content staining, the cells were resuspended in 400 µL of 200 nM FxCycle stain, diluted in 1 × Click-iT™ saponin-based permeabilization and wash reagent and supplemented with 100 µg/mL RNase A. The samples were measured on a BD LRS Fortessa™.

4.8 PCR amplification and sequencing of *KRAS* locus

To confirm the $KRAS^{G12D}$ mutation via PCR amplification and sequencing of the *KRAS* locus, genomic DNA of CT-PDTO eKRAS organoids was extracted using the GenElute Mammalian Genomic DNA Miniprep Kit. 50 ng genomic DNA was used as a template to amplify the region of interest with *KRAS* primers (section 3.5.2) using Phusion High Fidelity PCR Master Mix, according to manufacturer's instructions (PCR cycler program: 98 °C, 30 seconds; [35 cycles: 98 °C, 30 seconds; 63.5 °C, 10 seconds; 72 °C, 35 seconds]; 72°C, 1 minute; 16°C, hold). The PCR product was ligated into CloneJET PCR Cloning Kit vector according to manufacturer's instructions and transformed into the *Escherichia coli* Stbl3 strain as described above (section 4.3). Plasmid DNA was extracted and purified using the NucleoSpin Miniprep Kit. Sanger sequencing was performed using the T7 primer at Eurofins Genomics, Ebersberg, Germany.

4.9 Panel-guided next generation sequencing

Genomic DNA was extracted from PDTOs using the GenElute Mammalian Genomic DNA Miniprep Kit. Targeted next generation sequencing was performed by the Diagnostics Department of the Institute of Pathology, LMU Munich, with the Oncomine Comprehensive Assay Plus screening for genetic alterations in 500+ cancer-asssociated genes at the levels of DNA (SNV, MNV, indels, TMB status, MSI status). Briefly, libraries were generated using the Oncomine Comprehensive Assay Plus and Ion AmpliSeq Library-, IonXpress Barcode Adapter-, Ion Library Equalizer-kits together with Ion 550 Chip kits according to the manufacturer's instructions. The libraries were sequenced on an Ion Torrent GeneStudio S5 Prime next generation sequencing machine. Analysis of the results was performed with the Ion Reporter System (v5.16) followed by further variant and quality interpretation using a home-made excel tool and python-script filtering for clinically relevant mutations. Alterations were confirmed with the Integrated Genomics Viewer (Broad Institute).

Mutations were judged as relevant on the basis of the interpretation criteria utilized in ClinVar[178]. Only likely pathogenic and pathogenic mutations as well as VUS (variant of unknown significance or not evaluated in ClinVar with a prediction trend of being likely pathogenic – majorly frameshift or truncating variants) with allele frequencies ≥3% were reported.

4.10 Next generation whole exome sequencing (WES)

Genomic DNA from PDTOs was prepared using the GenElute Mammalian Genomic DNA Miniprep Kit. Subsequent steps were performed by the Genomics and Proteomics Core Facility of the German Cancer Research Center (DKFZ Heidelberg, Germany). WES libraries were prepared using Agilent SureSelectXT Human All Exon V6 (Agilent technologies) and 200 ng of input DNA according to the manufacturer's protocol. The final libraries were quality controlled by Agilent 4200 TapeStation System (Agilent technologies) and Qubit ds DNA HS Assay kit (Life Technologies-Invitrogen). Based on Qubit quantification and sizing analysis, sequencing libraries were normalized, pooled and clustered on the cBot (Illumina) with a final concentration of 250 pM (spiked with 1% PhiX control v3). 100 bp paired-read sequencing was performed on the Illumina HiSeq 4000 instrument using standard Illumina protocols at the Genomics and Proteomics Core Facility of the DKFZ Heidelberg.

Raw sequence data was trimmed based on base calling quality (min 13) at both ends while reads with length <50 nt after trimming were discarded, as well as reads containing "N" bases. Reads were mapped to the hg19 Human reference genome using BWA-aln 0.7.10 with default parameters. Mapped reads were filtered based on mapping quality (min 13) and reads not mapping to annotated protein coding regions were discarded. PCR duplicates were removed using samtools rmdup. Sequencing reads were realigned around insertions and deletions using GATK IndelRealigner. Sequence variants were detected using samtools mpileup and VarScan 2.3.7. Copy number alterations were detected as described before[179] based on the optimalCaptureSegmentation R package[180]. The minimum size of copy number alterations (CNAs) was set to 5 Mb, with 2 exons minimum per segment, allowing up to 10 segments per chromosome.

4.11 RNA isolation, cDNA transcription, and qRT-PCR

Total RNA was isolated using High Pure RNA Isolation Kit according to the manufacturer's instructions. Subsequently, complementary DNA (cDNA) was prepared from the RNA using

the High-Capacity cDNA Reverse Transcription Kit according to the manufacturer's protocols. Quantitative real-time PCR (qRT-PCR) was performed using the Fast SYBR Green Master Mix on a LightCycler480 as described by the manufacturer. Relative expression values were normalized to *PPIA* and *B2M* or *PPIA* and *GAPDH* expression as indicated in the figure legends and calculated using the ΔΔCt method. Melting curves were assessed for each experiment to confirm the generation of specific PCR products. For primer sequences, see section 3.5.3.

4.12 cDNA library preparation, RNA sequencing analysis, and gene set enrichment analysis

For next generation RNA sequencing, the parental and chemotherapy tolerant PDTO lines were seeded in control or FOLFIRI/Cmab-containing cell culture medium, respectively, in three independent replicates for each parental / chemotherapy tolerant PDTO pair. In addition, the RNA sequencing run was performed in technical duplicates. Quality of the isolated RNA was confirmed using the Experion™ RNA Std Sens Analysis Kit on a BioRad Experion™ Automated Electrophoresis System, according to the manufacturer's protocols. The following steps of the RNA sequencing were performed by Dr. Rupert Öllinger, Thomas Engleitner, and Prof. Dr. Roland Rad (Technical University Munich). Library preparation for bulk 3'-sequencing of poly(A)-RNA was done as described previously[181]. Briefly, barcoded cDNA of each sample was generated with a Maxima RT polymerase (Thermo Fisher) using oligo-dT primer containing barcodes, unique molecular identifiers (UMIs) and an adapter. 5' ends of the cDNAs were extended by a template switch oligo (TSO) and after pooling of all samples full-length cDNA was amplified with primers binding to the TSO-site and the adapter. cDNA was tagmented with the Nextera XT DNA Library Preparation Kit and 3'-end-fragments finally amplified using primers with Illumina P5 and P7 overhangs. In comparison to Parekh *et al.*[181], the P5 and P7 sites were exchanged to allow sequencing of the cDNA in read1 and barcodes and UMIs in read2 to achieve a better cluster recognition. The library was sequenced on a NextSeq 500 (Illumina) with 63 cycles for the cDNA in read1 and 16 cycles for the barcodes and UMIs in read2.

Gencode gene annotations version 24 (version 28) and the human reference genome GRCh38 were derived from the Gencode homepage (EMBL-EBI). The Dropseq tools v1.12[182] was used for mapping raw sequencing data to the reference genome. The resulting UMI filtered count matrix was imported into R v3.4.4. To estimate the effect of treatment on parental and chemotherapy tolerant tumors, a dummy variable describing treatment and

tumor type was used for downstream differential expression analysis with DESeq2 v1.18.1[183]. Dispersion of the data was estimated with a parametric fit using the described dummy as parameter. The Wald test was used for determining differentially regulated genes between conditions. Shrunken log2 fold changes were calculated afterwards. A gene was determined to be differentially regulated if the absolute apeglm shrunken log2 fold change was at least 1 and the adjusted p-value was below 0.05. Rlog transformation of the data was performed for visualization and further downstream analysis. GSEA v4.0.3 was used to perform gene set enrichment analysis in the preranked mode using the apeglm shrunken log2 fold changes as ranking metric. A pathway was considered to be significantly associated with an experimental condition if the FDR was below 0.25.

4.13 Publicly available gene expression data

Gene expression data of COAD (colorectal adenocarcinoma) and READ (rectal adenocarcinoma) used for the comparison of *AURKA* gene expression between cancerous and normal tissues (Figure 26) were obtained from the National Cancer Institute's Genomic Data Commons The Cancer Genome Atlas (GDC-TCGA) datasets available via the UCSC Xena Browser (https://xenabrowser.net/)[184]. The GSE numbers of publicly available gene expression data of non-metastatic and metastatic primary CRCs as well as of normal colon, primary CRCs, and liver metastases of CRC used for the comparison of *AURKA* gene expression (Figure 38) are shown in the figure or figure legend and were derived from the NIH Gene Expression Omnibus.

4.14 Imaging

Processed slides from immunohistochemical analysis were scanned using the quantitative slide scanner Vectra Polaris™. Scanning was performed using the highest possible instrument setting (40-fold scan resolution). Snapshots of these scans were taken with the Phenochart 1.0.8 software.

PDTOs images were generated using an AZ100 Multizoom Microscope and NIS Elements D Imaging Software.

4.15 Statistical analysis

GraphPad Prism software (v7.01) was used for statistical analyses. For calculation of significant differences between two groups of biological replicates, a Student’s t-test (unpaired, two-tailed, Holm-Sidak method, with alpha level = 0.05) was applied. For the

comparison of three or more groups, a multiple comparison one-way ANOVA test was applied. In case of paired data (M0-M1 CRC cohort), a repeated measures ANOVA test combined with a Tukey's multiple comparison test was performed. For unpaired data, one-way ANOVA in combination with a Tukey's multiple comparisons test was performed. For comparison of data with two different parameters, a two-way ANOVA with either a Tukey's (when all samples were compared with each other) or Sidak's (when only certain treatments were compared with each other) multiple comparison test was performed. For calculation of correlation coefficients, Pearson's correlation analysis was applied. Statistical significance is indicated by asterisks in the figures and elucidated in the figure legends.

5 Results

5.1 Establishment of a colorectal cancer "living biobank"

We established a "living biobank" of PDTOs of primary CRCs and liver metastases of CRC. The tumor samples were derived from the Institute of Pathology of the LMU Munich in collaboration with Prof. Dr. Jens Neumann and Prof. Dr. Thomas Kirchner. Single cells were embedded in a three-dimensional basement membrane matrix mainly containing the extracellular matrix proteins laminin and collagen IV (Matrigel®). The embedded CRC cells were overlaid with a chemically defined and adjustable cell culture medium as described previously[162]. These PDTOs can be propagated *ex vivo* and kept in liquid nitrogen for long-term storage. A part of each primary tumor sample was also formalin-fixed and paraffin embedded for subsequent histological staining and characterization.

To study the effects of long-term treatment with chemotherapy, we chose the three PDTO lines 1, 2, and 5. They reflect the prototypic CRC that is capable of distant metastatic spread and is susceptible to first-line treatment with the chemotherapeutic regimen FOLFIRI plus the clinically approved anti-EGFR antibody Cmab. As summarized in Table 2, they displayed the following characteristics:

1. Derivative of liver metastatic CRC. While PDTO1 was derived from a liver metastatic primary CRC, PDTO2 and 5 were derived from liver metastases of CRC
2. Tumor grade 2 (moderately differentiated) as determined by HE staining (Figure 9)
3. Microsatellite stability (MSS)
4. Negativity for oncogenic mutations in *KRAS*, *NRAS*, *BRAF*, and *PIK3CA* according to pyrosequencing because mutations in these oncogenes would render the tumors tolerant towards Cmab treatment[95,96]
5. A similar mutational pattern in CRC driver genes, according to next generation gene panel sequencing, especially the loss of TP53 and truncating mutations in *APC*

These five features reflect typical hallmarks of CRCs, which are prone to metastasis formation and are eligible for treatment with FOLFIRI/Cmab.

Table 2: Characteristics of PDTO lines used in this study

PDTO line	Site of origin	*KRAS/ NRAS/ BRAF*	*PI3KCA*	*APC*	*TP53*	*SMAD2/3/4*	MSI/MSS	Histological grade
PDTO1	Primary tumor (liver metastatic)	wt	wt	mut	mut	wt	MSS	2
PDTO2	Liver metastasis	wt	wt	mut	mut	wt	MSS	2
PDTO5	Liver metastasis	wt	wt	mut	mut	wt	MSS	2
PDTO4	Primary tumor	$KRAS^{G12D}$	wt	mut	mut	SMAD2 mut	MSS	N.A.
PDTO17	Primary tumor	$KRAS^{G12R}$	wt	N.A.	N.A.	N.A.	MSS	N.A.

PDTO: patient-derived tumor organoid, wt: wild type, mut: mutant, MSI: microsatellite instable, MSS: microsatellite stable, N.A.: not available. PDTO1, 2, and 5 were used for the generation of FOLFIRI/Cmab tolerance.

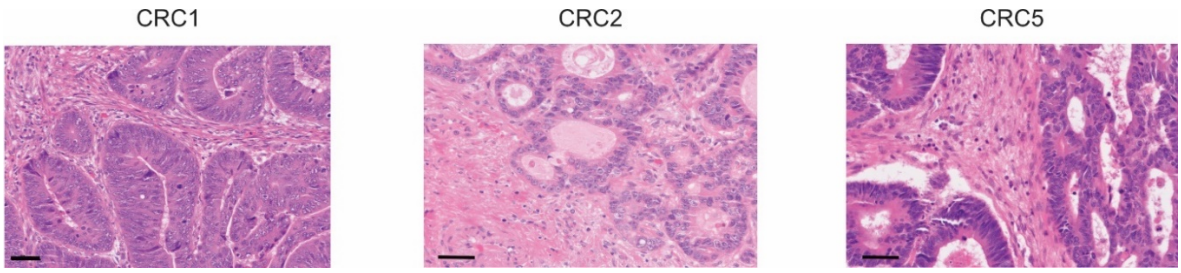

Figure 9: HE staining on FFPE tissue sections derived from CRC1, 2, 5

CRCs, from which the respective PDTO lines were generated. CRC1: primary tumor of a liver metastatic CRC, CRC2 and 5: liver metastases of CRC. Scale bars represent 50 µm.

5.2 *Ex vivo* chemotherapy tolerance modeling

We first analyzed the sensitivity of PDTO1 towards FOLFIRI. This chemotherapeutic regimen consists of folinic acid, 5-FU, and Irinotecan. Irinotecan is a prodrug that is metabolized into its active derivative SN-38 by esterases in liver cells and normal intestinal tissue[82]. Since these enzymes are not expected to be expressed at a sufficient level in our tumor organoid culture system, we compared the activity of Irinotecan and SN-38 in combination with 5-FU and folinic acid (FOLF), the two other components of FOLFIRI. As anticipated, FOLF alone decreased the cell viability (Figure 10A). However, the addition of 1 µM Irinotecan had no effect. In contrast, substitution of Irinotecan with equimolar amounts of SN-38 decreased the cell viability by an additional 61.5 % (Figure 10A). This confirms that Irinotecan cannot be sufficiently metabolized by the carcinoma cells of our PDTO lines and therefore does not affect the cell viability, but the active Irinotecan metabolite SN-38 is

able to decrease the viability substantially. Therefore, for all subsequent experiments we used the active metabolite SN-38 instead of Irinotecan in the FOLFIRI regimen.

Next, we examined the responsiveness of the three lines PDTO1, 2, and 5 to FOLFIRI/Cmab. The cell viability decreased in all three PDTO lines upon treatment with FOLFIRI, Cmab, or their combination (Figure 10B).

As a proof-of-concept that the sensitivity towards Cmab is reduced by an oncogenic mutation in *KRAS*, we included the $KRAS^{G12D}$ mutated PDTO4 in this experiment. Indeed, PDTO4 hardly responded to Cmab, which was in stark contrast to the other *KRAS* wild type PDTO lines (Figure 10B). However, the combination of FOLFIRI and Cmab still decreased the viability to 82.3 %.

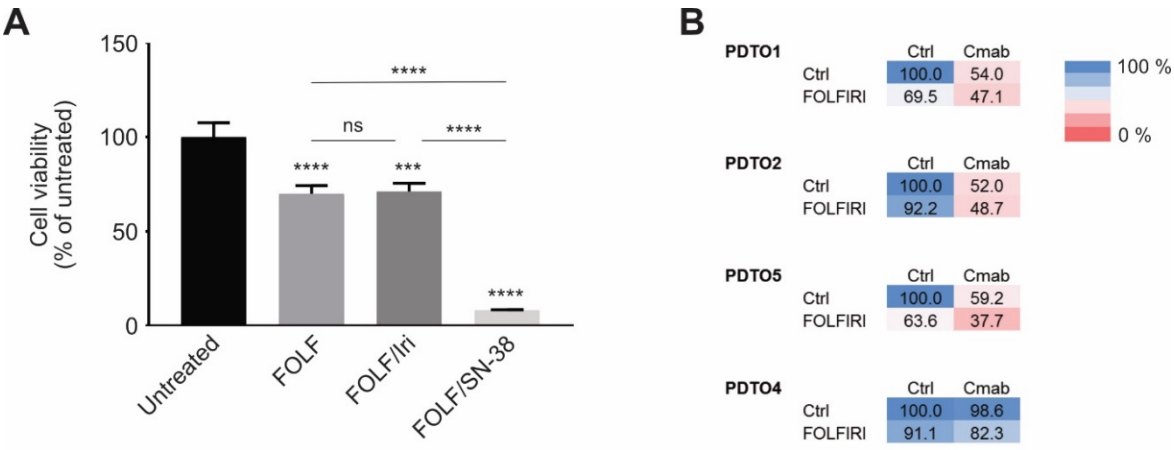

Figure 10: SN38 but not Irinotecan reduces the cell viability of PDTOs

A) Cell viability of PDTO1 was determined after 4 days of treatment with the indicated chemotherapeutics. FOLF: folinic acid plus 5-fluorouracil (5-FU); FOLF/Iri: folinic acid, 5-FU, and Irinotecan; FOLF/SN-38: folinic acid, 5-FU, and SN-38. Statistical significance was assessed by a one-way ANOVA in combination with Tukey's multiple comparisons test and is indicated by asterisks (***: p-value ≤ 0.001, ****: p-value ≤ 0.0001, ns: p-value > 0.05). Mean + SD, n = 3. **B)** Cell viability of PDTOs after 4 days of treatment with the indicated drugs. PDTO1, 2, and 5 are *KRAS* wild type while PDTO4 carries a $KRAS^{G12D}$ mutation. Mean, n = 3.

After we confirmed the responsiveness of the PDTOs towards FOLFIRI/Cmab, we performed a long-term treatment of the PDTOs with FOLFIRI/Cmab. The drug doses were adjusted to be partially sublethal, which achieved an equilibrium between cell killing and survival of drug persister cells over several PDTO passages. The concentrations were as follows: 625 nM 5-FU, 125 nM folinic acid, 0.5 nM SN-38, and 10 µg/mL Cmab. Notably, several pharmacokinetic studies have reported the plasma concentration of SN-38 of patients treated with 150 – 300 mg/m^2 Irinotecan to range between 1 and 10 nM[82,185,186]. Similarly,

the used doses of 5-FU and Cmab are in the range of the plasma concentrations of treated patients[187,188]. Therefore, the drug concentrations used here are similar to the therapeutic concentrations determined in the plasma of chemotherapy-exposed patients, which emphasizes the translational character and clinical relevance of our study.

Figure 11 shows the morphologic changes during the long-term treatment of the PDTOs. The evolution of tolerance development could be divided into three phases: In the first phase, treatment led to increased cell death as well as reduced cell viability and reseeding capacity within the first passages (approximately five weeks) in all PDTO lines, resulting in lower cell numbers than at the treatment start. Next, the treatment-exposed PDTO cultures entered a phase of stable equilibrium between cell death and growth, which resulted in stable, but low cell numbers. The third phase was marked by a recovery from the treatment and this was accompanied by increasing CRC cell yields up to a level sufficient for further analyses. This phase occurred at different time points after treatment start: For PDTO1 at approximately 4 months, for PDTO2 at 6 months and for PDTO5 at 5 months.

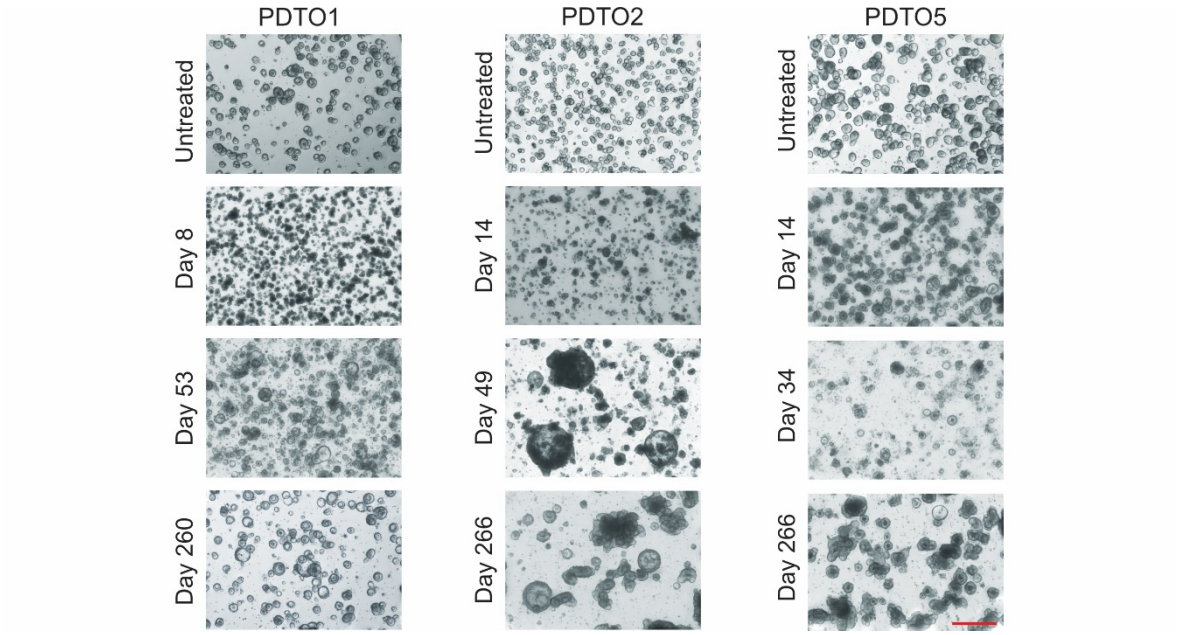

Figure 11: Morphologic changes of PDTOs during FOLFIRI/Cmab treatment

Microscopic images of PDTOs during chemotherapy tolerance generation. PDTOs were treated with FOLFIRI/Cmab for up to 9 months. The scale bar in the bottom right picture indicates 500 µm and is representative for all images.

5.3 PDTOs can acquire FOLFIRI/Cmab tolerance in the absence of mutations in *KRAS*, *NRAS*, *BRAF*, and *PIK3CA*

We aimed to show that the long-term treatment with FOLFIRI/Cmab led to the generation of chemotherapy tolerant PDTOs (CT-PDTOs) that are less sensitive to this drug regimen compared to their parental counterparts. Indeed, the cell viability, as assessed by the ATP-based CellTiter-Glo® 3D assay, was substantially more reduced in parental PDTOs by FOLFIRI/Cmab treatment than in the respective CT-PDTO derivatives. Notably, FOLFIRI/Cmab treatment led to a decrease in cell viability also in the treatment-adapted CT-PDTOs, which indicates an increased, but incomplete resistance towards this therapy.

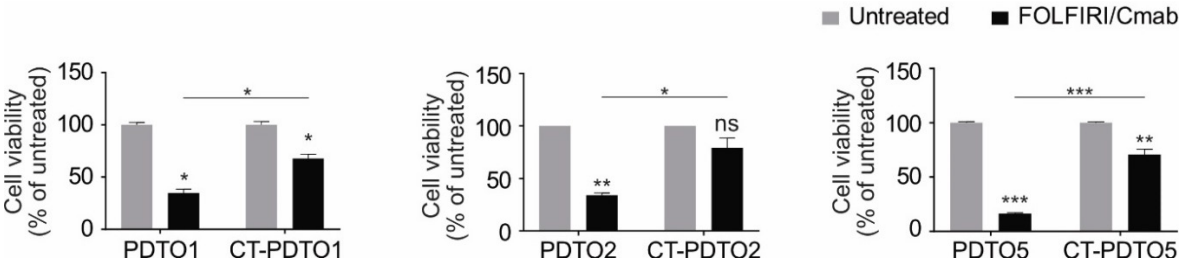

Figure 12: Cell viability is decreased further by FOLFIRI/Cmab in parental PDTOs than CT-PDTOs

Cell viability after 6 days (PDTO2 and 5) or 18 days (PDTO1, cells were passaged after 9 days) of treatment with FOLFIRI/Cmab. Statistical significance between all samples was assessed by a two-way ANOVA plus Tukey's multiple comparisons test and is indicated by asterisks (*: p-value ≤ 0.05, **: p-value ≤ 0.01, ***: p-value ≤ 0.001, ns: p-value > 0.05). Mean + SD, n = 2 for PDTO1, n = 3 for PDTO2 and 5.

To elucidate the effect of the FOLFIRI/Cmab treatment on the cell cycle behaviour, we pulsed CT-PDTO2 and its parental counterpart with the nucleoside analogue EdU and employed a whole DNA content stain (FxCycle) for FACS analysis (Figure 13). Both the parental PDTO2 and the CT-PDTO2 under control treatment showed the expected cell cycle distribution with cell populations in G1 (FxCycle low and EdU negative), S (EdU positive), and G_2/M phases (FxCycle high and EdU negative) (Figure 13A).

When PDTO2 and CT-PDTO2 were both cultured in the absence of chemotherapy, we detected approximately 16.1 and 35.8 % of cells in S phase, respectively (Figure 13B). This increased percentage of cells in S phase in the CT-PDTO2 population are in accordance to our observation that these cells proliferate faster than the parental PDTO2 when removing the chemotherapeutic regimen.

In parental PDTOs, FOLFIRI/Cmab treatment mostly led to a strongly compromised incorporation of EdU into the DNA, which indicates a typical chemotherapy-induced S phase arrest (28.6 %), and an increased fraction of cells in G_2/M phase. Only a small fraction of cells was EdU high, representative of a normal, active S phase. In contrast, CT-PDTO2 was less affected by the FOLFIRI/Cmab treatment: 27.4 % of cells were in normal S phase while only 10.8 % of cells were arrested in S phase. Compared to the untreated CT-PDTO2, an increased percentage of cells was also in G_2/M phase (Figure 13B).

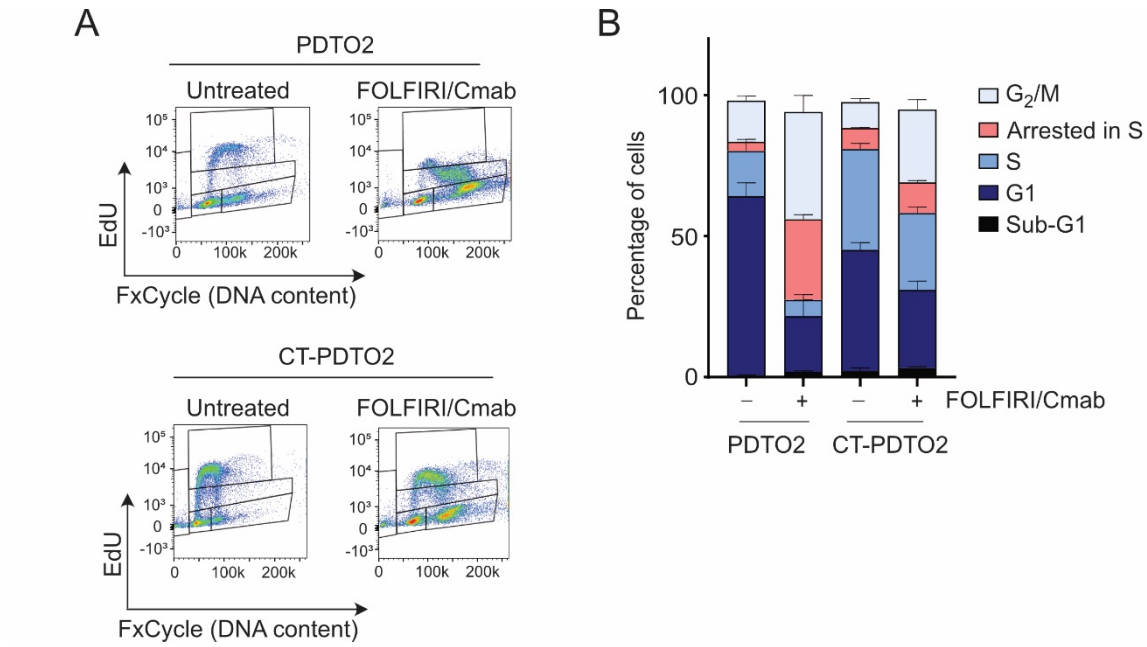

Figure 13: PDTO2 but not CT-PDTO2 shows an S phase arrest upon FOLFIRI/Cmab treatment

Established organoids were treated with FOLFIRI/Cmab for 48 h and subsequently pulsed with 10 µM EdU for 2 h and the DNA content was stained with FxCycle **A)** FACS plots of one representative experiment. **B)** Stacked bar graph of the FACS data. Note the discrimination between cells in normal S phase (middle blue) and cells arrested in S phase (red). Mean + SD, n = 3.

After we showed that CT-PDTO2 respond with higher viability and more cells in normal S phase to FOLFIRI/Cmab than the parental PDTO2, we inquired if this treatment would also provoke less apoptosis in the CT-PDTOs relative to their chemosensitive precursor organoid populations. To address this question, we performed immunoblot analyses of the three parental PDTO and CT-PDTO pairs with antibodies against the well-established apoptotic markers cleaved PARP and cleaved caspase 3. The parental PDTOs responded to FOLFIRI/Cmab with the expected PARP and caspase 3 cleavage. In contrast, the CT-PDTOs did not or to a lower extent respond with apoptosis to FOLFIRI/Cmab exposure (Figure 14). In summary, parental PDTOs but not the chemotherapy tolerant counterparts exhibited strongly reduced viability, an S phase arrest, and apoptosis upon FOLFIRI/Cmab treatment. Therefore, our analyses with different experimental approaches confirmed that the CT-PDTOs were more tolerant towards this first-line therapy regimen.

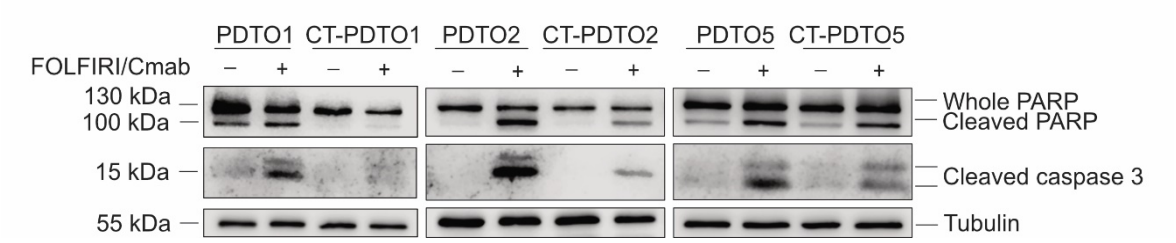

Figure 14: FOLFIRI/Cmab induces apoptosis in parental but not CT-PDTOs

Established organoids of parental PDTOs and their chemotolerant CT-PDTO counterparts were treated with FOLFIRI/Cmab for 48 h or left untreated, as indicated. Immunoblots of these samples were performed against whole and cleaved PARP as well as cleaved caspase 3. Cleavage of PARP and caspase 3 are markers for apoptosis. Alpha-tubulin was used as a loading control.

Mutations in key oncogenic drivers such as *KRAS*, *NRAS*, *BRAF*, or *PIK3CA* can lead to a partial or complete resistance towards FOLFIRI/Cmab[95,96]. Therefore, we compared the mutational status of these and other clinically relevant cancer driver genes before and after chemotherapy tolerance acquisition in our PDTO models. The Diagnostics Department of the Institute of Pathology of the LMU in collaboration with Dr. Jörg Kumbrink and Prof. Dr. Thomas Kirchner analyzed the mutational spectrum of PDTOs and CT-PDTOs via next generation panel sequencing with the Oncomine Comprehensive Assay Plus panel. This approach examines more than 500 genes relevant for today's precision oncology, including hotspot mutations, gene fusions, and copy number variations.

TP53 and *APC* were mutated in all parental PDTOs and CT-PDTOs (Table 3). In PDTO/CT-PDTO pairs 1 and 5, we detected five and four additional mutations, respectively, that were present in both the parental and the CT-PDTOs (Table 3).

Mutations in known resistance-conferring genes such as *KRAS*, *NRAS*, *BRAF,* or *PIK3CA* were not detected in any of the six PDTO lines. Only very few differences between the parental and the chemotherapy tolerant lines of a pair were seen: During the generation of chemo-tolerance, PDTO1 gained mutations in *COL11A1*, *OR8U1*, and *DICER1* while a mutation in *PPFIA2* was present only in the parental PDTO1. The treatment also selected against a mutant *TNFAIP3* allele in PDTO2 and *OR6F1* in PDTO5. No therapy-relevant gene fusions had occurred in CT-PDTOs during long-term drug exposure and adaptation.

Since the here detected genetic alterations have not been described in connection to a resistance towards FOLFIRI/Cmab, they are unlikely to have caused the tolerance towards this drug regimen in the CT-PDTOs. This suggests that alternative tolerance-conferring mechanisms are responsible for the here observed adaptation of CRC PDTOs to long-term FOLFIRI/Cmab exposure.

Table 3: Panel sequencing of PDTOs and CT-PDTOs (continued to next page)

Chromosomal position	Gene (HUGO)	cDNA	Type	Exon	Reference mRNA	Protein	Coverage	Allele freq.
PDTO1								
chr1:97547947	*DPYD*	c.2846A>T	SNV	22	NM_000110.3	p.Asp949Val	1996	65.68
chr5:112173917	*APC*	c.2626C>T	SNV	16	NM_000038.5	p.Arg876Ter	1036	44.5
chr5:112174094	*APC*	c.2804_2805insA	INDEL	16	NM_000038.5	p.Tyr935Ter	1315	50.34
chr6:28227363	*NKAPL*	c.214C>T	SNV	1	NM_001007531.2	p.Arg72Ter	1586	31.53
chr7:53104030	*POM121L12*	c.666A>C	SNV	1	NM_182595.3	p.Lys222Asn	731	52.67
chr8:114326980	*CSMD3*	c.221G>A	SNV	2	NM_198123.1	p.Gly74Asp	1477	26.13
chr8:114326983	*CSMD3*	c.218A>G	SNV	2	NM_198123.1	p.Asn73Ser	1479	26.17
chr12:81799639	***PPFIA2***	**c.688_689insC**	**INDEL**	**8**	**NM_003625.4**	**p.Met230ThrfsTer14**	**628**	**13.22**
chr17:7577538	*TP53*	c.743G>A	SNV	7	NM_000546.5	p.Arg248Gln	1031	99.9
chr19:52715982	*PPP2R1A*	c.547C>T	SNV	5	NM_014225.5	p.Arg183Trp	674	65.43
CT-PDTO1								
chr1:97547947	*DPYD*	c.2846A>T	SNV	22	NM_000110.3	p.Asp949Val	1997	68.6
chr1:103428216	***COL11A1***	**c.3017G>C**	**SNV**	**39**	**NM_001854.3**	**p.Gly1006Ala**	**1579**	**34.83**
chr5:112173917	*APC*	c.2626C>T	SNV	16	NM_000038.5	p.Arg876Ter	1092	34.8
chr5:112174094	*APC*	c.2804_2805insA	INDEL	16	NM_000038.5	p.Tyr935Ter	1386	67.32
chr6:28227363	*NKAPL*	c.214C>T	SNV	1	NM_001007531.2	p.Arg72Ter	1747	34.92
chr7:53104030	*POM121L12*	c.666A>C	SNV	1	NM_182595.3	p.Lys222Asn	948	50.74
chr8:114326980	*CSMD3*	c.221G>A	SNV	2	NM_198123.1	p.Gly74Asp	1182	32.32
chr8:114326983	*CSMD3*	c.218A>G	SNV	2	NM_198123.1	p.Asn73Ser	1181	32.09
chr11:56143344	***OR8U1***	**c.245T>C**	**SNV**	**1**	**NM_001013356.2, NM_001005204.1**	**p.Leu82Pro**	**1368**	**12.5**
chr14:95572504	***DICER1***	**c.2861T>G**	**SNV**	**20**	**NM_030621.4**	**p.Leu954Arg**	**1100**	**23.64**
chr17:7577538	*TP53*	c.743G>A	SNV	7	NM_000546.5	p.Arg248Gln	1376	99.93
chr19:52715982	*PPP2R1A*	c.547C>T	SNV	5	NM_014225.5	p.Arg183Trp	847	66.94

Table 3 (continued): Panel sequencing of PDTOs and CT-PDTOs

Chromosomal position	Gene (HUGO)	cDNA	Type	Exon	Reference mRNA	Protein	Coverage	Allele freq.
PDTO2								
chr5:112173869	*APC*	c.2579delT	INDEL	16	NM_000038.5	p.Leu860GlnfsTer56	1995	63.26
chr5:112175734	*APC*	c.4446_4455delTCCAGATGCT	INDEL	16	NM_000038.5	p.Pro1483IlefsTer21	1981	33.01
chr6:138199926	***TNFAIP3***	**c.1344G>A**	**SNV**	**7**	**NM_001270507.1**	**p.Trp448Ter**	**1820**	**29.73**
chr17:7577557	*TP53*	c.723delC	INDEL	7	NM_000546.5	p.Cys242AlafsTer5	1688	100
CT-PDTO2								
chr5:112173869	*APC*	c.2579delT	INDEL	16	NM_000038.5	p.Leu860GlnfsTer56	1996	28.66
chr5:112175734	*APC*	c.4446_4455delTCCAGATGCT	INDEL	16	NM_000038.5	p.Pro1483IlefsTer21	1982	67.66
chr17:7577557	*TP53*	c.723delC	INDEL	7	NM_000546.5	p.Cys242AlafsTer5	1991	99.95
PDTO5								
chr1:247875339	***OR6F1***	**c.719C>T**	**SNV**	**1**	**NM_001005286.1**	**p.Thr240Met**	**2000**	**33.1**
chr3:1427413	*CNTN6*	c.2636T>A	SNV	20	NM_014461.3	p.Val879Glu	1169	34.73
chr4:187542357	*FAT1*	c.5383C>T	SNV	10	NM_005245.3	p.Arg1795Ter	1998	50.4
chr5:41201759	*C6*	c.200delA	INDEL	3	NM_000065.3	p.Lys67SerfsTer56	1545	100
chr5:112173917	*APC*	c.2626C>T	SNV	16	NM_000038.5	p.Arg876Ter	1253	99.92
chr10:8115852	*GATA3*	c.1201A>G	SNV	6	NM_001002295.1	p.Met401Val	1520	31.32
chr17:7577094	*TP53*	c.844C>T	SNV	8	NM_000546.5	p.Arg282Trp	2000	99.65
CT-PDTO5								
chr3:1427413	*CNTN6*	c.2636T>A	SNV	20	NM_014461.3	p.Val879Glu	1417	54.06
chr4:187542357	*FAT1*	c.5383C>T	SNV	10	NM_005245.3	p.Arg1795Ter	1999	49.92
chr5:41201759	*C6*	c.200delA	INDEL	3	NM_000065.3	p.Lys67SerfsTer56	1990	100
chr5:112173917	*APC*	c.2626C>T	SNV	16	NM_000038.5	p.Arg876Ter	1678	99.52
chr10:8115852	*GATA3*	c.1201A>G	SNV	6	NM_001002295.1	p.Met401Val	1998	29.18
chr17:7577094	*TP53*	c.844C>T	SNV	8	NM_000546.5	p.Arg282Trp	2000	99.65

Results from the Oncomine Comprehensive Assay Plus panel of PDTO1, 2, and 5 and their FOLFIRI/Cmab-tolerant derivatives (CT-PDTO1, 2, 5). Genetic alterations detected in only one line of the PDTO/CT-PDTO pairs are indicated in **bold**. SNV: single nucleotide variant, INDEL: insertion or deletion. Panel sequencing was performed by the Diagnostics Department of the Institute of Pathology and data analysis was performed by Dr. Kumbrink (LMU Munich).

5.4 Acquisition of FOLFIRI/Cmab tolerance is accompanied by an adaptation of the global gene expression in CT-PDTOs

Since we did not detect genetic events that could explain the acquired tolerance towards FOLFIRI/Cmab in CT-PDTOs, we hypothesized that these changes were more likely to have occurred on the gene expression level. To test this hypothesis, we performed unbiased transcriptome analysis (next generation RNA sequencing) in collaboration with Dr. Rupert Öllinger (library preparation and sequencing run), Thomas Engleitner (primary data analysis), and Prof. Dr. Roland Rad (coordination, all Technical University Munich). We compared the parental PDTOs maintained in control medium in the absence of chemotherapeutics with the CT-PDTOs under the influence of FOLFIRI/Cmab medium, to which they had been adapted for several months.

The volcano plots in Figure 15 show the adjusted p-value of each differentially expressed gene in dependence of the $\log_2$ fold change between FOLFIRI/Cmab-treated CT-PDTOs and parental PDTOs.

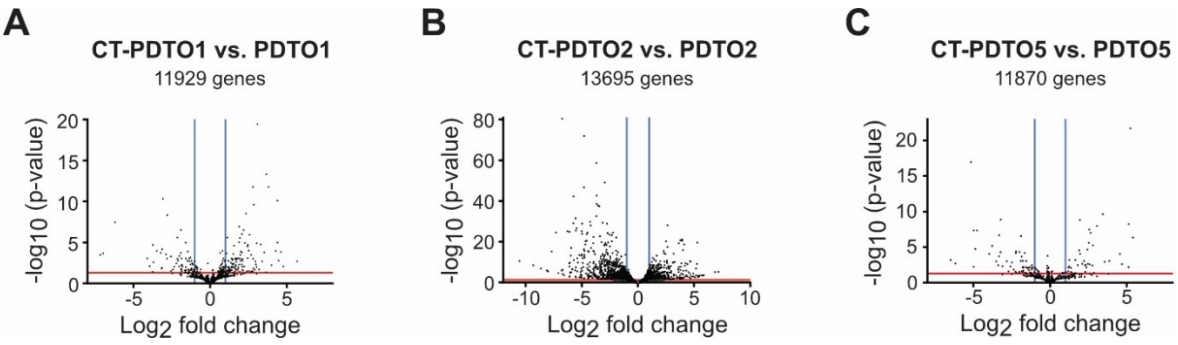

Figure 15: Volcano plots of the next generation RNA sequencing data

Expression changes between CT-PDTO and parental PDTO pairs. Red horizontal line indicates $-\log_{10}$(p-value) = 1.30, which equals a p-value of 0.05. The p-value was adjusted for multiple testing. Blue vertical lines indicate a $\log_2$ fold change in expression of 1 or -1. RNA sequencing was performed in collaboration with Dr. Rupert Öllinger, Thomas Engleitner, and Prof. Dr. Roland Rad.

The total numbers of detected mRNAs among the three PDTO/CT-PDTO pairs were similar (11929, 13695, and 11870 mRNAs for the PDTO/CT-PDTO pairs 1, 2, and 5, respectively; Figure 15). In contrast, the number of genes differentially expressed at a significant level between each PDTO and the respective CT-PDTO derivative varied tremendously between the patients. The PDTO2/CT-PDTO2 organoid pair showed the greatest number of differentially expressed genes (Figure 16).

To find shared features of the CT-PDTOs, we assessed the overlap of differentially expressed genes in the three chemotherapy-adapted organoid lines. Only seven genes were upregulated and seventeen genes downregulated simultaneously in all three CT-PDTOs compared to their respective parental counterparts (Figure 16). These seven upregulated and seventeen downregulated genes are listed in Table 4 and Table 5, respectively.

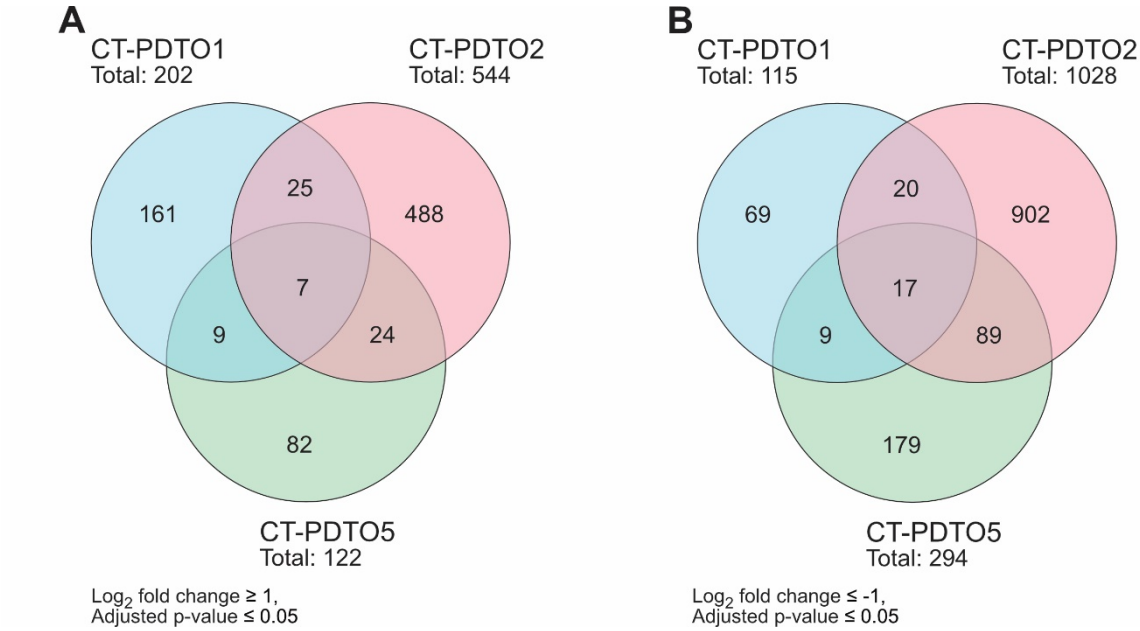

Figure 16: Differentially expressed genes in CT-PDTOs vs. PDTOs

A) Number of significantly upregulated genes (adjusted p-value ≤ 0.05, log_2 fold change ≥ 1) in each FOLFIRI/Cmab-treated CT-PDTO compared to the parental counterpart and the overlap between the different organoid lines. Total number of significantly upregulated genes for each PDTO pair is indicated. **B)** Number of significantly downregulated genes (adjusted p-value ≤ 0.05, log_2 fold change ≤ -1) in each FOLFIRI/Cmab-treated CT-PDTO compared to the parental counterpart and the overlap between the different organoid lines. Total number of significantly downregulated genes for each PDTO pair is indicated. RNA sequencing was performed in collaboration with Dr. Rupert Öllinger, Thomas Engleitner, and Prof. Dr. Roland Rad.

Table 4: Genes that are upregulated in all three CT-PDTOs

	CT-PDTO1	CT-PDTO2	CT-PDTO5
TBX2	4.01	3.69	4.55
OLFM4	3.03	4.92	2.33
SLC29A1	2.08	2.64	1.84
MT1G	1.18	1.48	3.92
TMEM171	2.05	2.55	1.30
SULT2A1	1.68	5.36	3.09
CDCA7	1.38	2.45	1.50

The seven genes that were upregulated in all three FOLFIRI/Cmab-treated CT-PDTOs compared to the parental counterparts and their log_2-fold gene expression changes. RNA sequencing was performed in collaboration with Dr. Rupert Öllinger, Thomas Engleitner, and Prof. Dr. Roland Rad.

Table 5: Genes that are downregulated in all three CT-PDTOs

	CT-PDTO1	CT-PDTO2	CT-PDTO5
KLK6	-1.91	-3.82	-1.28
CST7	-3.23	-4.98	-2.79
LGALS1	-2.82	-3.89	-2.00
IGFL2-AS1	-2.29	-4.37	-4.79
CST1	-3.24	-4.00	-4.61
HOXA10	-1.96	-2.86	-4.60
ACSS2	-1.09	-1.15	-1.16
CST4	-3.50	-5.36	-3.52
HOXA11-AS	-3.29	-2.68	-4.21
SERPINE2	-1.58	-1.37	-1.57
NDRG1	-2.36	-3.07	-2.49
EFNB2	-2.02	-2.08	-2.37
SLC16A3	-2.23	-1.82	-2.60
CDKN1C	-1.66	-1.36	-3.10
EPHB6	-2.79	-5.83	-1.38
C3orf85	-4.64	-1.17	-2.83
H1F0	-1.74	-1.60	-2.31

The seventeen genes that were downregulated in all three FOLFIRI/Cmab-treated CT-PDTOs compared to the parental counterparts and their log_2-fold gene expression changes. RNA sequencing was performed in collaboration with Dr. Rupert Öllinger, Thomas Engleitner, and Prof. Dr. Roland Rad.

To confirm these RNA sequencing results, we performed quantitative real-time PCR (qRT-PCR). Indeed, the seven genes that were upregulated in the treated CT-PDTOs compared to the parental PDTOs according to next generation RNA sequencing could be validated by qRT-PCR. We also confirmed one of the downregulated genes via qRT-PCR, namely *NDRG1* (Figure 17).

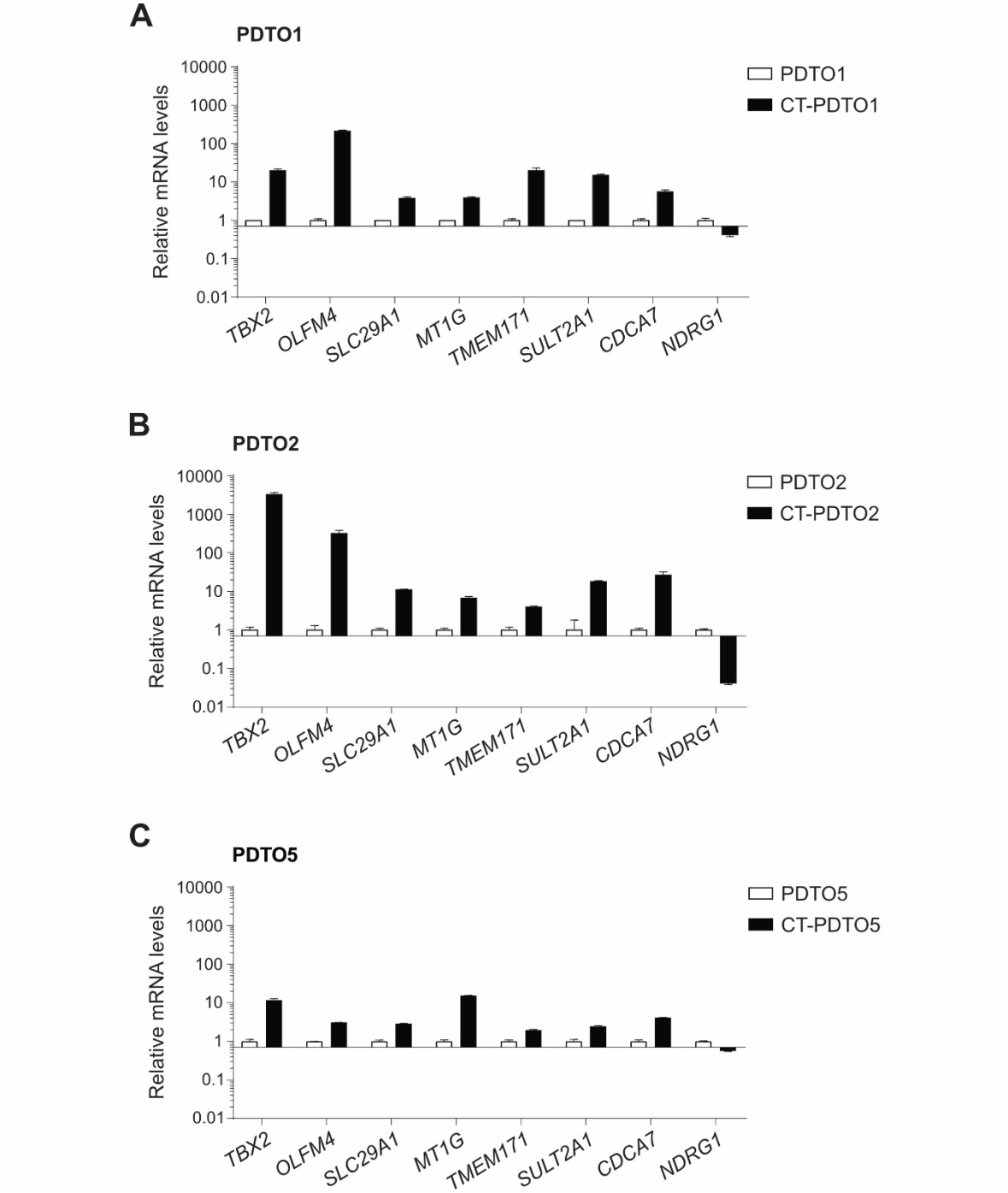

Figure 17: qRT-PCR confirmation of next generation RNA sequencing results

The seven genes that were upregulated and one gene that was downregulated (*NDRG1*) according to the RNA sequencing data in all three CT-PDTOs compared to their parental counterparts were confirmed by qRT-PCR. PDTOs were left untreated, while CT-PDTOs were maintained under FOLFIRI/Cmab treatment until harvest. The expression levels were normalized to the expression of *GAPDH* and *PPIA*. Mean + SD of technical triplicates are indicated for each PDTO line.

Since the CT-PDTO models displayed a large heterogeneity of gene expression changes on the single gene level, we assessed the chemotherapy adaptation-accompanied changes not only on the single gene level, but also on a signaling pathway scale. To achieve this, we performed gene set enrichment analyses (GSEA)[189] with the publicly available Hallmark gene sets (Molecular Signatures Database (MSigDB) Collections, Broad Institute[190]). This GSEA utilizes a list of differentially expressed genes from the RNA sequencing, which has been ranked according to the fold change or p-value. It is then examined whether genes that are relevant for a certain pathway accumulate at the top or bottom of this list of differentially expressed genes[189].

No gene sets were significantly upregulated simultaneously in all three CT-PDTOs compared to their parental counterparts at an FDR q-value (false discovery rate) of below 0.25 (Figure 18).

The commonalities shared between the two liver metastasis-derived CT-PDTO2 and CT-PDTO5 were the greatest: Four gene sets were upregulated in both tumor organoid lines upon chemotherapy tolerance acquisition (Figure 18). CT-PDTO2 and CT-PDTO5 gene expression profiles were enriched in the Hallmarks “E2F targets”, “G_2/M checkpoint”, and two different MYC target gene sets (Figure 18, Table 6).

None of these gene sets were enriched in CT-PDTO1 when compared to the parental PDTO1. There was an overlap between the PDTO1 and 2, which consisted of the Hallmark gene set “Interferon alpha response” (Figure 18, Table 6). In agreement with these data, an increased antiviral response gene expression of type I interferons has been described previously to confer resistance to EGFR inhibition by Erlotinib in non-small cell lung cancer[191].

Figure 19 displays the GSEA plots for enriched gene sets. Figure 20 shows four representative heat maps of the leading edge subsets of the enriched Hallmark gene sets for CT-PDTO2 versus PDTO2. The leading edge subset contains the genes of a gene set that contribute most to the enrichment score[189]. These genes lead to the increase in the enrichment score and appear before the maximum of the enrichment score curve (also called the running sum) in case of a positive enrichment[189].

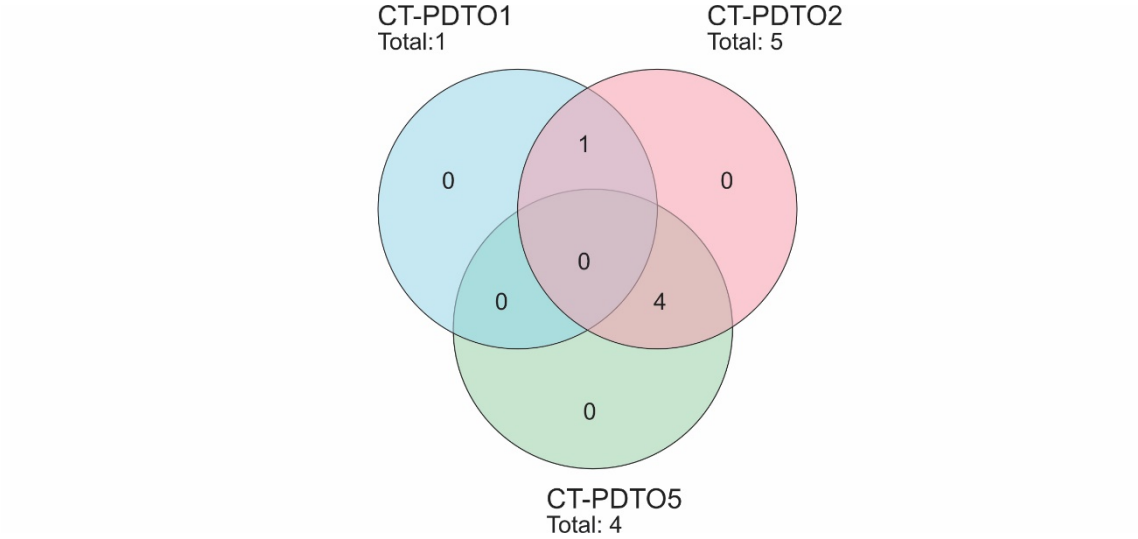

Figure 18: Upregulated Hallmark gene sets in CT-PDTO lines

Numbers of significantly upregulated Hallmark gene sets according to an FDR q-value < 0.25 in each FOLFIRI/Cmab-treated CT-PDTO compared to the parental counterpart and the overlap between the different organoid lines. The total number of upregulated Hallmark gene sets is indicated for every PDTO/CT-PDTO pair. RNA sequencing was performed in collaboration with Dr. Rupert Öllinger, Thomas Engleitner, and Prof. Dr. Roland Rad.

Table 6: Upregulated Hallmark gene sets in CT-PDTO lines

PDTO line	Gene set	NES	NOM p-val	FDR q-val
CT-PDTO1	**Interferon alpha response**	1.541	0.020	0.216
CT-PDTO2	**MYC targets V1**	2.142	0.000	0.000
	E2F targets	1.954	0.000	0.001
	MYC targets V2	1.874	0.000	0.001
	Interferon alpha response	1.586	0.004	0.020
	G_2/M checkpoint	1.280	0.025	0.160
CT-PDTO5	**E2F targets**	1.947	0.000	0.000
	G_2/M checkpoint	1.736	0.005	0.012
	MYC targets V2	1.371	0.070	0.151
	MYC targets V1	1.318	0.038	0.161

NES: normalized enrichment score, NOM p-val: nominal p-value, FDR q-val: false discovery rate. Shown are the significantly upregulated Hallmark gene sets with an FDR q-val < 0.25. Gene sets that are also significantly upregulated in at least one other CT-PDTO are highlighted in **bold**. RNA sequencing was performed in collaboration with Dr. Rupert Öllinger, Thomas Engleitner, and Prof. Dr. Roland Rad.

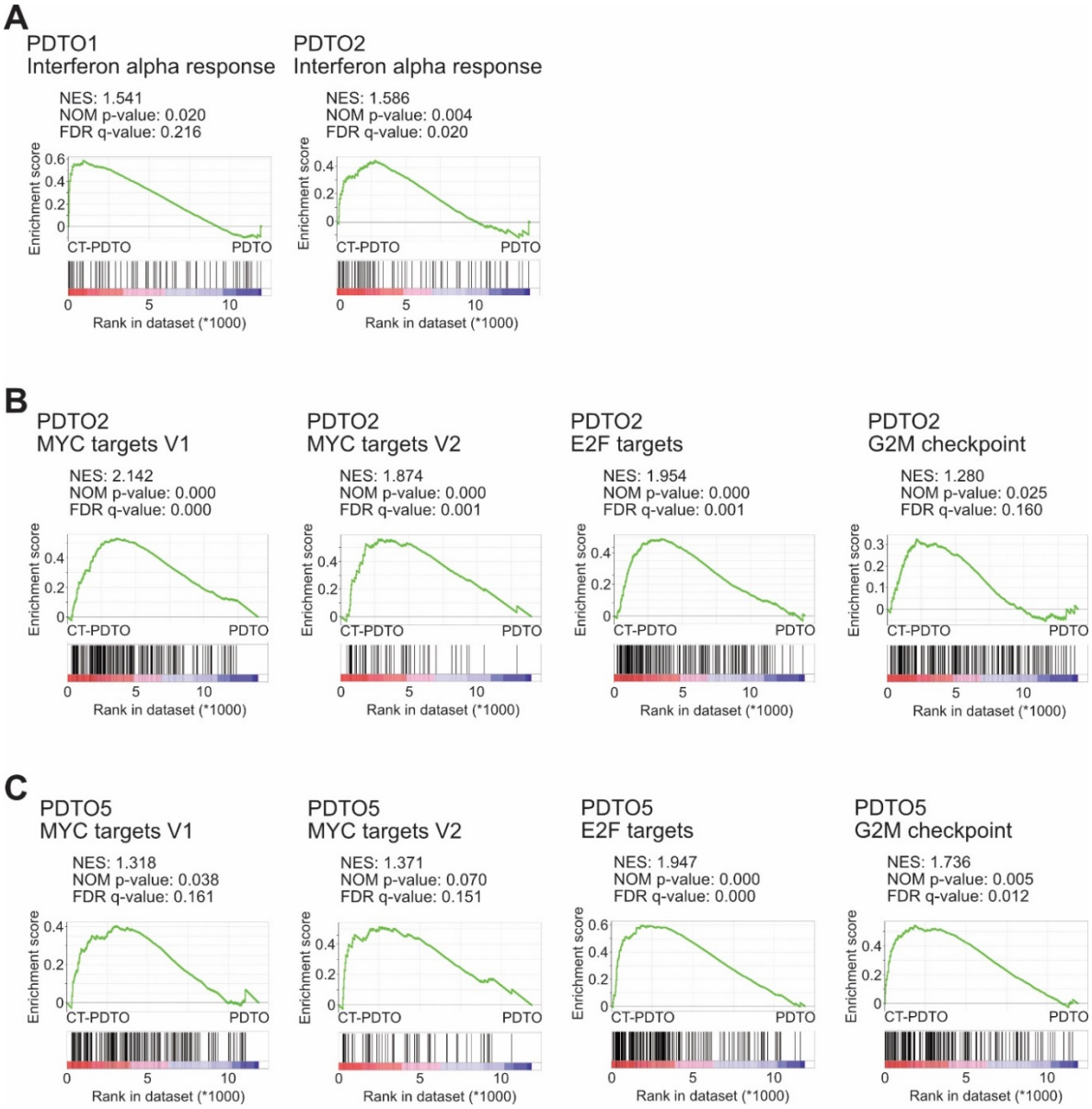

Figure 19: Gene set enrichment analysis plots of the Hallmarks augmented in CT-PDTOs

Gene set enrichment analysis (GSEA) of FOLFIRI/Cmab-treated CT-PDTOs versus untreated parental PDTOs with the Hallmark gene sets (MSigDB Collections, Broad Institute[190]). Shown are the gene sets that reached statistical significance at an FDR < 0.25. NES: normalized enrichment score, NOM p-value: nominal p-value, FDR q-value: false discovery rate. RNA sequencing was performed in collaboration with Dr. Rupert Öllinger, Thomas Engleitner, and Prof. Dr. Roland Rad.

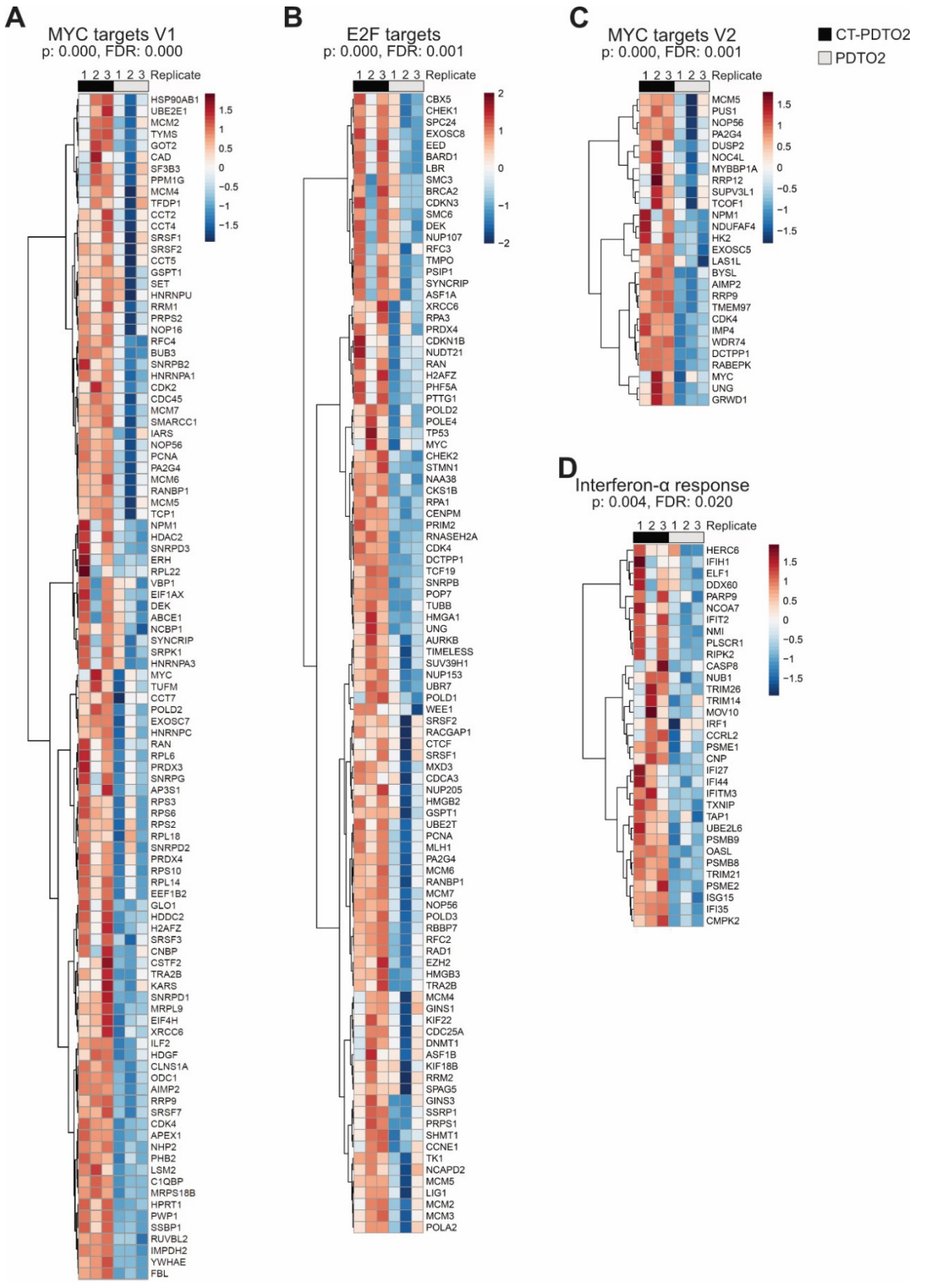

Figure 20: Heat maps of the leading edge genes contained in the augmented Hallmark gene sets in CT-PDTO2 versus PDTO2

Shown are the heat maps of the leading edge subsets of the four statistically most significant Hallmark gene sets (MSigDB Collections, Broad Institute[190]) for CT-PDTO2 vs. PDTO2 of three replicates each. RNA sequencing was performed in collaboration with Dr. Rupert Öllinger, Thomas Engleitner, and Prof. Dr. Roland Rad.

With a focus on CT-PDTO2 and CT-PDTO5, we analyzed whether the enriched MYC target gene sets were also accompanied by elevated MYC protein levels. To elucidate this, we performed immunoblot analysis and observed that compared to their parental PDTOs, CT-PDTO2 and 5 indeed showed increased levels of MYC protein. The higher MYC levels occurred independently of whether the chemotherapy adapted CT-PDTOs had been cultured in FOLFIRI/Cmab-containing medium before the harvest for lysate generation (Figure 21). In contrast, CT-PDTO1 exhibited a decrease in MYC protein level compared to the parental PDTO1 and downmodulation of MYC when exposed to combination chemotherapy (Figure 21).

Therefore, the immunoblot analysis data underscore the observation of an increased MYC target signature generated by GSEA in CT-PDTO2 and 5, but not CT-PDTO1.

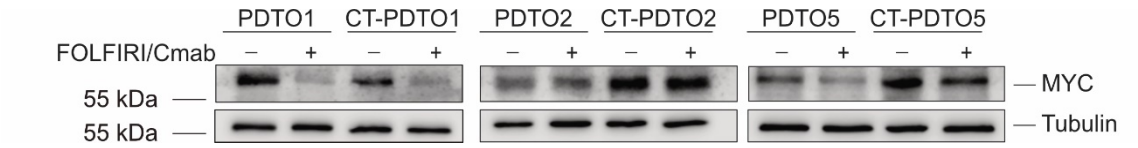

Figure 21: MYC expression is increased in CT-PDTO2 and 5

Established organoids of parental PDTOs and their chemotherapy adapted CT-PDTO counterparts were treated with FOLFIRI/Cmab for 48 h or left untreated, as indicated. Immunoblots of these samples were performed against MYC. Alpha-tubulin was used as a loading control.

Moreover, the GSEA data showed that all three CT-PDTOs decreased the expression of the two Hallmark gene sets “Hypoxia” and “Apoptosis” compared to their untreated parental PDTOs (Figure 22, Table 7).

The downregulation of the Hallmarks gene set “Apoptosis” is especially noteworthy since it demonstrates that the CT-PDTOs show a lower expression of apoptotic markers when exposed to the initially apoptosis-inducing therapy FOLFIRI/Cmab in comparison to the parental PDTOs in the absence of chemotherapeutic stress. Simultaneously, it validates our observation from the immunoblot experiments, which showed that the CT-PDTOs do not or to a lesser extent display the apoptotic markers cleaved caspase 3 and cleaved PARP upon drug exposure when compared to the parental PDTOs (Figure 14).

The downregulation of hypoxia-associated factors is in not in agreement with previously published studies, which mostly showed that hypoxia-inducible factors are implicated in the development of resistance to chemotherapy as well as EGFR inhibitors[192] (reviewed in[193]).

CT-PDTO1 showed a downregulation of the Hallmark gene set MYC targets V1 (Table 7), which was upregulated in the two other CT-PDTOs (Table 6). This further confirms our

hypothesis that the PDTO1 developed the tolerance towards FOLFIRI/Cmab through a different mechanism than PDTO2 and 5.

Additionally downregulated Hallmarks gene sets, which do not form part of the topic of this study, are listed in Table 7.

Figure 23 shows the enrichment plots of the Hallmark gene sets “Apoptosis” and “Hypoxia”, which were downregulated in all three CT-PDTO lines in respect to their parental PDTO counterparts. The respective heat maps of the leading edge genes of these Hallmark gene sets are shown in Figure 24 representatively for the PDTO2/CT-PDTO2 pair.

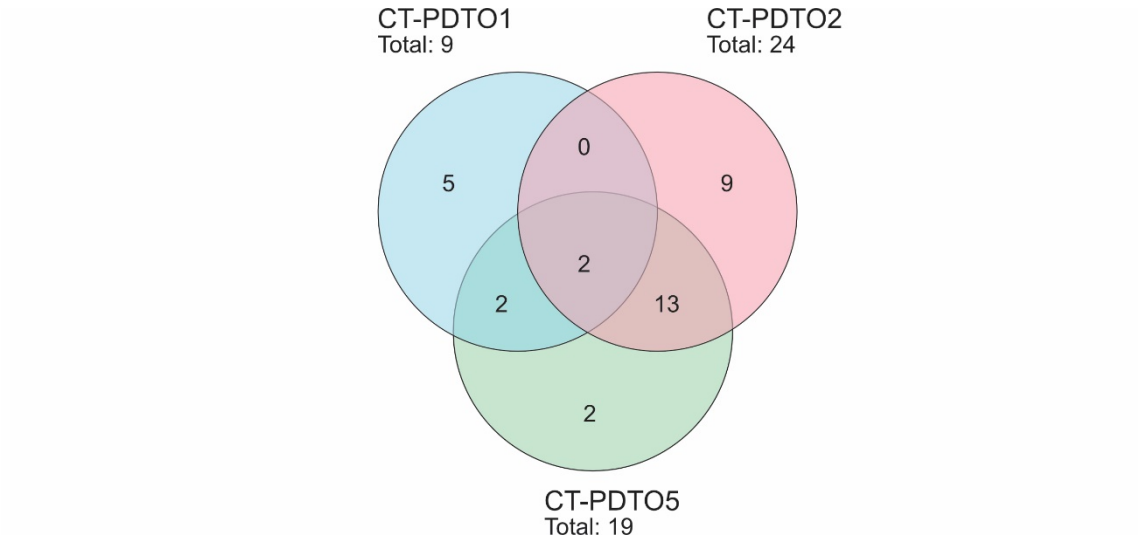

Figure 22: Downregulated Hallmark gene sets

Numbers of significantly downregulated Hallmark gene sets according to an FDR q-value < 0.25 in each FOLFIRI/Cmab-treated CT-PDTO compared to the parental counterpart and the overlap between the different organoid lines. The total number of downregulated Hallmark gene sets is indicated for every PDTO/CT-PDTO pair. RNA sequencing was performed in collaboration with Dr. Rupert Öllinger, Thomas Engleitner, and Prof. Dr. Roland Rad.

Table 7: Downregulated Hallmark gene sets in CT-PDTO lines

PDTO line	Gene set	NES	NOM p-val	FDR q-val
CT-PDTO1	**Hypoxia**	-1.980	0.000	0.000
	Cholesterol homeostasis	-1.975	0.000	0.001
	MTORC1 Signaling	-1.858	0.000	0.005
	Glycolysis	-1.870	0.000	0.005
	Apoptosis	-1.593	0.007	0.053
	Unfolded protein response	-1.374	0.042	0.166
	Androgen response	-1.349	0.071	0.172
	MYC targets V1	-1.387	0.007	0.175
	Fatty acid metabolism	-1.393	0.028	0.198
	IL2 STAT5 signaling	-1.257	0.076	0.274
CT-PDTO2	Epithelial mesenchymal transition	-1.905	0.000	0.000
	Hypoxia	-1.859	0.000	0.001
	TGF beta signaling	-1.779	0.000	0.003
	Hedgehog signaling	-1.644	0.011	0.012
	Complement	-1.647	0.000	0.013
	IL2 STAT5 signaling	-1.649	0.001	0.014
	UV response dn	-1.600	0.001	0.015
	KRAS signaling up	-1.657	0.000	0.015
	p53 Pathway	-1.602	0.001	0.016
	TNFA signaling via NFkB	-1.676	0.000	0.016
	Inflammatory response	-1.588	0.005	0.016
	Coagulation	-1.604	0.004	0.017
	Apoptosis	-1.549	0.001	0.025
	Estrogen response early	-1.533	0.002	0.027
	Myogenesis	-1.413	0.020	0.075
	Protein secretion	-1.422	0.022	0.077
	Apical junction	-1.351	0.058	0.114
	Estrogen response late	-1.260	0.105	0.194
CT-PDTO5	**Apoptosis**	-1.814	0.000	0.001
	Estrogen response early	-1.739	0.000	0.010
	IL2 STAT5 signaling	-1.677	0.003	0.021
	Glycolysis	-1.603	0.001	0.031
	p53 pathway	-1.621	0.003	0.031
	Inflammatory response	-1.625	0.005	0.035
	Estrogen response late	-1.560	0.005	0.056
	Hypoxia	-1.531	0.008	0.059
	Coagulation	-1.542	0.020	0.063
	TNFA signaling via NFkB	-1.533	0.008	0.064
	TGF beta signaling	-1.505	0.028	0.073
	Complement	-1.441	0.028	0.127
	UV response dn	-1.416	0.051	0.147
	Androgen response	-1.388	0.058	0.155
	Apical junction	-1.389	0.048	0.164
	Myogenesis	-1.310	0.097	0.242
	Protein secretion	-1.301	0.121	0.244

NES: normalized enrichment score, NOM p-val: nominal p-value, FDR q-value: false discovery rate. Shown are the top 10 significantly downregulated Hallmark gene sets plus all gene sets that were downregulated simultaneously in at least 2 CT-PDTOs (highlighted in **bold**) with an FDR q-val < 0.25. RNA sequencing was performed in collaboration with Dr. Rupert Öllinger, Thomas Engleitner, and Prof. Dr. Roland Rad.

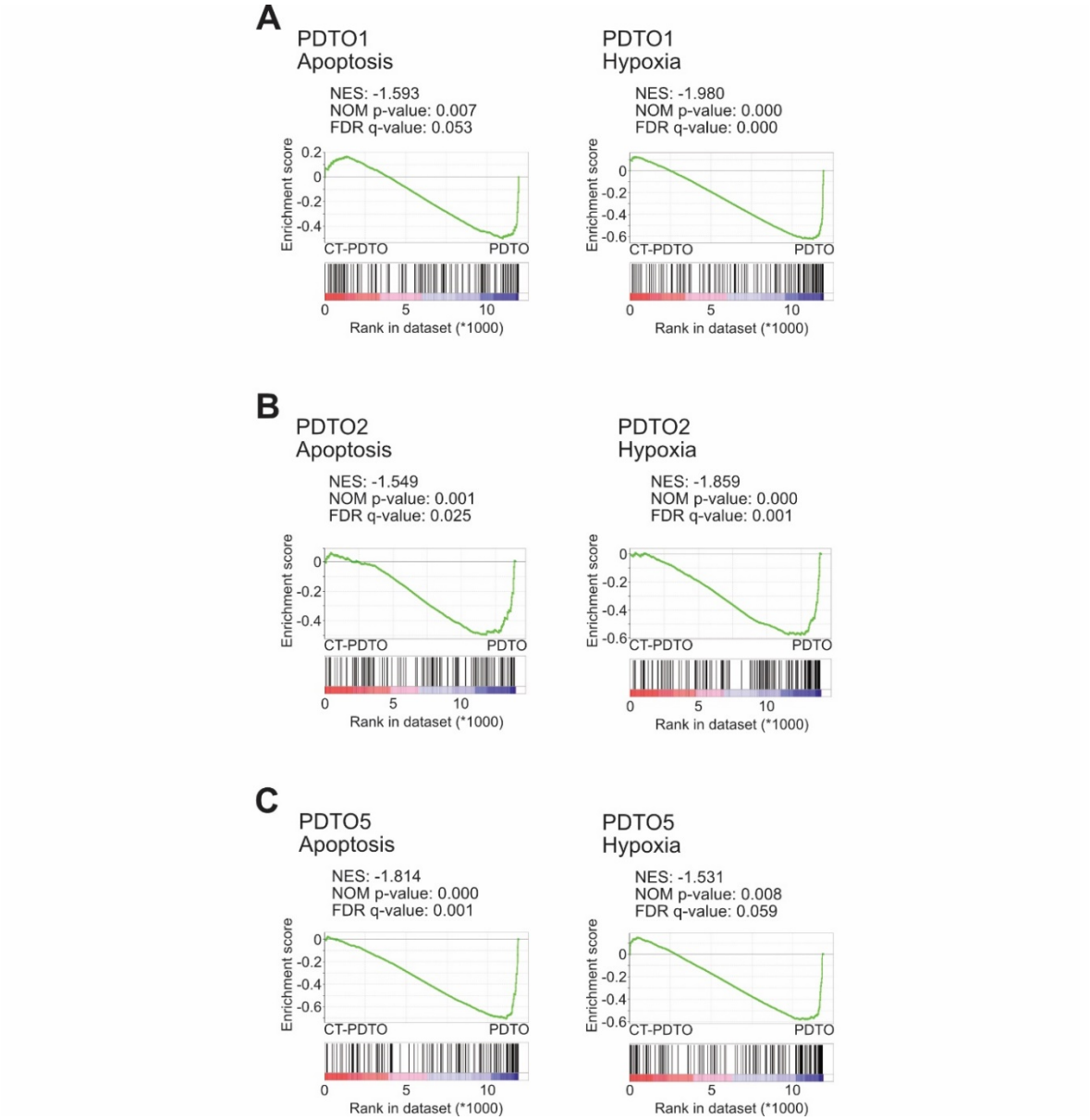

Figure 23: Gene set enrichment analysis plots of downregulated Hallmarks

Gene set enrichment analysis (GSEA) of FOLFIRI/Cmab treated CT-PDTOs versus untreated parental PDTOs with the Hallmark gene sets (MSigDB Collections, Broad Institute[190]). Shown are the gene sets that reached statistical significance at an FDR < 0.25 in all three CT-PDTOs compared to their parental counterparts. NES: normalized enrichment score, NOM p-value: nominal p-value, FDR q-value: false discovery rate. RNA sequencing was performed in collaboration with Dr. Rupert Öllinger, Thomas Engleitner, and Prof. Dr. Roland Rad.

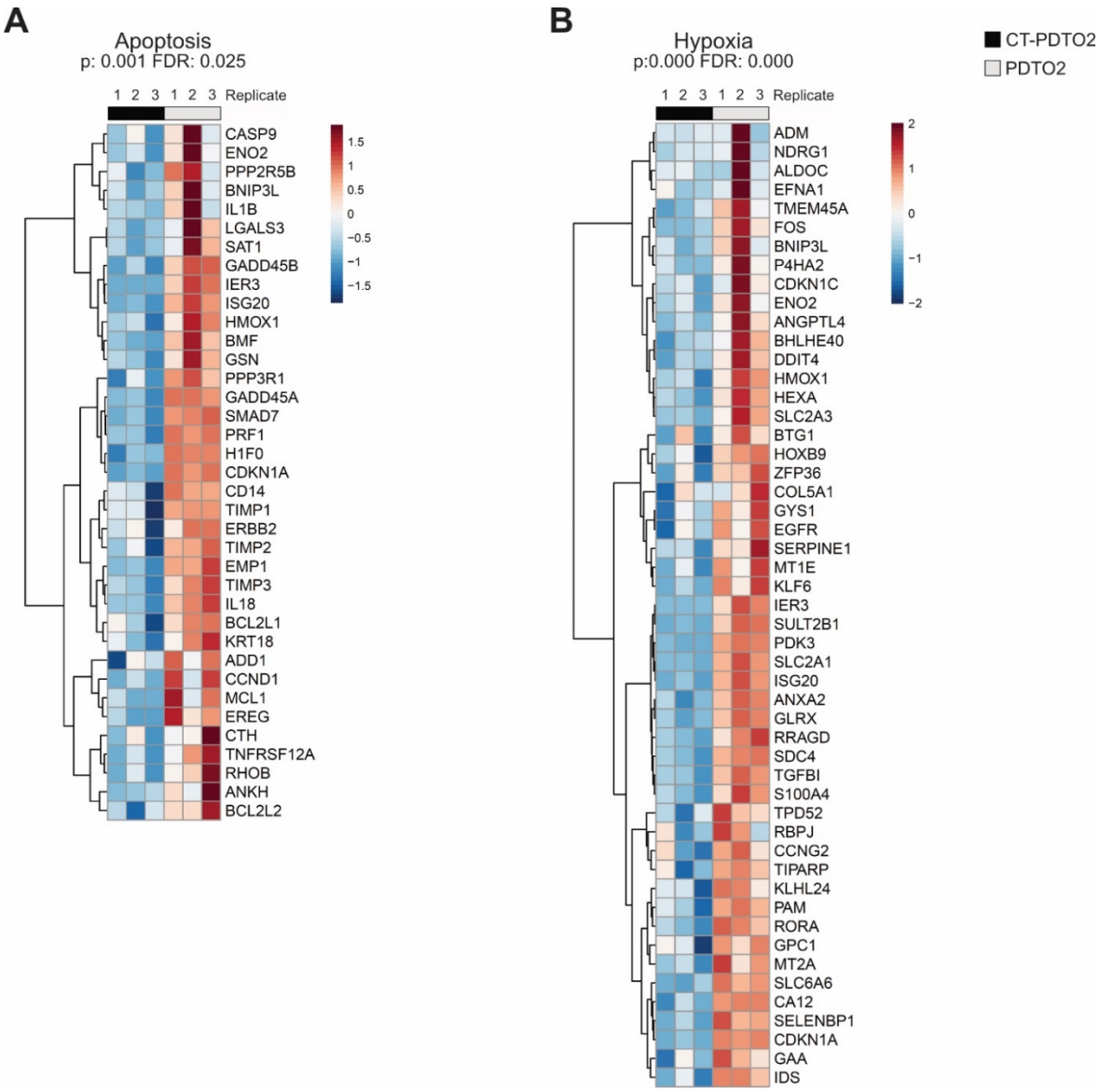

Figure 24: Heat maps of the leading edge genes of downregulated Hallmark gene sets "Apoptosis" and "Hypoxia" in CT-PDTO2 versus PDTO2

Shown are the heat maps of the leading edge subsets of the Hallmark gene sets "Apoptosis" and "Hypoxia" (MSigDB Collections, Broad Institute[190]) for CT-PDTO2 vs. PDTO2 of three replicates each. These gene sets were downregulated in all three CT-PDTOs compared to their parental PDTO counterparts. RNA sequencing was performed in collaboration with Dr. Rupert Öllinger, Thomas Engleitner, and Prof. Dr. Roland Rad.

5.5 Elevated MYC levels coincide with reduced sensitivity towards a dual EGFR/MEK inhibition

Misale *et al.* showed that prolonged EGFR inhibition results in the activation of downstream MAPK pathway components such as MEK and ERK, which leads to resistance towards this treatment[111]. Instead, they suggested a dual inhibition of EGFR and its downstream effector MEK as a more effective approach since it did not trigger resistance in their study[111]. To evaluate this so-called "vertical targeting" of the EGFR-MAPK signaling pathway in our setting of FOLFIRI/Cmab-tolerant organoid lines, we treated PDTOs and CT-PDTOs with the combination of Afatinib, a dual EGFR/HER2 inhibitor, and Selumetinib, a MEK inhibitor (here referred to as AfaSel). Indeed, this dual targeting of the EGFR signaling pathway led to a reduced viability in all six organoid lines (Figure 25). The CT-PDTO2 and 5 were less sensitive towards this dual inhibition than their parental counterparts, whereas both lines of the PDTO1 - parental and chemotherapy tolerant - showed similar levels of viability reduction upon treatment (Figure 25). Interestingly, as mentioned before, these CT-PDTO lines 2 and 5 also had other shared features: Both showed enriched G_2/M checkpoint, E2F targets, and MYC targets gene signatures (Table 6) as well as increased MYC protein levels (Figure 21). In contrast, CT-PDTO1, which had developed chemotherapy tolerance against FOLFIRI/Cmab independently of these Hallmark alterations, had not generated a tolerance towards the dual EGFR-MEK inhibition.

These data show that the treatment with a commonly applied first-line therapy such as FOLFIRI/Cmab can induce tolerance also against potential second-line therapeutic strategies, in this case a combined targeting of EGFR and MEK. This highlights the importance of experimentally evaluating the first-line therapy resistant tumors before the actual start of a second-line therapy. The potential correlation between the here observed enrichment in MYC target gene sets and the partially diminished response towards certain second-line therapy options could help to stratify patients into groups with different second-line treatment preferences or contraindications. However, this hypothesis warrants further confirmation in a larger cohort of pre-clinical models in the future.

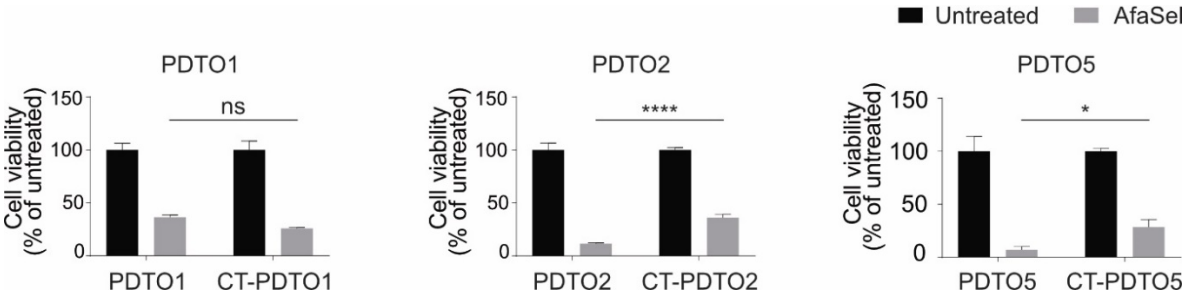

Figure 25: CT-PDTOs with increased MYC target gene expression show a decreased sensitivity towards vertical EGFR-MAPK pathway inhibition

Cell viability was determined after six days of treatment with AfaSel (50 nM of the pan-HER inhibitor Afatinib plus 50 nM of the MEK inhibitor Selumetinib) or corresponding concentrations of DMSO. Statistical significance between samples with the same treatment was assessed by a two-way ANOVA plus Sidak's multiple comparisons test and is indicated by asterisks (*: p-value ≤ 0.05, ****: p-value ≤ 0.0001, ns: p-value > 0.05). Mean + SD, n = 3.

5.6 AURKA inhibition induces apoptosis in *KRAS* wild type CT-PDTOs

Since a dual targeting strategy directed against the EGFR-MAPK pathway proved less effective in the two CT-PDTO lines with an acquired increase in E2F and MYC target gene expression, we set out to evaluate an adapted treatment option. A common approach is to target alternative growth and survival pathways that are activated due to resistance mechanisms to the first-line therapy[194,195]. In case of the CT-PDTOs that were less responsive to AfaSel treatment, two different sets of Hallmark MYC target gene sets were enriched. Since MYC is not an enzyme, it has no active site itself that could be targeted by a small molecule inhibitor. However, interactions of MYC with other proteins, such as its critical transcription co-factor MAX, can be targeted instead[44,115].

Intriguingly, Myc has been shown to form a complex with the G_2/M kinase Aurka in a hepatocellular carcinoma mouse model[133]. This complex stabilizes Myc and prevents it from proteasomal degradation. Conformation changing inhibitors of Aurka such as Alisertib can disrupt the generation of this complex, lead to the degradation of Myc, and subsequently reduce the cell viability in the liver cancer model published by Dauch *et al.*[133]

Another rationale for the treatment with an AURKA inhibitor is that in chromosomally instable CRC cells, the *AURKA* genomic locus is frequently amplified[135]. The resulting elevated AURKA expression levels are correlated with a poor prognosis[196–198]. The publicly available TCGA COAD and READ cohorts contain next generation RNA sequencing data from normal colorectal epithelium and CRCs. Analysis of these data sets showed that *AURKA* expression is increased in CRC cases compared to the normal tissue (Figure 26A),

which indicates an increased dependency of rapidly proliferating tumor cells on this G_2/M checkpoint component.

To assess whether this was recapitulated in our organoid model system, we compared the expression of *AURKA* in patient-derived organoids of normal mucosa (PDOs), both in a stem cell and a differentiated state, with the PDTOs used in our study by qRT-PCR. The PDOs of the normal colorectal epithelium showed a reduced *AURKA* expression under differentiation-inducing compared to the stemness-supporting culture conditions. Tumor-derived PDTOs displayed an even higher expression level of *AURKA* than the benign PDOs that were maintained in a proliferatively active and non-differentiated state (Figure 26B). PDTO1 had the highest and PDTO5 the lowest *AURKA* expression among the analyzed PDTOs. The FOLFIRI/Cmab treated CT-PDTOs showed a slightly reduced, but not statistically significant lower expression level of *AURKA* than their respective parental PDTOs (Figure 26B).

We performed immunohistochemical staining of AURKA on FFPE slides of a normal colonic mucosa and of the tumors, from which the PDTO1, 2, and 5 had been derived. In the normal mucosa sample, the expression of AURKA was restricted to the compartment of transit amplifying cells whereas the stem cell compartment at the bottom of the crypts and the differentiated upper region of the crypts were negative (Figure 26C). This agrees with the qRT-PCR data of the PDOs that showed a decrease in *AURKA* gene expression upon *in vitro* differentiation. Overall, the normal mucosa showed a weaker and less frequent AURKA staining compared to the CRC samples. In concordance with the *in vitro* mRNA levels, CRC5 was the tumor sample that showed the lowest protein expression of AURKA among the analyzed cancer tissues (Figure 26C).

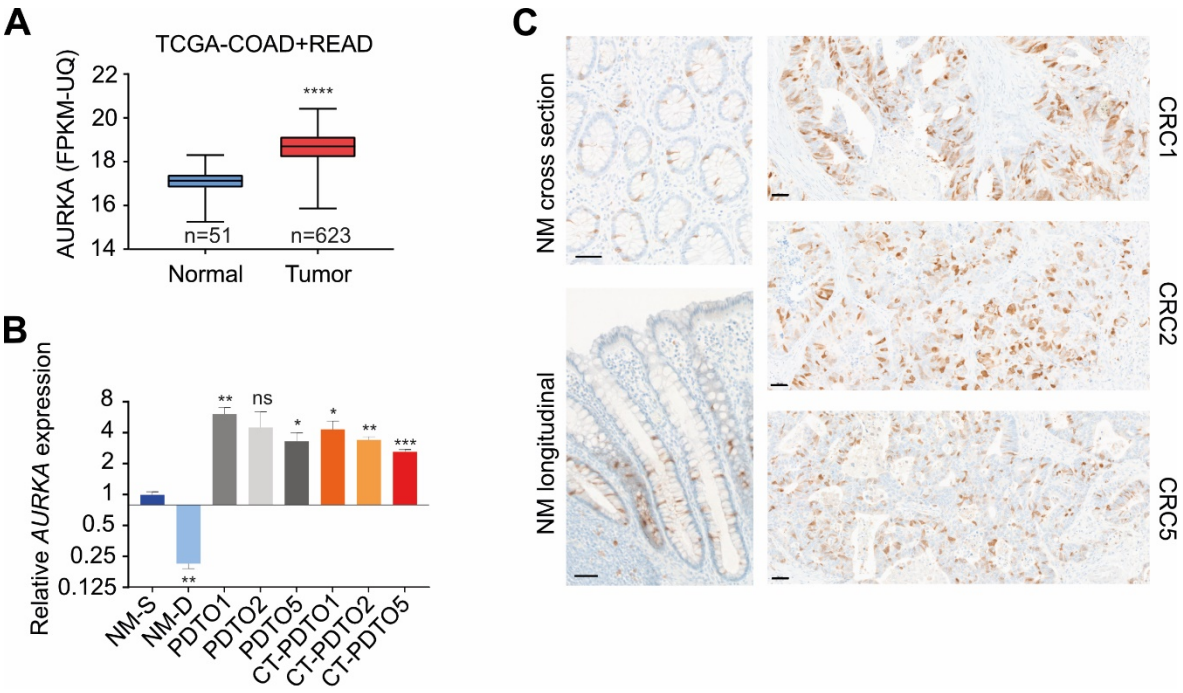

Figure 26: AURKA expression is increased in CRC and CRC-derived PDTOs

A) RNA sequencing data from TCGA-COAD and TCGA-READ cohorts were used for the comparison of *AURKA* expression levels in human normal mucosa (n = 51) and CRC tissues (n = 623). Box plots show the median and error bars indicate the minimal to maximal data spread. Statistical significance was assessed by an unpaired, two-tailed t-test and is indicated by asterisks (****: p-value ≤ 0.0001). **B)** The relative *AURKA* gene expression was determined by qRT-PCR in human benign organoids under stem cell (NM-S) or differentiation (NM-D) culture conditions (mean + SD of 2 different patients) and in PDTOs and CT-PDTOs (mean + SD, n ≥ 2 for each patient). Relative expression values were normalized to *PPIA* and *B2M* expression. Statistical significant difference of each sample to the NM-S samples was assessed by two-tailed t-tests and is indicated by asterisks (*: p-value ≤ 0.05, **: p-value ≤ 0.01, ***: p-value ≤ 0.001, ns: p-value > 0.05, here: p = 0.069). **C)** Immunohistochemical staining of AURKA in a normal colonic mucosa (NM) and the CRCs, from which the respective PDTO lines were generated. Scale bars indicate 50 µm. Staining was performed by the Diagnostic Department of the Institute of Pathology (LMU Munich).

The high expression of AURKA in the CRC1, 2, 5, and the respective PDTOs could stem from a common amplification of chromosome 20q13.2, which harbors the *AURKA* gene. To test this hypothesis, we performed next generation whole exome sequencing of the parental PDTO1, 2, and 5 in collaboration with Dr. Greif and Dr. Vosberg (LMU Munich). The copy number alteration (CNA) plots are depicted in Figure 27. The tumor samples were normalized to two normal mucosa samples from different patients, which were not expected and not found to contain any major chromosomal aberrations (Figure 27D). Indeed, chromosome 20q13.2 was amplified in all three PDTO samples. The highest amplification of 2.26-fold was seen in PDTO2. PDTO5 displayed a lower amplification, yet a 1.59-fold increase of *AURKA* copy numbers was determined. Overall, the analyses show a correlation between genomic DNA, mRNA, and protein levels of AURKA and suggest that PDTO5 has the lowest AURKA levels compared to PDTO1 and PDTO2.

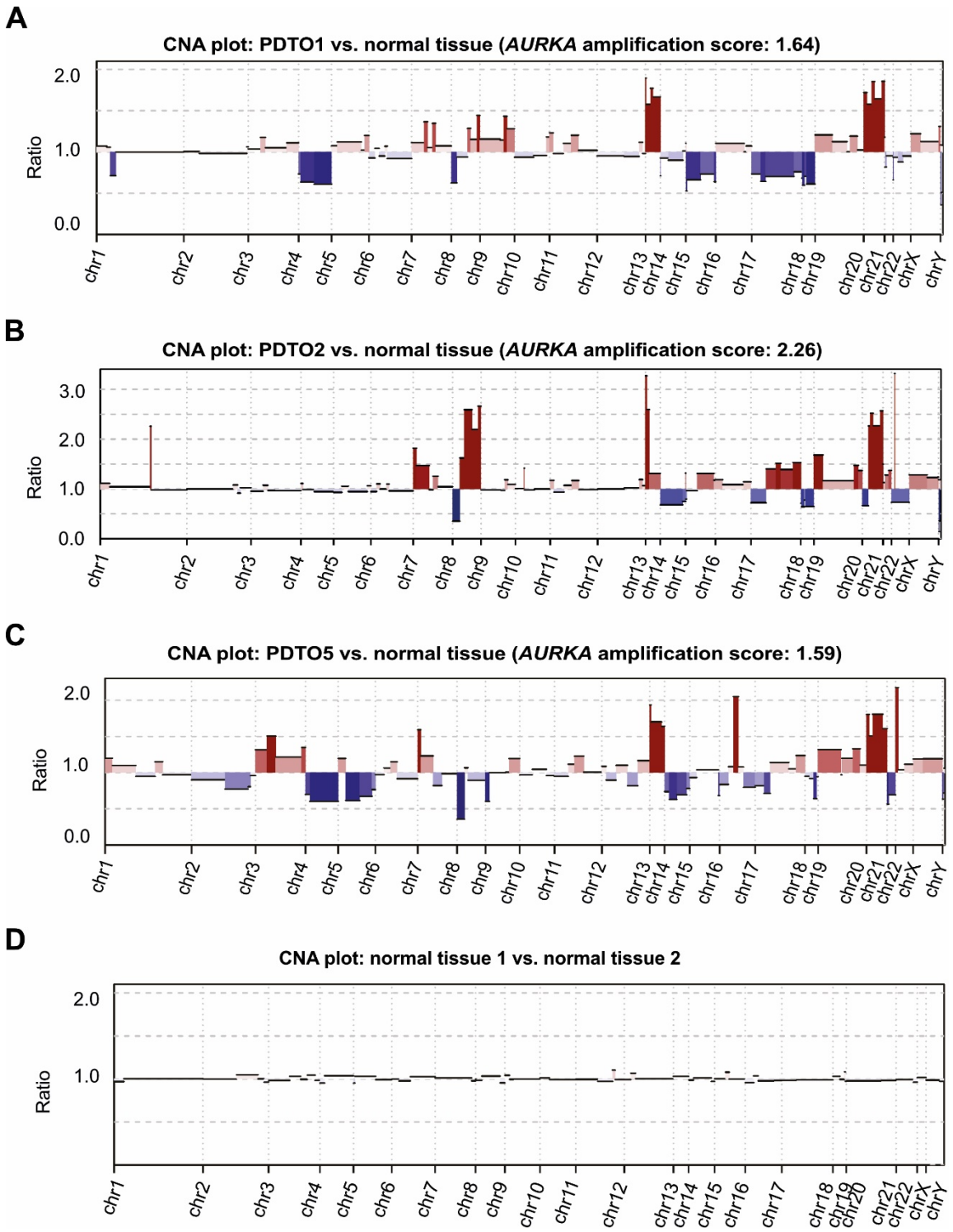

Figure 27: Copy number alteration plots of PDTO1, 2, and 5

Copy number alteration (CNA) plots were generated from whole exome sequencing. **A – C)** Next generation whole exome sequencing data from PDTO1, 2, and 5 were normalized to that of benign tissue. Note the pronounced genomic amplification of chromosome 20, which contains the *AURKA* gene. **D)** CNA plot of normal tissue from two different patients. These were used as a reference for the analyses of PDTO1, 2, and 5. Note that no major chromosomal alterations were detected, which indicates an unaltered 2N DNA content. Whole exome sequencing data analysis was performed by Dr. Vosberg and Dr. Greif (both LMU Munich).

We hypothesized that the high expression of AURKA in the tumor samples could be exploited therapeutically to overcome the acquired FOLFIRI/Cmab tolerance in our CT-PDTOs. We evaluated this by targeting AURKA with the small molecule inhibitor Alisertib. This inhibitor is currently tested in clinical trials and seems to be tolerated well in patients. It has also been described to change the conformation of AURKA and thereby prevent its interaction with MYC[133,156–160].

Therefore, we treated the CT-PDTOs with Alisertib. Indeed, this treatment was able to reduce the viability of all three CT-PDTO lines (Figure 28). Notably, the cell viability was reduced the furthest in CT-PDTO2, which displayed high *AURKA* expression and whose parental counterpart showed the highest amplification of chromosome 20q13.2 (Figure 26B, Figure 27B). CT-PDTO5 responded to a lesser extent to the AURKA inhibitor Alisertib (Figure 28). This CT-PDTO line showed also relatively lower *AURKA* mRNA expression and its parental PDTO line had a lower magnitude of chromosome 20 amplification as well as mRNA and protein levels of AURKA (Figure 26B, Figure 27C). These data suggest a positive correlation between the overall AURKA expression with the response to Alisertib. Nonetheless, a larger-scale study is necessary to confirm this preliminary finding in a higher number of CRC models.

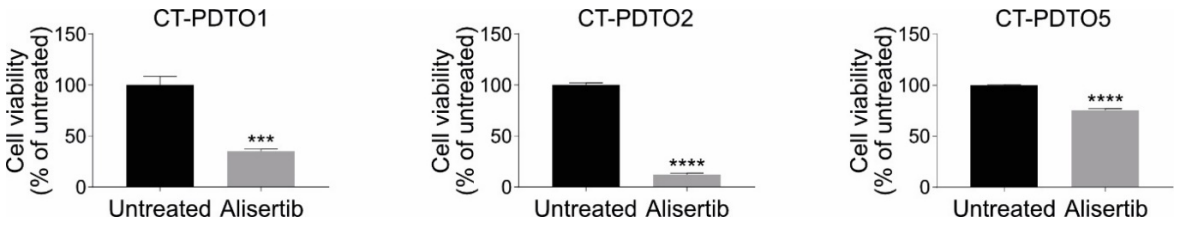

Figure 28: Alisertib treatment reduces the cell viability of CT-PDTOs

For cell viability analysis, the CT-PDTOs were treated with 100 nM of the AURKA inhibitor Alisertib or the according concentration of DMSO for 6 days. Statistical significance was assessed by a t-test and is indicated in by asterisks (***: p-value ≤ 0.001, ****: p-value ≤ 0.0001). Mean + SD, n = 3.

Since not only the general ability of a potential therapy approach to decrease the cell viability but also to induce apoptosis represents a key aspect, we evaluated whether Alisertib was able to induce apoptosis in the FOLFIRI/Cmab-adapted CT-PDTOs. Indeed, when we performed immunoblot analysis for cleaved PARP and cleaved caspase 3 - both well accepted indicators of apoptosis - we detected that treatment with FOLFIRI/Alisertib was able to induce apoptosis in all three CT-PDTO lines (Figure 29). As seen before and reanalyzed here in

parallel to the Alisertib-containing drug regimen, no or only marginal levels of apoptosis were induced by FOLFIRI/Cmab in drug-adapted tumor organoids (Figure 14, Figure 29). These data suggest that liver metastatic CRCs with high AURKA levels, which have developed a resistance to the first-line therapy FOLFIRI/Cmab independent of resistance-conferring mutations, are susceptible to treatment with AURKA inhibitors.

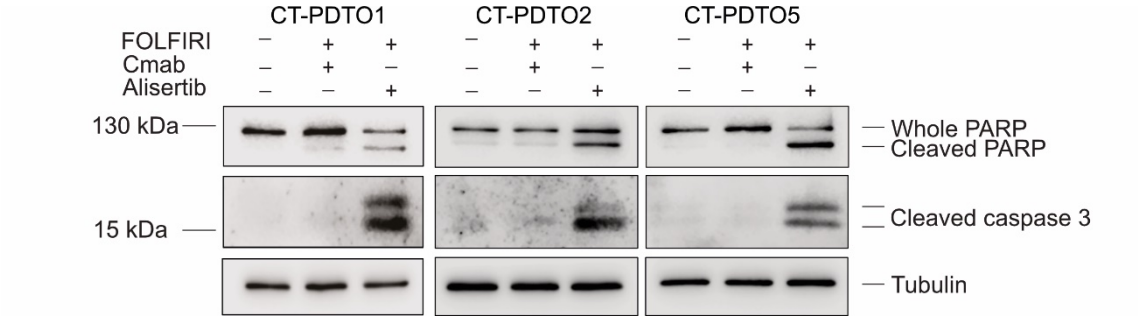

Figure 29: The AURKA inhibitor Alisertib induces apoptosis in CT-PDTOs

Established organoids of the chemotherapy-adapted CT-PDTOs were treated with the indicated treatments for 48 h before harvest for immunoblot analysis. Alisertib: AURKA inhibitor (400 nM). Immunoblot analysis of these samples was performed against whole and cleaved PARP as well as cleaved caspase 3. Cleavage of PARP and caspase 3 represent markers for apoptosis. Alpha-tubulin was used as a loading control.

5.7 Introduction of a KRAS^{G12D} mutation into CT-PDTOs via CRISPR/Cas9-mediated genome engineering

One of the best-known mechanisms that can lead to the development of therapy resistance against EGFR-MAPK pathway inhibition is the gain of an activating *KRAS* mutation, such as KRAS^{G12D}. The KRAS protein, once aberrantly activated, independently signals downstream of EGFR and therefore can render tumor cells irresponsive to EGFR-inhibiting agents such as Cmab[95,96]. *KRAS* mutations can arise in drug persister cells under the prolonged pressure of treatment and thereby lead to the development of therapy resistances[104].

To model the situation where the prolonged first-line therapy exposure led to the generation of a *KRAS* mutation in drug persister cells, we introduced a KRAS^{G12D}-encoding mutation into the CT-PDTOs by CRISPR/Cas9-mediated genetic engineering. We utilized DNA-free ribonucleoproteins that are composed of a *KRAS*-targeting guide RNA and the Cas9 protein in combination with an oligonucleotide coding for the KRAS^{G12D} mutation with flanking homology arms on both sides (Figure 30). The homology-directed repair machinery of the

cell uses the mutated oligonucleotide as a template to repair the DNA double strand break created by the CRISPR/Cas9 ribonucleoprotein. Thereby, the $KRAS^{G12D}$ mutation is introduced into the genome. In addition, the oligonucleotide contains two silent mutations, which are introduced into the genome alongside the $KRAS^{G12D}$ mutation, to distinguish cells with a genetically engineered *KRAS* mutation from those with a sporadic mutation.

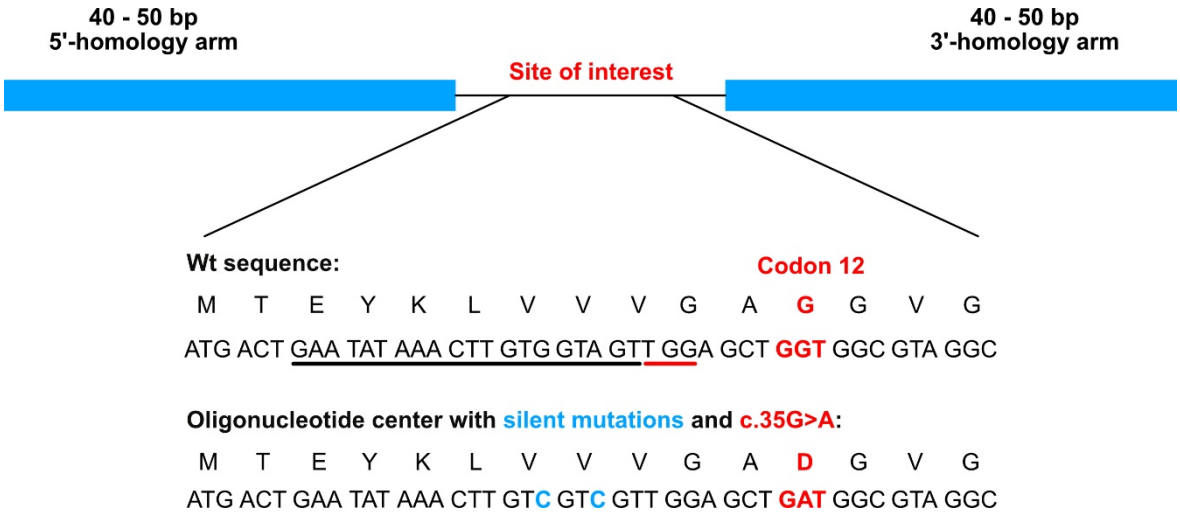

Figure 30: Schematic of the mutated *KRAS* oligonucleotide for genetic engineering

Representation of the oligonucleotide that was used for CRISPR/Cas9-mediated genetic engineering of *KRAS*. It contains the c.35G>A mutation in codon 12 resulting in $KRAS^{G12D}$ (both highlighted in red) and two silent mutations (blue) to discriminate between cells with the engineered mutation and cells with spontaneously arisen mutations. Underlined in black is the 20-mer single guide RNA target sequence, the protospacer adjacent motif (PAM) is underlined in red. Wt: wild type, bp: base pairs.

After a selection for successfully KRAS^{G12D}-engineered CT-PDTO cells with Cmab, to which the cells with activated KRAS should be less responsive, the Diagnostics Department of the Institute of Pathology (LMU Munich) performed routine pyrosequencing of the KRAS^{G12D} locus on exon 2 of the *KRAS* gene. Figure 31A shows a representative sequencing result of the parental PDTO2 and the PDTO2 harbouring the genetically engineered KRAS^{G12D} mutation (eKRAS). Notably, the locus of interest is indicated with a red frame: The GGT>GAT mutation, encoding for KRAS^{G12D}, was determined in the PDTO2 eKRAS but not the wild type sequence of the parental PDTO2.

To estimate the allele frequency of the engineered mutation, we performed panel sequencing using the Cancer Hot Spot v2 Panel in collaboration with the Diagnostics Department of the Institute of Pathology of the LMU Munich, coordinated by Dr. Jörg Kumbrink. It confirmed the successful engineering of the KRAS^{G12D} mutation in PDTO1 eKRAS with a sequencing depth of approximately 1986-fold coverage. The eKRAS allele frequency was determined to be 54 %, which suggests a successful heterozygous mutation of *KRAS* in the targeted CT-PDTOs (Figure 31B).

Moreover, we set out to confirm that not only the *KRAS* G12D codon, but also the surrounding genomic region, which is covered by the repair oligonucleotide, remained intact. To achieve this, we PCR-amplified a 645 bp part of the engineered *KRAS* locus. Sanger sequencing confirmed the intact DNA sequence flanking the oligonucleotide used for homologous recombination and of the homology arms. As expected, the only bases differing from the *KRAS* reference sequence were the GGT>GAT mutation encoding for KRAS^{G12D} and the two silent mutations we added for discrimination from spontaneously occurring mutations (Figure 31C). In summary, we genetically engineered a KRAS^{G12D} mutation into the endogenous *KRAS* locus of the three CT-PDTO lines.

A

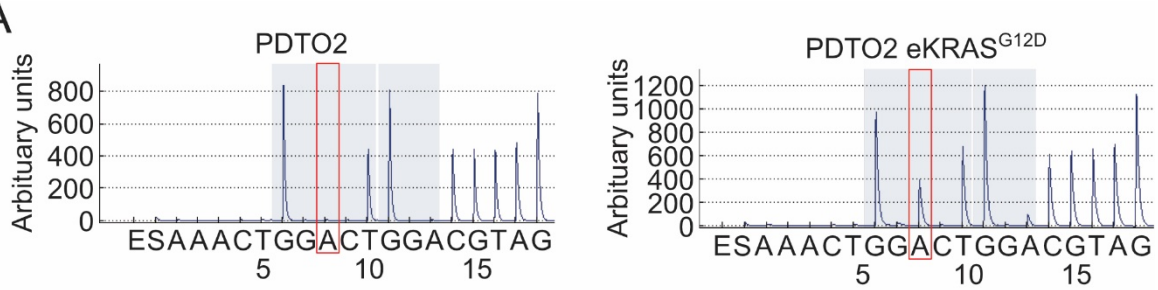

B

Tumor line	Chrom. Pos	Gene	cDNA	Protein	Coverage	Allele frequency
PDTO1 eKRAS^{G12D}	chr12:25398280	*KRAS*	c.35G>A	p.G12D	1986	0.5408

C

Figure 31: Genome engineering of oncogenic *KRAS* in PDTOs

A) Pyrosequencing confirmed the successful introduction of the KRAS^{G12D}-encoding mutation. Red frames indicate the c.35, the site of potential mutation: note the appearance of a peak at the position of the A (GGT > GAT) in the edited PDTO2 eKRAS (right panel). **B)** Panel sequencing of PDTO1 eKRAS determined the allele frequency of 54.08 % of the KRAS^{G12D}-encoding variant at a coverage of 1986. **C)** Sanger sequencing confirmed not only the successful mutation of codon 12 (GGT > GAT, red) and the silent mutations (grey) but also the intact sequence of the whole oligonucleotide (blue) and the adjacent sequence. A, B) Pyrosequencing and panel sequencing were performed by the Diagnostics Department of the Institute of Pathology under the supervision of Dr. Jörg Kumbrink (LMU Munich).

After we showed the genetic intactness of the introduced $KRAS^{G12D}$ mutation, we next set out to test its oncogenic activity. We analyzed this relevant aspect by treating the CT-PDTO and the CT-PDTO eKRAS lines with Cmab in parallel. As expected, the mutated KRAS protein conferred a reduced sensitivity towards this treatment even in the tumor organoids that were pre-adapted to FOLFIRI/Cmab treatment for several months (Figure 32A). This confirms the biological integrity of the mutated KRAS protein.

Several studies have assessed whether *KRAS* mutant CRC models can be targeted with a combination of EGFR and MEK inhibitors. Misale *et al.* showed that in CRC cell lines that had gained mutations in *KRAS*, *NRAS*, or *BRAF* upon acquisition of Cmab resistance, the combined targeting of EGFR and MEK reduced cell growth *in vitro* and regressed patient-derived xenograft tumors *in vivo*[111]. However, Verissimo *et al.* demonstrated that a double blockade of the EGFR-MAPK signaling pathway reduced the viability of $KRAS^{G12D}$ mutant CRC PDTOs to a lesser extent when compared to *KRAS* wild type PDTOs[112]. Since the $KRAS^{G12D}$ mutation conferred a partial resistance towards this dual inhibition of the EGFR-MAPK pathway, higher drug concentrations were required to achieve the desired effect on cell viability[112].

To elucidate this issue further, we treated the KRAS wild type and the $KRAS^{G12D}$ mutated CT-PDTOs with AfaSel, the combination of the EGFR/HER inhibitor Afatinib and the MEK inhibitor Selumetinib (Figure 32B). The CT-PDTO eKRAS lines displayed a reduced sensitivity to AfaSel when compared to their KRAS wild type counter parts, which confirms the observations made by Verissimo *et al*[112]. Notably, the response towards this dual EGFR-MAPK pathway inhibition varied between the organoid lines derived from different CRC patients, which underlines the argument to integrate the PDTO model in personalized medicine. Simultaneously, this experiment also confirmed the biological activity of the genetically engineered and endogenously expressed $KRAS^{G12D}$.

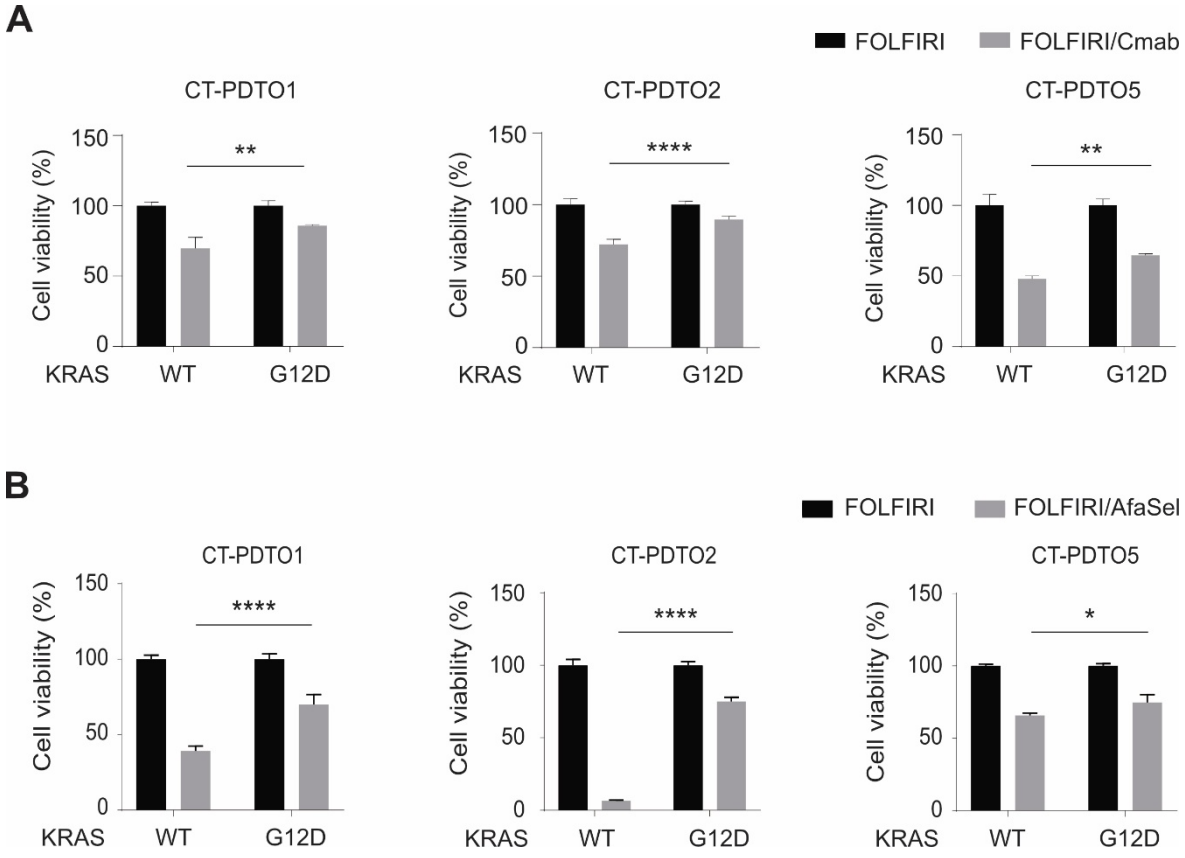

Figure 32: CT-PDTO eKRAS are less sensitive to Cmab and AfaSel

Cells were treated as indicated for 7 (CT-PDTO1 and 5) or 6 (CT-PDTO2) days before cell viability assessment. **B)** AfaSel concentrations were 20 nM (CT-PDTO1 and 5) or 100 nM (CT-PDTO2). **A, B)** Mean + SD, n = 3. Statistically significant differences between samples with the same treatment were assessed by a two-way ANOVA with a Sidak's multiple comparisons test and are indicated by asterisks (*: p-value ≤ 0.05, **: p-value ≤ 0.01, ****: p-value ≤ 0.0001).

Moreover, Verissimo *et al.* stated that while KRAS wild type cells respond to AfaSel with apoptosis, $KRAS^{G12D}$ mutated cells do not, which would implicate an only transient, reversible effect of AfaSel on *KRAS* mutant CRC[112]. To confirm this, we treated PDTO1 and PDTO1 eKRAS lines with the same high concentrations of AfaSel (1 µM for 48 hours) as Verissimo *et al.* employed in their study and assessed the levels of apoptosis using immunoblot analysis of cleaved PARP and cleaved caspase 3. Indeed, the *KRAS* wild type PDTO1 showed high levels of PARP and caspase 3 cleavage upon AfaSel treatment, while the $KRAS^{G12D}$ counterpart did not display any effect on these apoptotic markers (Figure 33). In summary, we confirmed in our PDTO model that the introduction of a $KRAS^{G12D}$ mutation reduces the sensitivity towards the vertical EGFR-MAPK pathway inhibition, as demonstrated by cell viability and apoptosis measurements.

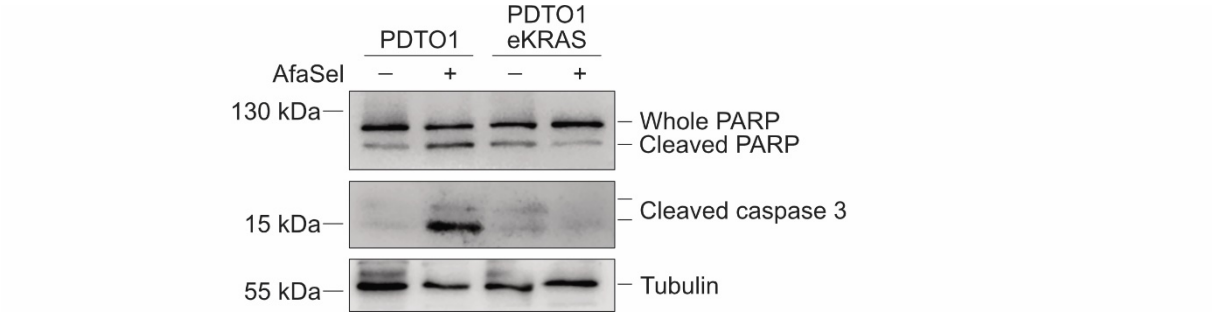

Figure 33: PDTO1 but not PDTO1 eKRAS responds with apoptosis to AfaSel treatment

Established organoids of the parental PDTO1 and the CRISPR/Cas9-genetically engineered $KRAS^{G12D}$ (eKRAS) PDTO1 were treated with 1 µM each of the EGFR/HER inhibitor Afatinib and the MEK inhibitor Selumetinib (AfaSel) for 48 h. Immunoblot analyses were performed against whole and cleaved PARP as well as cleaved caspase 3. Cleavage of PARP and caspase 3 are markers for apoptosis. Alpha-tubulin was used as a loading control.

5.8 Dual EGFR-MAPK pathway inhibition primes *KRAS* mutant PDTOs for apoptosis by the AURKA inhibitor Alisertib

As mentioned above, Verissimo *et al.* demonstrated that $KRAS^{G12D}$ CRC PDTOs are more resistant towards a dual EGFR-MAPK pathway inhibition than *KRAS* wild type PDTOs[112]. Interestingly, they showed that addition of other targeted drugs can act synergistically and that the combination can reduce the cell viability more than either drug alone[112].

We hypothesized that the combination of AfaSel with Alisertib would induce a superior response concerning the cell viability in *KRAS* mutant PDTOs than AfaSel or Alisertib alone. To test this hypothesis, we treated the CT-PDTO eKRAS lines with AfaSel, Alisertib, or the combination of these drugs (Figure 34A, C). In all three lines, the cell viability was significantly reduced further by AfaSel/Alisertib compared to the single treatments. The CT-PDTO2 eKRAS was especially responsive towards the combination of AfaSel/Alisertib and the cell viability was reduced to 2 % (Figure 34A, C).

To confirm the collaborative effect of AfaSel/Alisertib not only in our organoid lines with engineered $KRAS^{G12D}$ but also in tumor cells with spontaneously occurring *KRAS* mutations, we applied this treatment to additional models with sporadic KRAS mutations: PDTO4 contains a $KRAS^{G12D}$ mutation, PDTO17 a $KRAS^{G12R}$ mutation, and the classical CRC cell line SW620 expresses the oncogenic $KRAS^{G12V}$ variant. As seen in the CT-PDTO eKRAS lines, treatment with either AfaSel or Alisertib alone was inferior to the combination of both therapies (Figure 34B).

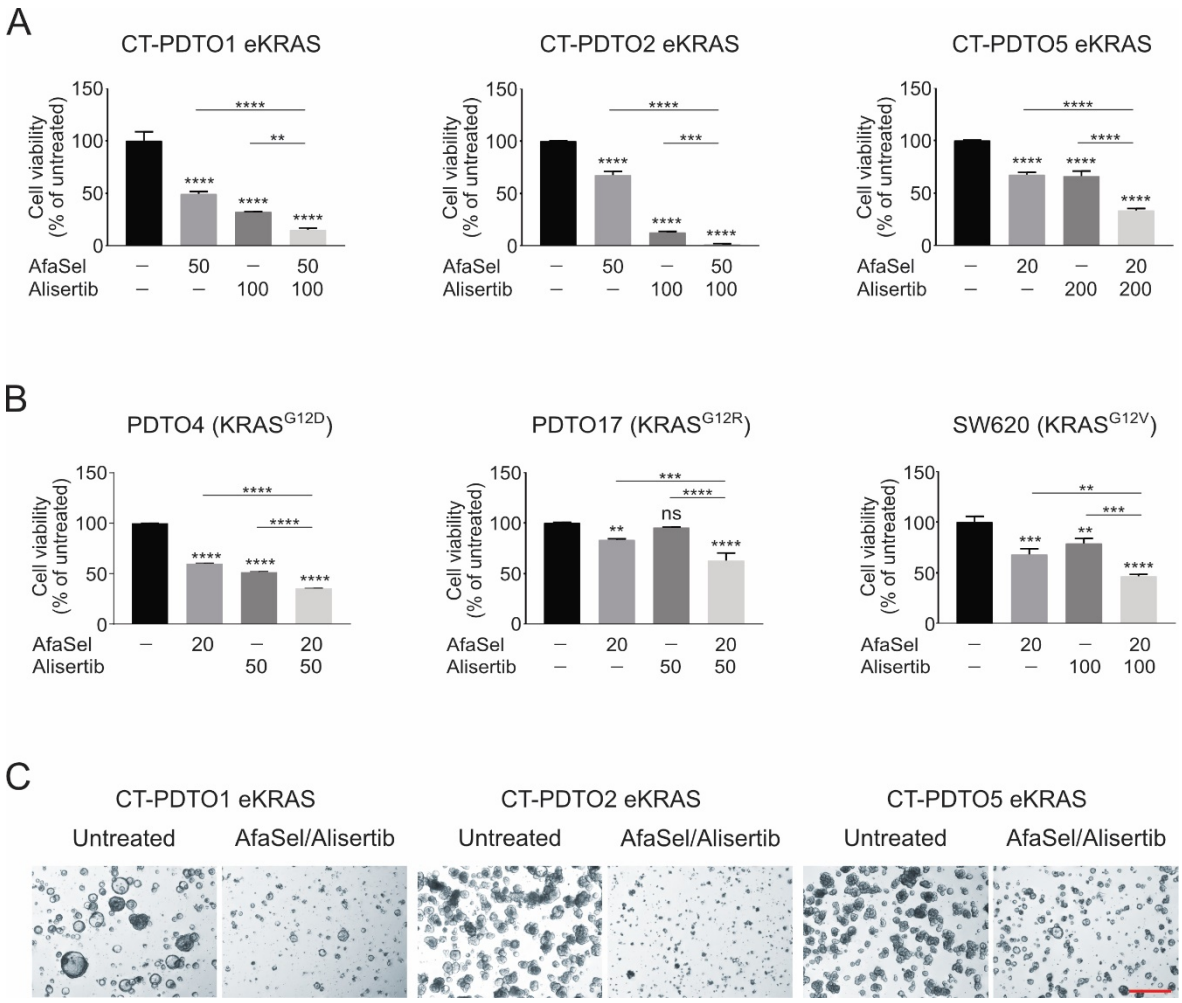

Figure 34: AfaSel/Alisertib treatment reduces the cell viability of *KRAS* mutants stronger than single treatments

A) Cell viability was analyzed after 6 days of treatment. **B)** Cell viability was assessed after 5 (PDTO4), 7 (PDTO17) or 3 days (SW620) of treatment. **A, B)** Drug doses of AfaSel (pan-HER inhibitor Afatinib plus MEK inhibitor Selumetinib) and Alisertib (AURKA inhibitor) are given in nanomolar concentrations below the bars. Statistical significance was assessed by a one-way ANOVA plus Tukey's multiple comparisons test and is indicated by asterisks (**: p-value ≤ 0.01, ***: p-value ≤ 0.001, ****: p-value ≤ 0.0001, ns: p-value > 0.05). Mean + SD, n = 3. **C)** Microscopic pictures of CT-PDTOs eKRAS with the indicated treatments from panel A after 6 days of treatment. Scale bar in the right picture indicates 500 µm and is representative for all images.

The cell proliferation of classical two-dimensionally grown cell lines can be constantly monitored over the period of several days using the xCELLigence real-time cell analyzer (RTCA) system. We used this method to assess the effect of AfaSel, Alisertib, or their combination in SW620 cells. Figure 35 shows the cell index, which is representative of the number of attached cells during a course of 130 hours. As expected from the cell viability measurements with CellTiter-Glo®, the treatment with AfaSel/Alisertib was significantly superior to the monotherapeutic approaches.

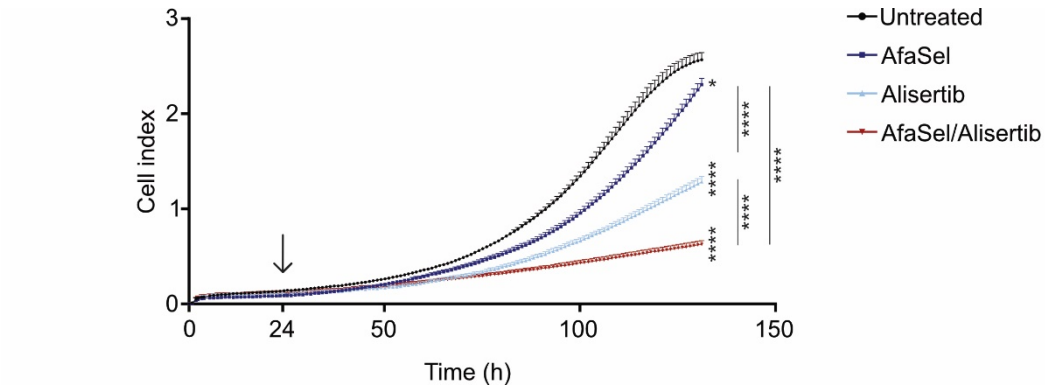

Figure 35: AfaSel/Alisertib treatment reduces SW620 cell numbers

SW620 cells were treated with 20 nM of AfaSel (pan-HER inhibitor Afatinib plus MEK inhibitor Selumetinib) and 100 nM of Alisertib (AURKA inhibitor) 24 h after seeding (indicated by the arrow). The cell index is representative of the number of attached cells. Mean + SD, n = 4. Statistical significance was assessed by a one-way ANOVA at the last measured time point (130 h) and is indicated by asterisks (*: p-value ≤ 0.05, ****: p-value ≤ 0.0001).

It has been published that a vertical EGFR-MAPK pathway inhibition alone does not evoke an apoptotic response in $KRAS^{G12D}$ tumors but might still prime the cells for apoptosis when combined with other treatments[112]. This means that a cytostatic EGFR-MAPK pathway inhibition concomitantly lowers the threshold for apoptosis induced by other therapeutic agents, which act on alternative cancer-relevant signaling pathway components[112].

Therefore, we assessed whether AfaSel treatment could prime the *KRAS* mutant PDTOs and thereby lower the apoptotic threshold for treatment with Alisertib. We achieved this by analyzing the occurrence of apoptotic markers in treated organoids and SW620 cells by immunoblot analysis (Figure 36). FOLFIRI/AfaSel failed to induce a noteworthy level apoptosis in the *KRAS* mutant models compared to the treatment with FOLFIRI alone as shown before (Verissimo *et al.*[112] and Figure 33). The different lines responded to a different extent to FOLFIRI/Alisertib: Whereas two lines (CT-PDTO1 and SW620) responded with

almost no induction of apoptotic markers compared to the treatment with FOLFIRI alone, there was a weak indication of apoptotic marker increase in four PDTO lines (CT-PDTO2 eKRAS, CT-PDTO5 eKRAS, PDTO4, and PDTO17). The combination of FOLFIRI/AfaSel/Alisertib was superior to monotherapies: It augmented the apoptotic rate in cell or organoid lines as shown by an increase in the apoptotic markers cleaved PARP and cleaved caspase 3 in five out of six *KRAS* mutant CRC models. CT-PDTO1 eKRAS was a notable exception as there was only a weak apoptotic response upon any of the treatments. Notably, the CT-PDTO1 had also developed the tolerance towards FOLFIRI/Cmab via a different mechanism than the other two CT-PDTO lines. As mentioned above, CT-PDTO1 displayed an enrichment in interferon alpha-related gene expression rather than increased G_2/M checkpoint, E2F targets, and MYC targets Hallmark gene signatures (Table 6).

In summary, five out of six CRC models showed a benefit of the combination of FOLFIRI/AfaSel/Alisertib.

Next, we assessed whether the treatment with AfaSel, Alisertib, or their combination affected the levels of MYC (Figure 36). We analyzed this aspect by immunoblot analysis of treated CT-PDTO eKRAS lines. Indeed, the MYC protein levels were most effectively decreased by combinatorial FOLFIRI/AfaSel/Alisertib treatment. Notably, we observed a milder decrease in MYC protein also by single agent treatments, although this effect was dependent on the analyzed PDTO model and was therefore patient-specific.

In conclusion, these data suggest that the dual EGFR-MAPK pathway inhibition with AfaSel primes *KRAS* mutant cells for apoptosis upon treatment with the AURKA inhibitor Alisertib. However, this seems to be dependent on the characteristics of the tumor, potentially on its path of developing a tolerance towards first-line therapy.

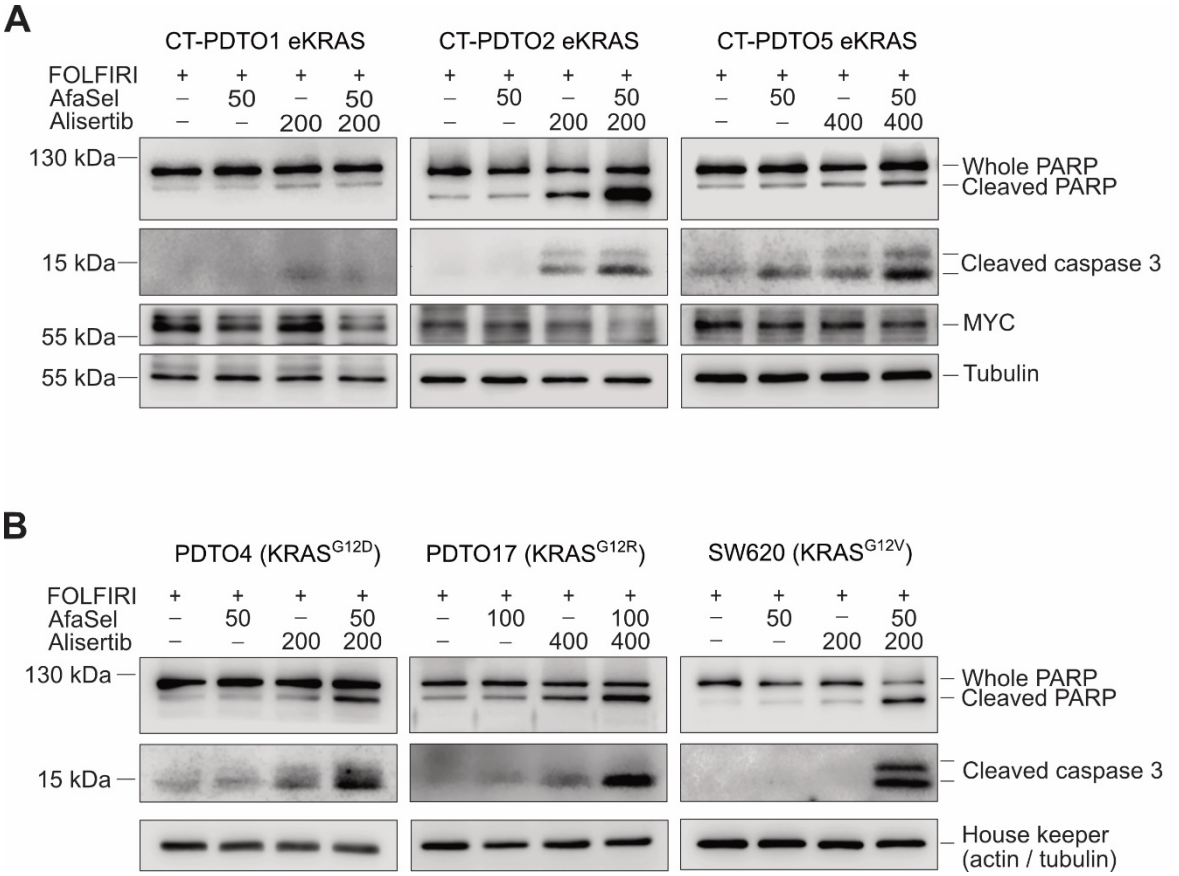

Figure 36: FOLFIRI/AfaSel/Alisertib induces apoptosis in *KRAS* mutant PDTOs

Immunoblot analysis of the indicated apoptosis markers (cleaved PARP and cleaved caspase 3) and MYC in CT-PDTOs carrying CRISPR/Cas9-engineered $KRAS^{G12D}$ (eKRAS) and in PDTOs and SW620 cells with the indicated KRAS variants. Cells were treated for 48 h with the indicated drug combinations (FOLFIRI, AfaSel (pan-HER inhibitor Afatinib plus MEK inhibitor Selumetinib), Alisertib (AURKA inhibitor)). Drug doses are given in nanomolar concentrations. A) Alpha-tubulin was used as a loading control. B) Beta-actin (PDTO17) or alpha-tubulin (PDTO4 and SW620) were used as a loading control.

Since we detected a growth inhibitory effect of AfaSel alone on the *KRAS* mutant (CT-) PDTOs (Figure 34), but no induction of apoptosis upon 48 hours of treatment with this regimen (Figure 36), we aimed to determine whether prolonged treatment with FOLFIRI/AfaSel would lead to a reduced recovery of organoids. We analyzed this by treating CT-PDTO1 eKRAS with FOLFIRI or FOLFIRI/AfaSel for six days and subsequently leaving the cells to recover in the absence of the drugs. The cell viability was assessed after 6 days of treatment as well as 11 days after treatment stop, when recovery and outgrowth of unharmed organoids was expected to have taken place (Figure 37A).

In accordance with the 48-hour treatment of AfaSel alone, which failed to induce apoptotic markers in CT-PDTO1 eKRAS (Figure 36A), even a 6 day exposure did not prevent a recovery of tumor organoids (Figure 37B). This confirms a purely cytostatic and only transient as well as reversible action of AfaSel on CRC growth, and is in accordance with what has been observed by others[112].

Based on these data, we aimed to test whether the AfaSel/Alisertib treatment could achieve a reduced recovery of treated PDTOs. Therefore, we repeated the recovery experiment with FOLFIRI or FOLFIRI/AfaSel/Alisertib treatment in the CT-PDTO2 eKRAS and CT-PDTO1 eKRAS lines – representative of organoid lines that did and did not show an increase in apoptosis levels after 48 hours of treatment, respectively.

After 6 days of treatment, the cell viability of $KRAS^{G12D}$-engineered organoids was drastically reduced by FOLFIRI/AfaSel/Alisertib to 7.6 % and 6.2 % in CT-PDTO1 eKRAS and CT-PDTO2 eKRAS, respectively (Figure 37C). We then removed the therapeutic agents to induce organoid recovery. While some CT-PDTO1 eKRAS organoids were able to recover from the treatment, the cell viability of CT-PDTO2 eKRAS remained constant (18.4 % and 6.2 % viability compared to untreated PDTOs at day 6, respectively). This is in agreement with our results from the immunoblot analysis (Figure 36A), which indicated that CT-PDTO2 eKRAS but not CT-PDTO1 eKRAS responded with substantial apoptosis to the short-term 48-hour treatment period with FOLFIRI/AfaSel/Alisertib.

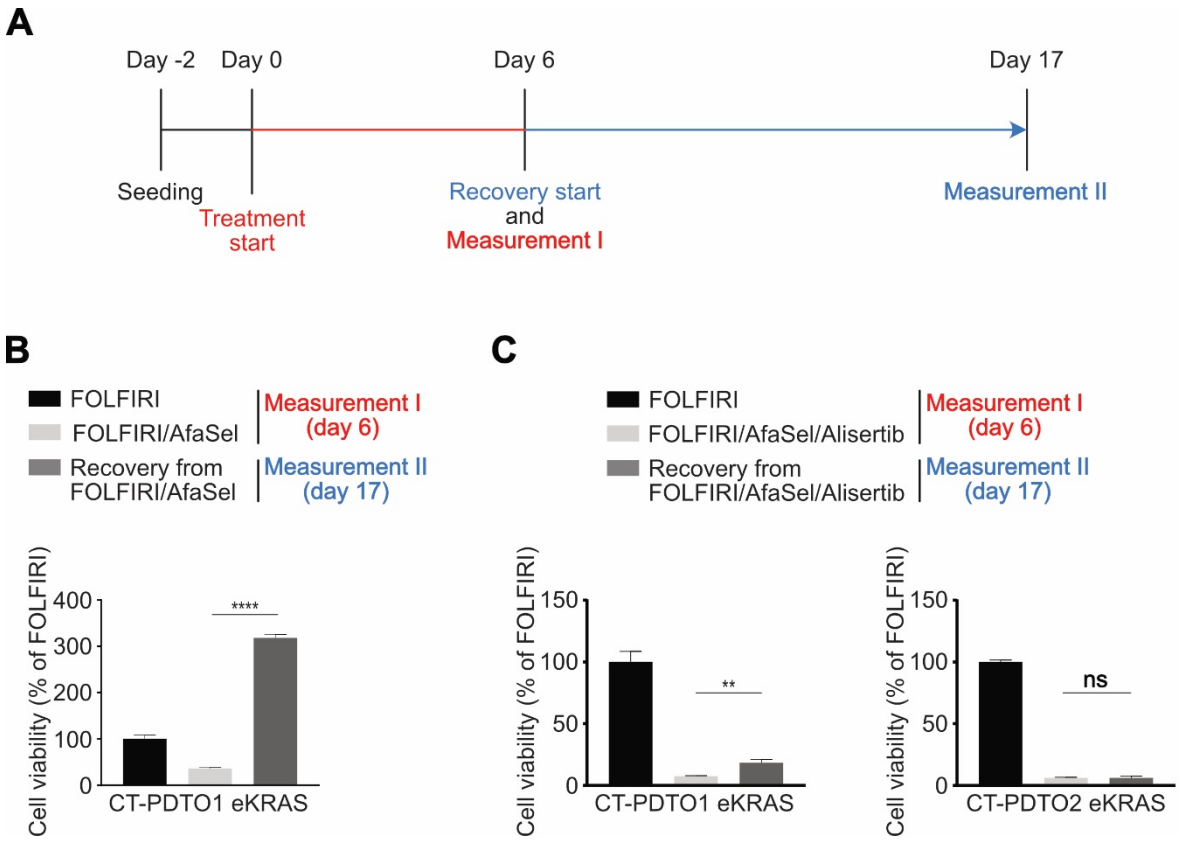

Figure 37: CT-PDTO recovery after drug removal

A) Experimental design: CT-PDTO1 eKRAS and CT-PDTO2 eKRAS were treated for 6 days with FOLFIRI, FOLFIRI/AfaSel, or FOLFIRI/AfaSel/Alisertib and then either measured for cell viability (red, first two bars in each graph in B and C) or left to recover for 11 additional days in the absence of drugs and then measured for cell viability (blue, third bar in each graph in B and C). **B, C)** Cell viability measurements as described in panel A. Measurements were normalized to FOLFIRI treatment after 6 days of treatment. Statistical significance was assessed by a t-test and is indicated by asterisks (**: p-value ≤ 0.01, ****: p-value ≤ 0.0001, ns: p-value > 0.05). Mean + SD, n = 3. AfaSel: pan-HER inhibitor Afatinib plus MEK inhibitor Selumetinib, 50 nM each; Alisertib: AURKA inhibitor, 200 nM.

5.9 Differential AURKA expression in liver, lung, and non-metastatic CRC

Increased levels of AURKA in primary and liver metastasized colorectal tumors have been associated with poor survival, and similar observations have been made in other tumor entities[140,198–202]. However, to our knowledge, AURKA protein levels have not been compared directly between non-metastatic and metastatic CRCs. We performed immunohistochemical staining of AURKA on a cohort of CRC cases in collaboration with Dr. Marlies Michl and Prof. Dr. Jens Neumann (Institute of Pathology, LMU Munich). The cases of this cohort were matched according to T category, grading, and primary tumor site and divided into three groups: non-metastatic (M0), exclusive liver metastatic (M1-HEP), and exclusive lung metastatic (M1-PUL) CRCs. The cohort consists of eighty-two triplets, each containing FFPE slides of a matched M0, an M1-HEP, and an M1-PUL sample[203]. Five slides had to be disregarded due to low numbers of tumor cells, leaving seventy-seven triplets for analysis. Notably, within these seventy-seven triplets, a total of twenty-nine M1 cases were collected directly from the metastases, whereas the other slides were generated from the primary tumors.

In agreement with previous studies[140,198], AURKA staining was mostly nuclear or nuclear-cytoplasmic and limited to a fraction of typically 5 – 40 % of the cells in each tumor area. We quantified the AURKA staining using the H-score, which reconciles both the intensity and the abundance of the staining[174] (Figure 38A).

The expression of AURKA was significantly decreased in liver metastatic CRC compared to matched non-metastatic cases. The AURKA staining scores were on average similarly decreased in M1-PUL cases compared to the matched M0 slides, even though this decrease did not reach statistical significance due to a wider spread of the staining scores (Figure 38B). This result was unexpected because AURKA has been described to be associated with poor prognosis in different tumor entities[140,198–201].

To assess the *AURKA* levels in primary CRCs of non-metastatic and metastatic patients on a broader, multi-study scale, Dr. Matjaz Rokavec (Institute of Pathology, LMU Munich) performed an analysis of publicly available RNA sequencing data sets (Figure 38C). Out of the fourteen analyzed patient cohorts, only three datasets showed a statistically significant decrease in *AURKA* mRNA levels in metastatic compared to non-metastatic primary CRCs. No statistically significant differences were detected in the other eleven cohorts, which showed tendencies of either upregulation or downregulation of *AURKA* mRNA in metastatic CRC.

Moreover, RNA sequencing data of patient-matched normal colonic tissue, primary CRC, and liver metastases of CRC of eighteen cases performed by Kim *et al.* are publicly available[204]. Dr. Peter Jung analyzed these data for expression levels of *AURKA*. The primary CRCs and liver metastases of CRC showed a statistically significant upregulation of *AURKA* expression compared to the normal colonic tissue (Figure 38D), whereas there was no difference between the primary tumors and the liver metastases.

Taken together, the publicly available data sets suggest that *AURKA* mRNA levels are not substantially different in metastatic compared to non-metastatic CRCs, although a slight trend towards reduced *AURKA* levels exists in some studies. Therefore, these data do not fully support our findings from the immunohistochemical staining of the M0-M1(HEP)-M1(PUL) cohort of Michl *et al*[203].

Finally, we set out to compare the pattern of AURKA immunohistochemical staining to a marker of poor prognosis in CRC, namely the abundance of nuclear β-catenin (CTNNB1)[205,206]. Michl *et al.*[203] had already assessed the nuclear CTNNB1 scores of the here employed cohort. Using these data, we depicted the AURKA H-score in dependence of the CTNNB1 score (Figure 38E). CRCs with more than 30 % of nuclei positive for β-catenin (CTNNB1 scores 2 and 3) also expressed significantly higher levels of AURKA when compared to cases without any nuclear β-catenin staining. This observation is in agreement with previous studies in CRC and gastric cancer, where increased AURKA levels were shown to enhance Wnt signaling[147,148].

Metastatic tumors with relatively high AURKA levels might display a dependency on AURKA functionality, which is supported by our observation that the AURKA inhibitor Alisertib reduced the cell viability and induced apoptosis in these models (Figure 26, Figure 28, and Figure 29). However, future studies on a higher number of PDTOs with varying amplification scores and heterozygous expression levels of AURKA are necessary to demonstrate the significance of these findings. Nonetheless, we hypothesize that patients with liver metastatic CRC characterized by high AURKA levels might be responsive to the treatment with Alisertib or alternative AURKA inhibitors, possibly in combination with dual EGFR-MAPK pathway inhibition.

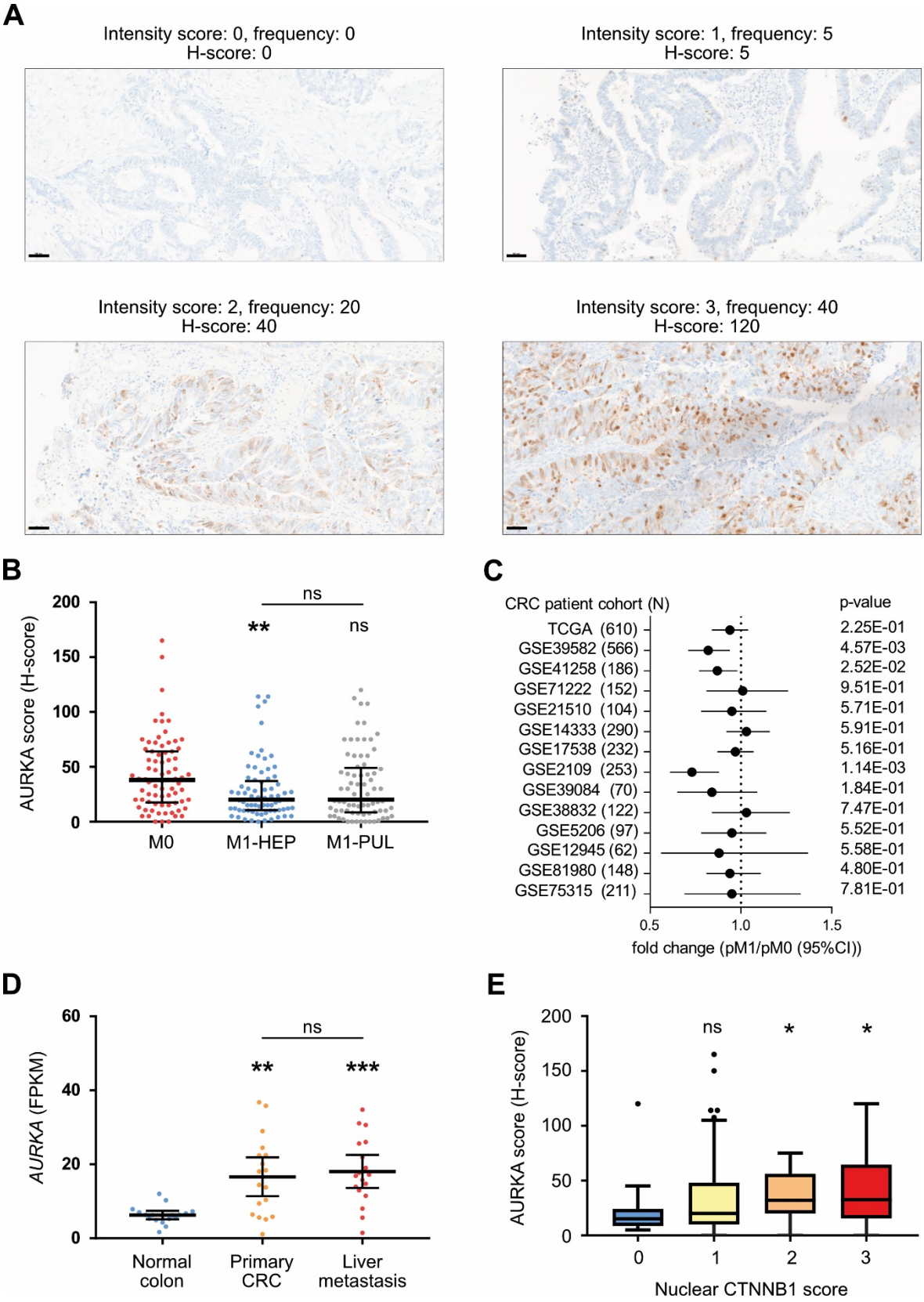

Figure 38: AURKA expression in non-metastatic and metastatic CRC

A) Immunohistochemical staining of AURKA of representative FFPE tissue sections of the M0 – M1 cohort of the primary CRCs. The staining was scored according to the intensity (on a scale from 0 – 3: 0 = no staining, 1 = weak staining, 2 = moderate staining, 3 = strong staining) and frequency

(percentage of AURKA positive cells in 5 % increments). The H-Score was calculated by multiplying the staining intensity and the frequency of a given area. It ranges from 0 to 300. Scale bars indicate 50 µm. **B)** The H-scores of AURKA staining according to their metastatic status: M0 = no metastasis, M1-HEP = exclusively liver metastatic CRC, M1-PUL = exclusively lung metastatic CRC. Each score is indicated by a dot, the median by the black horizontal line, and the interquartile range (IQR) by the error bars. Statistical significance was tested by a one-way repeated measures ANOVA with a Tukey's multiple comparisons test and is indicated by asterisks (**: p-value ≤ 0.01, ns: p-value > 0.05). n = 77. **C)** Forest plot of publicly available RNA sequencing data sets shows the fold change of AURKA expression in primary tumors of metastatic CRC patients (pM1) compared to non-metastatic CRC patients (pM0). Median ± 95 % confidence interval (CI). Number of patients in each cohort (N) is shown. Analysis was performed by Dr. Rokavec. **D)** AURKA expression levels of the publicly available RNA sequencing data set GSE50760 compared in matched normal colonic tissue, primary CRC, and liver metastases of CRC from eighteen patients. Statistical significance was calculated by a one-way repeated measures ANOVA with a Tukey's multiple comparisons test and is indicated by asterisks (**: p-value ≤ 0.01, ***: p-value ≤ 0.001, ns: p-value > 0.05). Analysis was performed by Dr. Peter Jung. **E)** The H-score is shown dependent on the nuclear CTNNB1 score, which ranges from 0 to 3 and indicates the percentage of CTNNB1 positive nuclei (score of 0: 0 %, 1: 1 – 30 %, 2: 31 – 60 %, 3: > 60 % positive nuclei). Box plots show the median AURKA H-score and the IQR. Outliers (> 1.5× IQR) are indicated as black dots. Statistical significance of each CTNNB1 score group compared to the score of 0 was assessed by a one-way ANOVA with a Kruskal-Wallis post-hoc test and is indicated by asterisks (*: p-value ≤ 0.05). Staining was performed by the Diagnostic Department of the Institute of Pathology (LMU Munich) and analyzed by Dr. Jung and Prof. Dr. Neumann.

6 Discussion

One major obstacle of CRC management remains the occurrence of metastases. The poor prognosis of metastatic cases is also underscored by a study from 2021 that analyzed survival data generated from 2010 to 2017[2]. While patients who had been diagnosed with localized CRCs had a five-year relative survival chance of 90 %, this rate went down dramatically to 14 % if distant metastases had been present at the time of diagnosis[2].

This demonstrates the urgent need for new treatment modalities of liver metastatic CRC, especially for the group of patients with a particularly poor prognosis: first-line therapy resistant liver metastatic CRC patients.

Long-term treatment of cancer cells *in vitro* is a common approach for the determination of vulnerabilities of resistant cells and subsequent analysis of new treatments[103,104,207]. However, these studies are often performed in classical two-dimensionally grown cell lines that do not represent the actual tumor disease very well because they omit the interaction among tumor cells in the three-dimensional space and between tumor cells and the extracellular matrix. The surrounding matrix provides tissue stiffness, which triggers a variety of CRC relevant integrin-mediated signaling, such as the Hippo pathway[164]. Moreover, many studies use only one therapeutic compound, which is not representative of first-line treatment. Therefore, these studies might fail to model the actual tumor progression and chemotolerance to clinically employed combination therapies. As a consequence, potential new therapies that are based on these data might disappoint in subsequent preclinical and clinical studies.

To overcome these shortcomings of previous studies, we used a state-of-the-art PDTO system of liver metastatic CRCs. We treated these organoids with FOLFIRI/Cmab, which represents a classical first-line treatment of patients suffering from *KRAS* wild type metastatic CRC.

PDTOs have been acknowledged for their capability to model CRCs *ex vivo*. Ooft *et al.* showed that PDTOs can be used to predict the response of patients to Irinotecan-based chemotherapeutics, such as FOLFIRI, which we used here[173]. Importantly, the drug concentrations we used in our study reflect the plasma concentrations of patients who were treated with these compounds[82,185–188]. Therefore, we consider our PDTO culture system and treatment modality a clinically relevant setting.

6.1 Changes in gene expression rather than resistance-conferring mutations occur during treatment-induced chemotherapy tolerance

Our main objective was to model the development of tolerance towards first-line therapy in MSS liver metastatic CRC responsive to the EGFR-inhibiting antibody Cmab. Therefore, we treated three *KRAS* wild type PDTO lines with the combination chemotherapeutic regimen FOLFIRI/Cmab until PDTOs had developed a chemotherapy tolerant state (CT-PDTOs).

The time until PDTOs exhibited signs of chemotherapy tolerance was quite long with up to 9 months, especially when compared to studies dealing with a pre-existing chemotherapy resistant subclone. For non-small cell lung cancer, Hata *et al*. suggested that in only 1 – 2 months such a resistant subclone takes over the complete culture system[104]. These kinetics reported by Hata *et al.* are in agreement with what we have observed during the selection of our CRISPR/Cas9-mediated genome edited *KRAS* mutant clones, which took over the PDTO culture within 4 – 6 weeks under selective pressure.

From these observations, we hypothesized that putative genetic or transcriptomic alterations of the chemotherapy-adapted CT-PDTOs should represent a *de novo* acquisition of chemotolerance-mediating features instead of the selection of already pre-existing chemotherapy resistant subclones in the PDTO models used in this study.

6.1.1 Mutational analysis of the chemotherapy tolerant and parental PDTOs

Panel sequencing of hot spot mutations in cancer-related genes of parental and CT-PDTOs revealed no differences that could explain the development of tolerance. None of the genetic alterations have been described in connection to chemotherapy resistance against the here applied combinatorial first-line therapy setting.

Treatment with FOLFIRI causes DNA damage and therefore the mutations might have occurred as repair errors without giving the cell any benefit, so-called passenger mutations. Moreover, it was shown that treatment of CRC cell lines with the EGFR-targeting antibody Cmab or with Cmab plus the BRAF inhibitor Dabrafenib reduces the expression of genes of MMR and homologous recombination[208]. Instead, polymerases of error-prone DNA repair mechanisms are upregulated. This observation was also confirmed in Cmab-treated patient-derived xenografts and in tumor samples of patients who underwent treatment with FOLFOX plus the EGFR-inhibiting antibody Panitumumab[208]. Thus, it is possible that not only the FOLFIRI but also the Cmab component in our combination therapy approach

increased the rate of random mutations during long-term treatment. Therefore, the here detected mutations are expected to be passenger mutations.

6.1.2 Transcriptomic analysis of the chemotherapy tolerant and parental PDTOs

Since the development of tolerance towards FOLFIRI/Cmab in the CT-PDTOs could not be explained by mutations in known resistance-conferring genes, we performed RNA sequencing of the PDTO/CT-PDTO pairs to assess changes in transcription.

Seven genes were differentially upregulated, and seventeen genes were differentially downregulated in all three CT-PDTOs compared to their parental counterparts. This small overlap between the different CT-PDTO lines points towards a strong heterogeneity of transcriptional changes between our samples and hence between different patient backgrounds.

Nevertheless, some of these genes have previously been associated with resistance to chemotherapy. For instance, the genes with increased expression after long-term treatment included Olfactomedin 4 (*OLFM4*), which is a stem cell marker[209,210]. In addition, it was suggested that OLFM4 plays a role in the regulation of apoptosis because it was upregulated by and protected cells from treatment with cytotoxic substances[211]. Moreover, upon treatment with Gemcitabine of a pancreatic cancer patient-derived xenograft model, *OLFM4* was upregulated and its knockdown in cell lines increased their sensitivity towards Gemcitabine[212].

TBX2 was also upregulated in all three CT-PDTOs and has been previously implicated as a resistance gene towards different chemotherapeutic agents in different tumor entities[213–216]. In addition, TBX2 was one of four transcription factors implicated in androgen therapy resistance in prostate cancer[217].

The upregulated *SLC29A1* encodes a solute carrier, also known as *ENT1*, which is responsible for the uptake of nucleosides and also imports chemotherapeutic nucleosides such as Gemcitabine and Cytarabine[218]. Its role in FOLFIRI resistance remains unclear, but most studies depict a correlation between low SLC29A1 levels and resistance towards Gemcitabine and Cytarabine, presumably due to decreased drug uptake[219–221]. These observations leave the possibility of an increased sensitivity of FOLFIRI/Cmab-tolerant cancers towards chemotherapeutics that are imported through SLC29A1 transporters, such as Gemcitabine.

Even though we showed a set of genes up- and downregulated in all three CT-PDTOs, the analysis of single genes has its drawbacks[189]: If a pathway X is activated in all three CT-PDTOs, this might not necessarily be represented by upregulation of the same gene in the three CT-PDTOs. Instead, different signaling components can activate this pathway X in the three CT-PDTOs, which would not be detectable as a common feature on the single gene level. Another possibility is that only a slight increase in gene expression of several members might accumulate to an increased activity of this pathway. This case might also go unnoticed on the single gene level because small increases in several genes of a pathway would be disregarded due to cut-offs that are used for defining differentially regulated candidates. These observations are considered in GSEA, which assesses whether a set of genes that is relevant in a certain pathway accumulates at the top or bottom of the list of differentially expressed genes. This approach utilizes ranked files, which consider the fold change (or p-value) for each gene even if the changes on the single gene level might be subtle[189].

Two of the three CT-PDTOs were enriched in the Hallmark gene sets "MYC targets", "E2F targets", and "G_2/M checkpoint". The GSEA results were underscored by immunoblot analyses that also showed increased MYC protein levels in these two CT-PDTOs. These data are in agreement with published studies that associate MYC with chemotherapy resistance. For instance, CRC patients with high levels of *MYC* expression before treatment start had a higher rate of recurrence after 5-FU-based adjuvant chemotherapy[222]. Moreover, in triple negative breast cancer, matched biopsies revealed an increase in *MYC* expression after neoadjuvant chemotherapy when compared to cancer cells prior to the treatment[223]. Another study implicated MYC in resistance to Cisplatin in different cell lines of solid tumors[224].

While the changes on the single gene and on the pathway level observed in our study have been described previously in the context of chemotherapy resistance, these studies mostly focused on other tumor entities and employed different cancer models as well as different treatment strategies than we did. At the same time, the concordance of our data with observations made by others supported our hypothesis that the here detected transcriptomic changes, which represent a common response to tumor therapy in different tumor models, are indeed associated with resistance generation in the CRC PDTO model.

6.2 A potential second-line therapy disappoints in CT-PDTOs

We observed that two of the *KRAS* wild type FOLFIRI/Cmab-tolerant PDTOs had acquired increased expression of MYC targets, E2F targets, and G_2/M checkpoint-related genes during long-term chemotherapy treatment. These lines also responded with a decreased

sensitivity towards a combination of the EGFR/HER inhibitor Afatinib and the MEK inhibitor Selumetinib when compared to parental PDTOs. Cross-resistance towards other therapies is a common phenomenon in clinical oncology and has also been described in different tumor entities and in the context of other drug regimen[105,111,225]. At the same time, it explains why second- and later line therapies are usually not as effective as first-line therapies[63].

Clinical trials that focused on the dual inhibition of the EGFR-MAPK pathway have been mostly disappointing so far. For instance, a study in non-small cell lung cancer compared the EGFR inhibitor Erlotinib as a monotherapy with Erlotinib plus the MEK inhibitor Selumetinib[226]. Toxicities resulted in the administration of lower drug doses and thereby limited the desired effects on tumor progression[226]. Moreover, clinical trials are bound to initially test the new therapeutic compounds in patients who have already undergone multiple lines of therapy. Consequently, these patients might also display a cross-resistance to the new treatment approach, thereby obscuring the potential of some drugs as first-line therapy agents.

Our data on PDTOs, together with the failure of a multitude of clinical trials highlight the importance and potential of *ex vivo* disease modeling and drug testing in first-line therapy sensitive tumor models and their treatment tolerant derivatives. This strategy will presumably allow clinicians to predict the development of cross-resistances of CRC cells during the adaptation to chemotherapy in a patient-specific manner.

Since vertical targeting of the EGFR-MAPK signaling pathway did not achieve the desired effect in FOLFIRI/Cmab-tolerant PDTOs when compared to parental PDTOs, we aimed to tackle alternative, EGFR pathway-independent signaling nodes therapeutically. We had observed increased levels of MYC protein and MYC gene set expression in two out of three CT-PDTO models after acquisition of chemotherapy tolerance. We decided to target the G_2/M checkpoint kinase AURKA for the following reason: AURKA has previously been shown to form a stabilizing complex with MYC, which can be targeted with the AURKA inhibitor Alisertib and thereby can lead to the targeted degradation of MYC via the ubiquitin proteasome pathway[133]. In our setting, this treatment approach succeeded to reduce the cell viability and, more importantly, to induce apoptosis, which was at least partially dependent on the AURKA levels: CT-PDTO5 was derived from the tumor with only a mild amplification of the AURKA locus on chromosome 20q13.2, and it expressed the lowest levels of *AURKA* on the mRNA and protein levels among the three CT-PDTO lines studied. The CT-PDTO5 also responded with the lowest sensitivity to the AURKA inhibitor Alisertib

compared to the other two CT-PDTO lines. This indicates a potential correlation in our small sample set between the overall increased AURKA level and the tolerance towards Alisertib. To our knowledge, only one study assessed the correlation between *AURKA* expression and response towards AURKA inhibition[227]. Hook *et al.* reported that in a panel of cancer cell lines, the growth inhibitory response towards single treatment with the AURKA and AURKB inhibitor PF-03814735 was negatively correlated with the *AURKA* mRNA expression[227]. However, it should be noted that this compound not only inhibits AURKA and AURKB, but also several other kinases, including FLT1 (fms related receptor tyrosine kinase 1, a member of the vascular endothelial growth factor receptor family), MET, and FGFR1 (fibroblast growth factor receptor 1). In addition, it has not been reported that this inhibitor can change the conformation of AURKA or prevent its interaction with MYC. Therefore, it is possible that the two inhibitors, Alisertib and PF-03814735, rely on different mechanisms of action and thus are associated with alternative markers for treatment effectiveness. Future studies are warranted to assess on a larger scale whether liver metastatic CRCs with FOLFIRI/Cmab-induced enrichment of MYC and E2F signaling and high AURKA expression levels are especially sensitive to AURKA targeting.

6.3 Introduction of a *KRAS* mutation into drug persister PDTOs

Clinical trials showed that mutations in the oncogenes *KRAS*, *NRAS*, *BRAF*, or *PIK3CA* render cells irresponsive to anti-EGFR therapy, for instance with Cmab[95,96]. Misale *et al.* generated anti-EGFR resistant CRC cell lines by long-term treatment with either Cmab or Panitumumab[111]. The resulting cell lines harboured *de novo* mutations in *KRAS*, *NRAS*, and *BRAF* genes, and some cell lines even consisted of different sub-populations with different resistance-conferring mutations[111]. In contrast, we did not detect the emergence of *RAS* or *BRAF* mutated clones in the three chemotherapy tolerant PDTO lines even after 9 months of treatment. This difference between our data and the study by Misale *et al*. could stem from the addition of FOLFIRI in our study. This chemotherapeutic regimen might have been more efficient at eliminating drug persister cells that are susceptible to *de novo* acquisition of resistance-conferring mutations. An even longer treatment until complete resistance towards FOLFIRI/Cmab might have allowed the emergence of *KRAS* or *BRAF* mutated clones in our treatment setting.

Therefore, we set out to model the situation systematically where long-term treatment with FOLFIRI/Cmab leads to the acquisition of a *de novo* mutation in *KRAS* in subclones of drug persister cells. We achieved this by introducing a CRISPR/Cas9-engineered $KRAS^{G12D}$

mutation via transient transfection of Cas9 ribonucleoproteins in pools of FOLFIRI/Cmab tolerant CT-PDTOs. Subsequent selection with Cmab led to the enrichment of *KRAS* mutant cells within 4 – 6 weeks, which demonstrated their growth dominance in a situation of chemotherapeutic selective pressure. This timeline is also in agreement with published kinetics by Hata *et al*., who demonstrated that the selection of a pre-existing resistant subclone takes approximately 1 – 2 months to take over a culture system, in which the bulk of tumor cells is initially sensitive towards the treatment[104].

The introduction of oncogenic *KRAS* reduced the sensitivity towards EGFR monotherapy (Cmab) as well as dual EGFR-MEK inhibition (AfaSel) even further compared to the FOLFIRI/Cmab-tolerant but *KRAS* wild type CT-PDTOs. These proof-of-concept experiments confirm that even when drug persister cells show enhanced tolerance towards first-line therapy through the deregulation of apoptotic and proliferative transcriptional programs, the *de novo* acquisition of a *KRAS* mutation renders them even more resistant to the first-line as well as putative second-line therapies.

6.4 Treatment of *KRAS* mutated drug persister cells with a combination of an AURKA inhibitor and dual targeting of the EGFR-MAPK pathway

Even after decades of research, there is still no well-established and successful therapy for most *KRAS* mutant tumor entities. One approach is to target MEK in combination with other components of the EGFR, MAPK, or PI3K pathways. While this scheme showed some benefit *in vitro*[228,229], the respective clinical studies were disappointing. Several trials were discontinued due to high systemic toxicities[113,114,226]. Recently, the combination of Afatinib and Selumetinib, which we also employed in our study, was assessed in a phase I clinical trial in *KRAS* mutant tumors, including nineteen CRC patients[64]. In agreement with our data on *KRAS* mutant chemotherapy tolerant PDTOs, this combination was ineffective at feasible drug doses in patients and a subsequent phase II study is not planned[64]. However, this study and two other phase I clinical trials, which evaluated the combination of pan-HER and MEK inhibition in *KRAS* mutant tumors, concluded that this combination is more effective in non-small cell lung cancer compared to CRC[64,230,231].

Preclinical studies in CRC PDTOs showed that even high doses of dual EGFR-MAPK pathway inhibitors do not elicit apoptosis in *KRAS* mutant tumor cells but only lead to a transient halt in proliferation[112]. This is also in agreement with our observation that PDTO1 with wild type *KRAS* but not the isogenic *KRAS* mutant PDTO1 eKRAS responds to a 48-hour AfaSel treatment with induction of apoptosis. Furthermore, we showed that even after

a prolonged treatment of 6 days, the majority of CT-PDTO1 eKRAS organoids recovered once the treatment was discontinued. These data provide a molecular explanation why clinical trials failed.

Interestingly, Verissimo *et al.* showed that even though the dual blockade of EGFR and MEK cannot elicit an apoptotic response in *KRAS* mutant CRC PDTOs, it primes the cells for apoptosis induction by BCL2/BCL-XL inhibition[112]. However, this treatment approach proved toxic *in vivo* at drug doses necessary to eradicate *KRAS* mutant PDTOs[112]. Still, this study highlighted an important proof-of-concept. It demonstrated the possibility to prime *KRAS* mutant tumors with dual inhibition of EGFR and MEK. This priming lowers the threshold of apoptosis induction by co-targeting of other pathways, on which the cytostatic cancer cells rely on for their survival.

Another indication to treat *KRAS* mutant tumors with inhibitors of alternative pathways came from Kapoor *et al*[102]: This study examined the effect of doxycycline omission in a doxycycline-inducible $Kras^{G12D}$ mouse model of pancreatic ductal adenocarcinoma after the establishment of tumors. This so-called $Kras^{G12D}$ extinction led to the growth of $Kras^{G12D}$ and Mapk signaling-independent tumors. Instead, the tumors showed a strong dependency on Yap1/Tead2-mediated cell cycle progression. Notably, the bypass of Kras signaling also induced *Aurka* and *Aurkb* expression[102]. This observation led us to hypothesize that elevated Aurka and/or Aurkb functionality might contribute to the survival of KRAS-independent cancer cells and might therefore represent an Achilles heel of CRC cells in a context of cytostatic RAS signaling blockade.

Other studies also suggested the combination of EGFR-MAPK pathway inhibitors with AURKA inhibition in different tumor entities. For instance, a study in non-small cell lung cancer reported that EGFR inhibitor treatment activated AURKA[232]. Simultaneous targeting of EGFR and AURKA in these tumors was demonstrated to be synergistic[232].

To follow this targeting approach, we combined the dual EGFR/MEK inhibition with targeting of the G_2/M checkpoint kinase AURKA in *KRAS* mutant CRC models. The combination proved more effective than single treatments: It impaired the cell viability, elicited apoptosis, and largely prevented the organoid reformation capacity after drug removal.

Verissimo *et al.* proposed to combine the dual EGFR/MEK inhibition with inhibitors of other pathways and used the BCL-inhibitor navitoclax[112]. However, due to high toxicities of effective drug doses, this combination proved unfeasible[112]. Compared to the study by Verissimo, we were able to decrease the AfaSel concentration 10- to 20-fold and still noticed

a powerful induction of apoptosis upon the dual EGFR-MAPK pathway and AURKA inhibition. Thus, these data confirm that the combination of compatible drugs allows the reduction of the concentration of each single drug, which might allow tumor regression with lower toxicities in patients.

Importantly, the only phase III clinical trial reported Alisertib to be well tolerated[157]: Fewer patients showed adverse events in the Alisertib treatment group compared to the comparator group. Consequently, Alisertib-treated patients discontinued their treatment less often because of treatment-induced adverse events than the comparator-treated patients. Nevertheless, this study was discontinued because single treatment with Alisertib alone did not prove more effective than comparator treatment in T cell lymphoma in respect to progression-free survival[157]. This underlines the importance of combining different treatment regimen that are superior to single agents in terms of the tumor regression. Optimally, these combinations would simultaneously allow the use of lower drug doses and thereby reduce adverse events in patients.

Future studies and clinical trials are necessary to evaluate the efficacy and toxicity of the proposed AURKA inhibition in dual EGFR-MAPK pathway primed *KRAS* mutant CRCs. A similar set up is tested while this thesis manuscript was in preparation: A clinical phase I/ Ib assesses the safety and tolerability of Alisertib with the EGFR inhibitor Osimertinib in EGFR mutant metastatic lung cancers (NCT04085315, clinicaltrials.gov, accessed on April 10, 2021).

Whereas a variety of clinically proven EGFR and MEK inhibitors are available, only a few AURKA inhibitors have been developed to date. More specific inhibitors with fewer off-targets would allow lower doses and limit side effects. Intriguingly, Adhikari *et al.* developed a proteolysis targeting chimera (PROTAC) to target AURKA: They linked Alisertib to an E3 ligase-binding molecule[233]. This PROTAC targets AURKA specifically via Alisertib and induces its proteasomal degradation. Subsequently, the treated cancer cell lines undergo apoptosis. Both Alisertib and the PROTAC are very specific for AURKA, but have a few off-targets, such as AURKB. Alisertib binds AURKA with an affinity that was more than 10-fold stronger than its affinity towards AURKB (K_d of 7 nM for AURKA versus 90 nM for AURKB). This difference in affinity was even greater for the Alisertib-based PROTAC (K_d of 99 nM for AURKA versus 5.1 µM for AUKRB). More importantly, even though the PROTAC was able to bind to these off-targets in a cell-free assay, none of the potential off-targets were degraded in a cellular assay[233].

In agreement with our data, Davis *et al.* reported an advantage of combined MEK and AURKA inhibition in MSI CRC cell lines in two-dimensional culture[234]. In our study, we used a similar treatment scheme but addressed a few drawbacks of the publication by Davis *et al.*: First, we studied MSS CRC cases, which occur more frequently than MSI CRC. Second, we utilized a clinically more representative PDTO model instead of two-dimensionally grown cell lines. Third, we could demonstrate that the combinatorial treatment proved effective in a first-line therapy tolerant setting with a gained $KRAS^{G12D}$ mutation. Therefore, we conclude that our study has extended the knowledge of combinatorial therapy in clinically important aspects.

Notably, the induction of apoptosis upon targeting of the EGFR-MAPK pathway and AURKA was stronger in those organoid lines where the FOLFIRI/Cmab tolerance generation had increased MYC levels before the introduction of the *KRAS* mutation. Moreover, MYC protein levels were reduced in the combined EGFR/MEK and AURKA inhibition. This may be attributed to the destruction of MYC protein upon Alisertib treatment, which was shown to prevent the formation of a MYC-stabilizing complex with AURKA in liver cancer[133]. The association between AURKA and MYC family members is also supported by studies that show that AURKA stabilizes N-MYC in neuroblastoma[154,155,235]. In addition, a study in a cancer cell line panel showed a positive correlation between MYC expression levels and the growth inhibitory response towards the AURKA and AURKB inhibitor PF-03814735[227].

The EGFR/MEK inhibition alone was able to reduce MYC levels partially in CT-PDTO1 eKRAS, indicating that also other effects that are independent of the AURKA-MYC complex might contribute to the reduction of MYC protein. Therefore, it needs further investigation to clarify whether the reduced MYC levels in the combined AURKA/EGFR/MEK inhibition stem from a potential prevention of AURKA-MYC complexes or whether it is an indirect outcome of reduced PDTO cell proliferation and hence triggered by an alternative mechanism.

Diaz *et al.* showed that even prior to chemotherapy treatment of CRCs with targeted therapy, subpopulations with resistance-conferring mutations exist in the tumor at levels below the detection limit of current diagnostic methods[236]. Therefore, when first imposing a selection pressure by the treatment, the bulk of the tumor does not contain this mutation, and is chemosensitive, which leads to the shrinkage of the overall tumor mass. This indicates an initially successful therapy. Simultaneously, the few resistant cells gain a proliferative advantage relative to the chemotherapy-stressed tumor bulk, and thereby take over the tumor

mass[236]. This concept was later corroborated by Sottoriva *et al.*, who suggested the Big Bang model of CRC growth. This model postulates that during the initial outgrowth of a tumor the timing of the development of a mutation rather than a potential advantage of this mutation determines its frequency in the tumor mass[237]. This is because an early mutation has more time to expand and because "selective sweeps" are relatively rare during the outgrowth of a newly established tumor. In contrast, anti-cancer treatment can represent such a "selective sweep" that gives these initially undetectable cells with a resistance-conferring mutation an advantage, which leads to its rapid expansion[237]. In addition, Roerink *et al.* used CRC PDTO subclones derived from single tumor cells to show that many treatment naïve CRCs already contain subpopulations with resistance-conferring mutations to most of the commonly used treatments[238].

Even if the tumor does not contain any resistance-conferring mutations at the time of the treatment start, it is likely that prolonged treatment of the tumor induces a drug persister phenotype and that these cells can acquire resistance-conferring mutations[239]. This has been demonstrated in non-small cell lung cancer cells *in vitro*: Single cell clones acquired resistance-conferring mutations in *EGFR*, *NRAS*, and *PIK3CA* upon prolonged treatment with the EGFR inhibitors Gefitinib[104] or Erlotinib[99]. Moreover, data from CRC cell lines confirmed that *de novo* mutations in resistance-conferring genes could develop during prolonged treatment with the EGFR inhibitors Cmab or Panitumumab[111]. These data are also in agreement with a study by Russo *et al.*, who demonstrated that treatment with Cmab or Panitumumab effected DNA repair mechanisms by downregulation of MMR and homologous recombination DNA repair genes in CRC cell lines, patient-derived xenografts, and patients[208]. This resulted in elevated DNA damage, mutability, and MSI[208].

These studies suggest that treatment resistance against many chemotherapeutics as well as targeted therapies is in many cases inevitable, especially when only a single signaling component such as EGFR is targeted. In contrast, combining the therapy with targeting of additional pathway components that are likely to confer resistance to the first-line therapy could prolong the time to relapse[207,236,238]. Therefore, if a tumor already contained a small subpopulation with a *KRAS* mutation, it would be beneficial to treat the tumor from the beginning with a therapeutic regimen that also targets the *KRAS* mutated cells, such as the here proposed dual EGFR/MAPK pathway targeting combined with AURKA inhibition.

6.5 AURKA expression in non-metastatic and metastatic CRCs

In our study, we have used PDTOs of liver metastatic CRCs and have established a potential new treatment for this type of tumor. To determine how the AURKA levels of liver metastatic CRCs compare to those of non-metastatic or lung-metastatic CRCs, we stained a matched cohort for AURKA expression. We showed that AURKA levels in non-metastatic CRCs are increased compared to matched lung and liver metastatic CRCs. This finding was unexpected because AURKA has been shown to be correlated with poor prognosis in different tumor entities, including liver metastatic CRC, which would suggest that its expression should be increased in metastatic compared to non-metastatic CRCs[140,198–201]. One possible explanation is that in our cohort a fraction of metastatic cases was directly derived from the distant metastases and not from the primary tumor. The liver or lung microenvironment might differentially affect the gene and protein expression behaviour of metastasized CRC cells via organ-specific metabolites, growth factors and cytokines, and nutrient and oxygen availability in a different way than the CRC microenvironment at the primary tumor site. This critical aspect limits the comparability and hence the significance of our results. Even though AURKA mRNA and protein levels do not necessarily need to correlate and AURKA is subjected to post-transcriptional modifications, which regulate its cell cycle phase-dependent stability[121], publicly available RNA sequencing data sets hint towards no or only a marginal decrease in *AURKA* levels in primary tumors of metastatic CRCs compared to those of non-metastatic CRC patients.

In addition, the fact that primary tumors and patient-matched liver metastases show elevated AURKA levels compared to the normal colonic epithelium supports our hypothesis that liver metastatic CRCs might benefit from AfaSel/Alisertib treatment. In particular, our results from the state-of-the-art patient-derived tumor organoid model point towards an elevated AURKA dependency in first-line therapy tolerant tumors with high AURKA levels and chemotherapy tolerance-associated enrichment of MYC protein.

AURKA levels also correlated with nuclear β-catenin scores. This is in agreement with studies in glioblastoma that showed that AURKA prevents the destruction of β-catenin as well as publications that demonstrated that AURKA enhanced Wnt signaling[146–148]. Nuclear β-catenin is also a marker for disease progression and metastasis formation[205,206], which indicate an aggressive subset of CRCs. Thus, CRC patients with a high nuclear β-catenin status and elevated AURKA levels should undergo an adapted treatment designed to prevent or delay metastatic disease relapse or reduce an already existing metastatic burden.

In conclusion, our study - which is based on CRC PDTOs, their first-line therapy tolerant counterparts as well as a cohort of CRC tissues with different metastatic properties - implicates AURKA as a promising therapeutic target for liver metastatic CRC. Future studies and clinical trials are necessary to validate the applicability of the here proposed combined treatment strategy of a dual EGFR-MEK inhibition with AURKA blockade in MSS liver metastatic CRCs, especially those that display MYC activation after failure of prolonged first-line therapy.

7 Summary

Metastatic spread and resistance to chemotherapy still limit the treatment success of current colorectal cancer therapy, even though multimodal treatment approaches have improved and prolonged patient survival.

Here, we used state-of-the-art patient-derived tumor organoids (PDTOs) of liver metastatic colorectal cancer to model the generation of tolerance towards chemotherapy. We achieved this by long-term *ex vivo* treatment of *KRAS* wild type PDTOs with a clinically employed first-line therapy consisting of the chemotherapeutic regimen FOLFIRI plus the EGFR-targeting antibody Cetuximab.

After up to 9 months of treatment, the PDTOs generated a tolerance towards FOLFIRI/Cetuximab and failed to induce an efficient apoptotic response. This phenotype occurred without the gain of resistance-conferring mutations in clinically relevant genes. Instead, unbiased whole transcriptome sequencing (next generation RNA sequencing) revealed an enrichment in MYC target gene expression in two out of three tolerant PDTO lines. The third PDTO line developed the tolerance towards first-line therapy via a different mechanism, which included upregulation of interferon-α-related gene expression.

Intriguingly, all three tolerant PDTO lines were derived from tumors with a genomic amplification of the chromosomal region 20q13.2, which contains the Aurora kinase A (*AURKA)* locus, and displayed elevated mRNA and protein levels of AURKA compared to normal colonic epithelium. Treatment with the AURKA inhibitor Alisertib, which also represents a strategy to target MYC indirectly in different cancer types, restored an apoptotic response in the three established chemotherapy tolerant PDTO lines.

We then introduced a $KRAS^{G12D}$ mutation into the FOLFIRI/Cetuximab tolerant PDTO lines via CRISPR/Cas9-mediated genomic engineering and confirmed that this clinically problematic mutation confers resistance towards therapeutic approaches of single or dual targeting of the EGFR-MAPK pathway.

Notably, the combination of dual targeting of the EGFR-MAPK pathway with inhibition of AURKA reduced the cell viability of first-line chemotherapy tolerant *KRAS* mutant PDTOs to a higher extent than each treatment alone. More importantly, the treatment with the AURKA inhibitor restored the apoptotic response and largely diminished the tumor organoid reformation capacity in *KRAS* mutant PDTOs, sensitized by dual EGFR-MAPK pathway inhibition. This combination treatment strategy was especially effective in the two PDTO

lines that had developed increased MYC levels after acquisition of tolerance to first-line therapy.

To obtain a deeper insight into AURKA expression levels in metastatic disease, we performed immunohistochemical staining of AURKA of CRCs of a matched patient cohort. Here, we observed that AURKA expression was slightly increased in non-metastatic colorectal cancers compared to liver or lung metastatic colorectal cancers. Moreover, the AURKA expression was positively correlated with the abundance of nuclear beta-catenin, which is a marker of aggressive disease and poor overall patient survival.

In conclusion, this Ph.D. thesis provides evidence for the potential of patient-derived tumor organoids for the *ex vivo* modeling of colorectal cancer therapy tolerance, mutational disease progression, and the evaluation of drug combinations to overcome treatment resistance in a preclinical setting.

8 Zusammenfassung

Metastasierung und Resistenzen gegenüber Chemotherapie limitieren die Behandlungsmöglichkeiten des kolorektalen Karzinoms, obwohl multimodale Behandlungsansätze das Überleben der Patienten verbessert und verlängert haben.

Wir haben Patienten-abgeleitete Tumor-Organoide (englisch: patient-derived tumor organoids, PDTOs) des lebermetastasierten kolorektalen Karzinoms angewandt, um die Entwicklung einer Toleranz gegenüber Chemotherapie nachzubilden. Das erreichten wir, indem wir die *KRAS*-wildtyp PDTOs *ex vivo* einer Langzeitbehandlung mit einer klinisch üblichen Erstlinientherapie unterzogen, die aus der Chemotherapie-Doublette FOLFIRI und dem EGFR-spezifischen Antikörper Cetuximab besteht.

Nach einer bis zu neun Monate andauernden Behandlung entwickelten die PDTOs eine Toleranz gegenüber FOLFIRI/Cetuximab und reagierten nicht mehr mit Apoptose auf diese Behandlung. Dieser Phänotyp trat unabhängig von Resistenz-vermittelnden Mutationen in klinisch relevanten Genen auf. Stattdessen offenbarte die Sequenzierung des gesamten Transkriptoms (RNA-Sequenzierung der nächsten Generation) eine Induktion der Expression von MYC-Zielgenen in zwei von drei toleranten PDTO-Linien. Die dritte PDTO-Linie entwickelte eine Toleranz gegenüber der Erstlinientherapie durch andere Mechanismen, welche die Hochregulierung von Interferon-α-Zielgenen beinhalteten.

Interessanterweise stammten alle drei PDTO-Linien von Tumoren ab, die genomische Amplifikation des chromosomalen Bereichs 20q13.2 zeigten, welcher den Aurora Kinase A (*AURKA*) Locus enthält. Weiterhin zeigten diese Ursprungstumore erhöhte AURKA mRNA- und Proteinmengen im Vergleich zu normalem Kolonepithel. Eine Behandlung mit dem AURKA-Inhibitor Alisertib stellt eine Strategie zur indirekten MYC-Inhibition in verschiedenen Tumorarten dar und induzierte Apoptose in den drei hier etablierten chemotoleranten PDTO-Linien.

Anschließend führten wir mittels CRISPR/Cas9-vermittelter Genommanipulation eine $KRAS^{G12D}$-Mutation in die FOLFIRI/Cetuximab-toleranten PDTO-Linien ein. Wir bestätigten, dass diese klinisch problematische Mutation eine Resistenz gegenüber Ansätzen der einfachen oder dualen Inhibition des EGFR-MAPK-Signalwegs vermittelt.

Interessanterweise reduzierte die Kombination aus dualer Inhibition des EGFR-MAPK-Signalweges und AURKA-Hemmer die Zellviabilität der Erstlinientherapie-toleranten *KRAS*-mutierten PDTOs in größerem Ausmaß als die jeweiligen Einzelbehandlungen. Zudem führte die Behandlung mit dem AURKA-Inhibitor von *KRAS*-mutierten PDTOs, die

durch die Inhibierung des EGFR-MAPK-Signalweges sensibilisiert wurden, zu einer Wiederherstellung der Apoptosereaktion und reduzierte zum Großteil die Reetablierungskapazität der Organoide nach Behandlung. Diese Strategie der Kombinationsbehandlung war besonders erfolgreich in den beiden PDTO-Linien, die erhöhte MYC-Level nach der Ausbildung der Toleranz gegenüber der Erstlinientherapie gezeigt hatten.

Um einen tieferen Einblick in das AURKA-Expressionslevel in metastasierten Fällen zu erhalten, führten wir einen immunhistochemischen Nachweis von AURKA in einer gepaarten Kohorte von Patienten mit kolorektalen Krebserkrankung durch. Dabei beobachteten wir, dass die AURKA-Expression in nicht-metastasierten kolorektalen Karzinomen im Vergleich zu exklusiv lebermetastasierten oder lungenmetastasierten kolorektalen Karzinomen leicht erhöht war. Weiterhin korrelierte die AURKA-Expression positiv mit der Abundanz von nukleärem Beta-Catenin, welches ein bekannter Marker für eine aggressive Erkrankung und eine schlechte Überlebensrate der Patienten ist.

Letztendlich betont diese Ph.D.-Arbeit das Potential von PDTOs als *ex vivo* Modell für die Therapietoleranz des kolorektalen Karzinoms, für das mutationsbasierte Fortschreiten der Tumorkrankheit sowie für die Evaluierung solcher Wirkstoffkombinationen zu dienen, die in der Lage sind, Behandlungsresistenzen in einem präklinischen Setting zu überwinden.

9 References

1. Sung, H. *et al.* Global Cancer Statistics 2020: GLOBOCAN Estimates of Incidence and Mortality Worldwide for 36 Cancers in 185 Countries. *CA. Cancer J. Clin.* **71**, 209–249 (2021).
2. Siegel, R. L., Miller, K. D., Fuchs, H. E. & Jemal, A. Cancer Statistics, 2021. *CA. Cancer J. Clin.* **71**, 7–33 (2021).
3. Hanahan, D. & Weinberg, R. A. Hallmarks of Cancer: The Next Generation. *Cell* **144**, 646–674 (2011).
4. Hanahan, D. & Weinberg, R. A. The Hallmarks of Cancer. *Cell* **100**, 57–70 (2000).
5. Modest, D. P. *et al.* Surgical treatment options following chemotherapy plus cetuximab or bevacizumab in metastatic colorectal cancer—central evaluation of FIRE-3. *Eur. J. Cancer* **88**, 77–86 (2018).
6. Van Cutsem, E. *et al.* ESMO consensus guidelines for the management of patients with metastatic colorectal cancer. *Ann. Oncol.* **27**, 1386–1422 (2016).
7. Munkholm, P. The incidence and prevalence of colorectal cancer in inflammatory bowel disease. *Aliment Pharmaol Ther* **18**, 1–5 (2003).
8. Müller, M. F., Ibrahim, A. E. K. & Arends, M. J. Molecular pathological classification of colorectal cancer. *Virchows Arch.* **469**, 125–134 (2016).
9. Brenner, H., Kloor, M. & Pox, C. P. Colorectal cancer. *Lancet* **383**, 1490–1502 (2014).
10. Cho, E. *et al.* Alcohol Intake and Colorectal Cancer: A Pooled Analysis of 8 Cohort Studies. *Ann. Intern. Med.* **140**, 603–614 (2004).
11. Bardou, M., Barkun, A. N. & Martel, M. Obesity and colorectal cancer. *Gut* **62**, 933–947 (2013).
12. Cross, A. J. *et al.* A Large Prospective Study of Meat Consumption and Colorectal Cancer Risk: An Investigation of Potential Mechanisms Underlying this Association. *Cancer Res.* **70**, 2406–2414 (2010).
13. Willett, W. C., Stampfer, M. J., Colditz, G. A., Rosner, B. A. & Speizer, F. E. Relation of Meat, Fat, and Fiber Intake to the Risk of Colon Cancer in a Prospective Study among Women. *N. Engl. J. Med.* **323**, 1664–1672 (1990).
14. Kumar, V., Abbas, A. K. & Aster, J. C. *Robbins Basic Pathology*. (Elsevier Saunders, 2013).
15. Sinkovics, J. G. *RNA/DNA and Cancer*. *Spring* vol. 644 (Springer International

Publishing AG Switzerland, 2009).

16. Lüllmann-Rauch, R. *Taschenlehrbuch Histologie*. (Georg Thieme Verlag, 2009).
17. Clevers, H. The Intestinal Crypt, A Prototype Stem Cell Compartment. *Cell* **154**, 274–284 (2013).
18. Van der Flier, L. G. & Clevers, H. Stem Cells, Self-Renewal, and Differentiation in the Intestinal Epithelium. *Annu. Rev. Physiol.* **71**, 241–260 (2009).
19. Sato, T. *et al.* Paneth cells constitute the niche for Lgr5 stem cells in intestinal crypts. *Nature* **469**, 415–418 (2011).
20. Korinek, V. *et al.* Depletion of epithelial stem-cell compartments in the small intestine of mice lacking Tcf-4. *Nat. Genet.* **19**, 379–383 (1998).
21. Ireland, H. *et al.* Inducible Cre-Mediated Control of Gene Expression in the Murine Gastrointestinal Tract: Effect of Loss of beta-Catenin. *Gastroenterology* **126**, 1236–1246 (2004).
22. Kuhnert, F. *et al.* Essential requirement for Wnt signaling in proliferation of adult small intestine and colon revealed by adenoviral expression of Dickkopf-1. *PNAS* **101**, 266–271 (2004).
23. Kim, K. A. *et al.* Mitogenic influence of human R-spondin1 on the intestinal epithelium. *Science* **309**, 1256–1259 (2005).
24. van Es, J. H. *et al.* Wnt signalling induces maturation of Paneth cells in intestinal crypts. *Nat. Cell Biol.* **7**, 381–386 (2005).
25. Santos, A. J. M., Lo, Y., Mah, A. T. & Kuo, C. J. The Intestinal Stem Cell Niche: Homeostasis and Adaptations. *Trends Cell Biol* **28**, 1062–1078 (2018).
26. Fearon, E. F. & Vogelstein, B. A Genetic Model for Colorectal Tumorigenesis. *Cell* **61**, 759–767 (1990).
27. Pinto, D. & Clevers, H. Wnt, stem cells and cancer in the intestine. *Biol. Cell* **97**, 185–196 (2005).
28. Fearon, E. R. Molecular Genetics of Colorectal Cancer. *Annu. Rev. Pathol. Mech. Dis* **6**, 479–507 (2011).
29. Network Cancer Genome Atlas, T. Comprehensive molecular characterization of human colon and rectal cancer. *Nature* **487**, 330–337 (2012).
30. Kinzler, K. W. & Vogelstein, B. Lessons from Hereditary Colorectal Cancer. *Cell* **87**, 159–170 (1996).
31. Sparks, A. B., Morin, P. J., Vogelstein, B. & Kinzler, K. W. Mutational Analysis of the APC/β-Catenin/Tcf Pathway in Colorectal Cancer. *Cancer Res.* **58**, 1130–1134

(1998).

32. Takagi, Y. *et al.* Somatic Alterations of the DPC4 Gene in Human Colorectal Cancers In Vivo. *Gastroenterology* **111**, 1369–1372 (1996).
33. Aberle, H., Bauer, A., Stappert, J., Kispert, A. & Kemler, R. β-catenin is a target for the ubiquitin-proteasome pathway. *EMBO J.* **16**, 3797–3804 (1997).
34. Kitagawa, M. *et al.* An F-box protein, FWD1, mediates ubiquitin-dependent proteolysis of β-catenin. *EMBO J.* **18**, 2401–2410 (1999).
35. Bhanot, P. *et al.* A new member of the frizzled family from Drosophila functions as a Wingless receptor. *Nature* **382**, 225–230 (1996).
36. Wehrli, M. *et al.* arrow encodes an LDL-receptor-related protein essential for Wingless signalling. *Nature* **407**, 527–530 (2000).
37. Nusse, R. & Clevers, H. Wnt/β-Catenin Signaling, Disease, and Emerging Therapeutic Modalities. *Cell* **169**, 985–999 (2017).
38. Janda, C. Y., Waghray, D., Levin, A. M., Thomas, C. & Garcia, K. C. Structural basis of Wnt recognition by Frizzled. *Science* **337**, 59–64 (2012).
39. Fiedler, M., Mendoza-Topaz, C., Rutherford, T. J., Mieszczanek, J. & Bienz, M. Dishevelled interacts with the DIX domain polymerization interface of Axin to interfere with its function in down-regulating β-catenin. *PNAS* **108**, 1937–1942 (2011).
40. Molenaar, M. *et al.* XTcf-3 transcription factor mediates β-catenin-induced axis formation in xenopus embryos. *Cell* **86**, 391–399 (1996).
41. Behrens, J. *et al.* Functional interaction of β-catenin with the transcription factor LEF-1. *Nature* **382**, 638–642 (1996).
42. Schneikert, J. & Behrens, J. The canonical WNT signalling pathway and its APC partner in colon cancer development. *Gut* **56**, 417–425 (2007).
43. He, T. C. *et al.* Identification of c-MYC as a Target of the APC Pathway. *Science* **281**, 1509–1512 (1998).
44. Wang, C. *et al.* Alternative approaches to target Myc for cancer treatment. *Signal Transduct. Target. Ther.* **6**, (2021).
45. Vennstrom, B., Sheiness, D., Zabielski, J. & Bishop, J. M. Isolation and Characterization of c-myc, a Cellular Homolog of the Oncogene (v-myc) of Avian Myelocytomatosis Virus Strain 29. *J. Virol.* **42**, 773–779 (1982).
46. Schwab, M. *et al.* Amplified DNA with limited homology to myc cellular oncogene is shared by human neuroblastoma cell lines and a neuroblastoma tumour. *Nature*

305, 245–248 (1983).

47. Zelinski, T. *et al.* Confirmation of the assignment of MYCL to chromosome 1 in humans and its position relative to RH, UMPK, and PGM1. *Genomics* **2**, 154–156 (1988).
48. Delattre, O. *et al.* Multiple genetic alterations in distal and proximal colorectal cancer. *Lancet* **334**, 353–355 (1989).
49. Vogelstein, B. *et al.* Genetic alterations during colorectal-tumor development. *N. Engl. J. Med.* **319**, 525–532 (1988).
50. Batlle, E. & Massagué, J. Transforming Growth Factor-β Signaling in Immunity and Cancer. *Immunity* **50**, 924–940 (2019).
51. David, C. J. & Massagué, J. Contextual determinants of TGFβ action in development, immunity and cancer. *Nat. Rev. Mol. Cell Biol.* **19**, 419–435 (2018).
52. Papageorgis, P. *et al.* Smad4 Inactivation Promotes Malignancy and Drug Resistance of Colon Cancer. *Cancer Res.* **71**, 998–1008 (2011).
53. Massagué, J., Blain, S. W. & Lo, R. S. TGFβ signaling in growth control, cancer, and heritable disorders. *Cell* **103**, 295–309 (2000).
54. Lane, D. P. p53, guardian of the genome. *Nature* **358**, 15–16 (1992).
55. Munro, A. J., Lain, S. & Lane, D. P. P53 abnormalities and outcomes in colorectal cancer: a systematic review. *Br. J. Cancer* **92**, 434–444 (2005).
56. Nakayama, M. & Oshima, M. Mutant p53 in colon cancer. *J. Mol. Cell Biol.* **11**, 267–276 (2019).
57. Salomao, N. *et al.* What do we need to know and understand about p53 to improve its clinical value? *J. Pathol.* **254**, 443 – 453 (2021).
58. Normanno, N. *et al.* Epidermal growth factor receptor (EGFR) signaling in cancer. *Gene* **366**, 2–16 (2006).
59. Cicenas, J. *et al.* KRAS, NRAS and BRAF mutations in colorectal cancer and melanoma. *Med. Oncol.* **34**, (2017).
60. Ternet, C. & Kiel, C. Signaling pathways in intestinal homeostasis and colorectal cancer: KRAS at centre stage. *Cell Commun. Signal.* **19**, (2021).
61. Gaspar, V. I., Catozzi, S., Ternet, C., Luthert, P. J. & Kiel, C. Analysis of Ras-effector interaction competition in large intestine and colorectal cancer context. *Small GTPases* **12**, 209–225 (2021).
62. Nguyen, L. H., Goel, A. & Chung, D. C. Pathways of Colorectal Carcinogenesis. *Gastroenterology* **158**, 291–302 (2020).

63. German Guideline Programm in Oncology (German Cancer Society. German Cancer Aid. AWMF). S3-Guideline Colorectal Cancer, long version 2.1, 2019, AWMF registrationnumber: 021-007OL. *AWMF registrationnumber: 021-007OL* 1–322 http://www.leitlinienprogramm-onkologie.de/leitlinien/kolorektales-karzinom/ (2019).
64. van Brummelen, E. M. J. *et al.* Phase I Study of Afatinib and Selumetinib in Patients with KRAS-Mutated Colorectal, Non-Small Cell Lung, and Pancreatic Cancer. *Oncologist* **26**, 290-e545 (2021).
65. Timmermann, B. *et al.* Somatic Mutation Profiles of MSI and MSS Colorectal Cancer Identified by Whole Exome Next Generation Sequencing and Bioinformatics Analysis. *PLoS One* **5**, (2010).
66. Li, L. *et al.* Tumor-derived mutations in postoperative plasma of colorectal cancer with microsatellite instability. *Transl. Oncol.* **14**, (2021).
67. Boland, C. R. *et al.* A National Cancer Institute Workshop on Microsatellite Instability for Cancer Detection and Familial Predisposition: Development of International Criteria for the Determination of Microsatellite Instability in Colorectal Cancer. *Cancer Res.* **58**, 5248–5257 (1998).
68. Cunningham, J. M. *et al.* Hypermethylation of the hMLHl Promoter in Colon Cancer with Microsatellite Instability. *Cancer Res.* **58**, 3455–3460 (1998).
69. Rad, R. *et al.* A Genetic Progression Model of BrafV600E-Induced Intestinal Tumorigenesis Reveals Targets for Therapeutic Intervention. *Cancer Cell* **24**, 15–29 (2013).
70. Peltomäki, P., Vasen, H. F. A. & international collaborative group on hereditary nonpolyposis colorectal cancer, T. Mutations predisposing to hereditary nonpolyposis colorectal cancer: database and results of a collaborative study. *Gastroenterology* **113**, 1146–1158 (1997).
71. Peltomäki, P. & Vasen, H. Mutations associated with HNPCC predisposition-Update of ICG-HNPCC/INSiGHT mutation database. *Dis. Markers* **20**, 269–276 (2004).
72. Samadder, N. J., Jasperson, K. & Burt, R. W. Hereditary and Common Familial Colorectal Cancer: Evidence for Colorectal Screening. *Dig. Dis. Sci.* **60**, 734–747 (2015).
73. Gustavsson, B. *et al.* A review of the evolution of systemic chemotherapy in the management of colorectal cancer. *Clin. Colorectal Cancer* **14**, 1–10 (2015).
74. Heidelberger, C. *et al.* Fluorinated pyrimidines, a new class of tumor-inhibitory

compounds. *Nature* **4561**, 663–666 (1957).

75. Spears, C. P. *et al.* Thymidylate Synthetase Inhibition in Malignant Tumors and Normal Liver of Patients Given Intravenous 5-Fluorouracil. *Cancer Res.* **44**, 4144–4150 (1984).
76. Gmeiner, W. H. Fluoropyrimidine Modulation of the Anti-Tumor Immune Response-Prospects for Improved Colorectal Cancer Treatment. *Cancers (Basel).* **12**, (2020).
77. Shah, M. A. & Schwartz, G. K. Cell cycle-mediated drug resistance: An emerging concept in cancer therapy. *Clin. Cancer Res.* **7**, 2168–2181 (2001).
78. Ullman, B., Lee, M., Martin, D. W. & Santi, D. V. Cytotoxicity of 5-fluoro-2'-deoxyuridine: Requirement for reduced folate cofactors and antagonism by methotrexate. *Proc. Natl. Acad. Sci. U. S. A.* **75**, 980–983 (1978).
79. Keyomarsi, K. K. & Moran, R. G. Folinic Acid Augmentation of the Effects of Fluoropyrimidines on Murine and Human Leukemic Cells. *Cancer Res.* **46**, 5229–5235 (1986).
80. Rustum, Y. M. *et al.* Biochemical and pharmacologic basis for potentiation of 5-fluorouracil action by leucovorin. *NCI Monogr.* **5**, 165–170 (1987).
81. Kunimoto, T. *et al.* Antitumor Activity of 7-Ethyl-10-[4-(1-piperidino)-1-piperidino]carbonyloxy-camptothecin, a Novel Water-Soluble Derivative of Camptothecin, against Murine Tumors. *Cancer Res.* **47**, 5944–5947 (1987).
82. Rivory, L. P. Metabolism of CPT-11: Impact on activity. *Ann. N. Y. Acad. Sci.* **922**, 205–215 (2000).
83. Hsiang, Y. H., Hertzberg, R., Hecht, S. & Liu, L. F. Camptothecin induces protein-linked DNA breaks via mammalian DNA topoisomerase I. *J. Biol. Chem.* **260**, 14873–14878 (1985).
84. Hsiang, Y. H., Lihou, M. G. & Liu, L. F. Arrest of Replication Forks by Drug-stabilized Topoisomerase I-DNA Cleavable Complexes as a Mechanism of Cell Killing by Camptothecin. *Cancer Res.* **49**, 5077–5082 (1989).
85. Saltz, L. *et al.* Irinotecan plus fluorouracil and leucovorin for metastatic colorectal cancer. *N. Engl. J. Med.* **343**, 905–914 (2000).
86. Goldberg, R. M. *et al.* A randomized controlled trial of fluorouracil plus leucovorin, irinotecan, and oxaliplatin combinations in patients with previously untreated metastatic colorectal cancer. *J. Clin. Oncol.* **22**, 23–30 (2004).
87. Colucci, G. *et al.* Phase III randomized trial of FOLFIRI versus FOLFOX4 in the treatment of advanced colorectal cancer: A Multicenter Study of the Gruppo

Oncologico Dell'Italia Meridionale. *J. Clin. Oncol.* **23**, 4866–4875 (2005).

88. Hurwitz, H. *et al.* Bevacizumab plus Irinotecan, Fluorouracil, and Leucovorin for Metastatic Colorectal Cancer. *N. Engl. J. Med.* **23**, 2335–2377 (2004).
89. Van Cutsem, E. *et al.* Cetuximab and Chemotherapy as Initial Treatment for Metastatic Colorectal Cancer. *N. Engl. J. Med.* **360**, 1408–1417 (2009).
90. Van Cutsem, E. *et al.* Cetuximab plus irinotecan, fluorouracil, and leucovorin as first-line treatment for metastatic colorectal cancer: Updated analysis of overall survival according to tumor KRAS and BRAF mutation status. *J. Clin. Oncol.* **29**, 2011–2019 (2011).
91. Stintzing, S. *et al.* FOLFIRI plus cetuximab versus FOLFIRI plus bevacizumab for metastatic colorectal cancer (FIRE-3): a post-hoc analysis of tumour dynamics in the final RAS wild-type subgroup of this randomised open-label phase 3 trial. *Lancet Oncol.* **17**, 1426–1434 (2016).
92. Heinemann, V. *et al.* FOLFIRI plus cetuximab or bevacizumab for advanced colorectal cancer: final survival and per-protocol analysis of FIRE-3, a randomised clinical trial. *Br. J. Cancer* **124**, 587–594 (2021).
93. Longley, D. B., Harkin, D. P. & Johnston, P. G. 5-Fluorouracil: Mechanisms of action and clinical strategies. *Nat. Rev. Cancer* **3**, 330–338 (2003).
94. Warren, N. J. H. & Eastman, A. Comparison of the different mechanisms of cytotoxicity induced by checkpoint kinase I inhibitors when used as single agents or in combination with DNA damage. *Oncogene* **39**, 1389–1401 (2020).
95. Karapetis, C. S. *et al.* K-ras Mutations and Benefit from Cetuximab in Advanced Colorectal Cancer. *N. Engl. J. Med.* **17**, 1757–65 (2008).
96. De Roock, W. *et al.* Effects of KRAS, BRAF, NRAS, and PIK3CA mutations on the efficacy of cetuximab plus chemotherapy in chemotherapy-refractory metastatic colorectal cancer: A retrospective consortium analysis. *Lancet Oncol.* **11**, 753–762 (2010).
97. Rougier, P. *et al.* Randomised trial of irinotecan versus fluorouracil by continuous infusion after fluorouracil failure in patients with metastatic colorectal cancer. *Lancet* **352**, 1407–1412 (1998).
98. Balak, M. N. *et al.* Novel D761Y and Common Secondary T790M Mutations in Epidermal Growth Factor Receptor-Mutant Lung Adenocarcinomas with Acquired Resistance to Kinase Inhibitors. *Clin. Cancer Res.* **12**, 6494–6501 (2006).
99. Ramirez, M. *et al.* Diverse drug-resistance mechanisms can emerge from drug-

tolerant cancer persister cells. *Nat. Commun.* **7**, 1–8 (2016).

100. Poulikakos, P. I. & Solit, D. B. Resistance to MEK Inhibitors: Should We Co-Target Upstream? *Sci. Signal.* **4**, (2011).
101. Mirzoeva, O. K. *et al.* Basal Subtype and MAPK/ERK Kinase (MEK)-Phosphoinositide 3-Kinase Feedback Signaling Determine Susceptibility of Breast Cancer Cells to MEK Inhibition. *Cancer Res.* **69**, 565–572 (2009).
102. Kapoor, A. *et al.* Yap1 Activation Enables Bypass of Oncogenic Kras Addiction in Pancreatic Cancer. *Cell* **158**, 185–197 (2014).
103. Liau, B. B. *et al.* Adaptive Chromatin Remodeling Drives Glioblastoma Stem Cell Plasticity and Drug Tolerance. *Cell Stem Cell* **20**, 233–246 (2017).
104. Hata, A. N. *et al.* Tumor cells can follow distinct evolutionary paths to become resistant to epidermal growth factor receptor inhibition. *Nat. Med.* **22**, 262–269 (2016).
105. Sharma, S. V. *et al.* A Chromatin-Mediated Reversible Drug-Tolerant State in Cancer Cell Subpopulations. *Cell* **141**, 69–80 (2010).
106. Pisco, A. O. & Huang, S. Non-genetic cancer cell plasticity and therapy-induced stemness in tumour relapse: 'What does not kill me strengthens me'. *Br. J. Cancer* **112**, 1725–1732 (2015).
107. Erlanson, D. A. & Webster, K. R. Targeting mutant KRAS. *Curr. Opin. Chem. Biol.* **62**, 101–108 (2021).
108. Ostrem, J. M., Peters, U., Sos, M. L., Wells, J. A. & Shokat, K. M. K-Ras(G12C) inhibitors allosterically control GTP affinity and effector interactions. *Nature* **503**, 548–551 (2013).
109. Hong, D. S. *et al.* KRASG12C Inhibition with Sotorasib in Advanced Solid Tumors. *N. Engl. J. Med.* **383**, 1207–1217 (2020).
110. Dunnett-Kane, V., Nicola, P., Blackhall, F. & Lindsay, C. Mechanisms of Resistance to KRAS G12C Inhibitors. *Cancers (Basel).* **13**, (2021).
111. Misale, S. *et al.* Blockade of EGFR and MEK intercepts heterogeneous mechanisms of acquired resistance to Anti-EGFR therapies in colorectal cancer. *Sci. Transl. Med.* **6**, (2014).
112. Verissimo, C. S. *et al.* Targeting mutant RAS in patient-derived colorectal cancer organoids by combinatorial drug screening. *Elife* **5**, (2016).
113. Lieu, C. H. *et al.* A Phase Ib Dose-Escalation Study of the Safety, Tolerability, and Pharmacokinetics of Cobimetinib and Duligotuzumab in Patients with Previously

Treated Locally Advanced or Metastatic Cancers with Mutant KRAS. *Oncologist* **22**, (2017).

114. Shimizu, T. *et al.* Clinical The Clinical Effect of the Dual-Targeting Strategy Involving PI3K/AKT/mTOR and RAS/MEK/ERK Pathways in Patients with Advanced Cancer. *Clin Cancer Res* **18**, 2316–2325 (2012).
115. Massó-Vallés, D. & Soucek, L. Blocking Myc to Treat Cancer: Reflecting on Two Decades of Omomyc. *Cells* **9**, 1–19 (2020).
116. Savino, M. *et al.* The action mechanism of the Myc inhibitor termed Omomyc may give clues on how to target Myc for cancer therapy. *PLoS One* **6**, (2011).
117. Soucek, L. *et al.* Inhibition of Myc family proteins eradicates KRas-driven lung cancer in mice. *Genes Dev.* **27**, 504–513 (2013).
118. Annibali, D. *et al.* Myc inhibition is effective against glioma and reveals a role for Myc in proficient mitosis. *Nat. Commun.* **5**, 1–11 (2014).
119. Sodir, N. M. *et al.* MYC instructs and maintains pancreatic adenocarcinoma phenotype. *Cancer Discov.* **10**, 588–607 (2020).
120. Sansregret, L. & Swanton, C. The Role of Aneuploidy in Cancer Evolution. *Cold Spring Harb. Perspect Med* **7**, 1–17 (2017).
121. Willems, E. *et al.* The functional diversity of Aurora kinases: a comprehensive review. *Cell Div.* **13**, 1–17 (2018).
122. Tanaka, M. *et al.* Cell-cycle-dependent Regulation of Human aurora A Transcription Is Mediated by Periodic Repression of E4TF1. *J. Biol. Chem.* **277**, 10719–10726 (2002).
123. Hutterer, A. *et al.* Mitotic Activation of the Kinase Aurora-A Requires Its Binding Partner Bora. *Dev. Cell* **11**, 147–157 (2006).
124. Hirota, T. *et al.* Aurora-A and an interacting activator, the LIM protein Ajuba, are required for mitotic commitment in human cells. *Cell* **114**, 585–598 (2003).
125. Katayama, H., Sasai, K., Kloc, M., Brinkley, B. R. & Sen, S. Aurora kinase-A regulates kinetochore/chromatin associated microtubule assembly in human cells. *Cell Cycle* **7**, 2691–2704 (2008).
126. Tsai, M.-Y. *et al.* A Ran signalling pathway mediated by the mitotic kinase Aurora A in spindle assembly. *Nat. Cell Biol.* **5**, 242–248 (2003).
127. Eyers, P. A., Erikson, E., Chen, L. G. & Maller, J. L. A novel mechanism for activation of the protein kinase Aurora A. *Curr. Biol.* **13**, 691–697 (2003).
128. Zorba, A. *et al.* Molecular mechanism of Aurora A kinase autophosphorylation and

its allosteric activation by TPX2. *Elife* **3**, 2667 (2014).

129. Floyd, S., Pines, J. & Lindon, C. APC/CCdh1 Targets Aurora Kinase to Control Reorganization of the Mitotic Spindle at Anaphase. *Curr. Biol.* **18**, 1649–1658 (2008).
130. Min, M., Mayor, U. & Lindon, C. Ubiquitination site preferences in anaphase promoting complex/ cyclosome (APC/C) substrates. *Open Biol* **3**, (2013).
131. den Hollander, J. *et al.* Aurora kinases A and B are up-regulated by Myc and are essential for maintenance of the malignant state. *Blood* **116**, 1498–1505 (2010).
132. Lu, L. *et al.* Aurora kinase A mediates c-Myc's oncogenic effects in hepatocellular carcinoma. *Mol. Carcinog.* **54**, 1467–1479 (2015).
133. Dauch, D. *et al.* A MYC-aurora kinase A protein complex represents an actionable drug target in p53-altered liver cancer. *Nat. Med.* **22**, 744–753 (2016).
134. Li, Y. *et al.* C-Myc Is a Major Determinant for Antitumor Activity of Aurora A Kinase Inhibitor MLN8237 in Thyroid Cancer. *Thyroid* **28**, 1642–1654 (2018).
135. Bischoff, J. R. *et al.* A homologue of Drosophila aurora kinase is oncogenic and amplified in human colorectal cancers. *EMBO J.* **17**, 3052–3065 (1998).
136. Zhou, H. *et al.* Tumour amplified kinase STK15/BTAK induces centrosome amplification, aneuploidy and transformation. *Nat. Genet.* **20**, 189–193 (1998).
137. Sen, S., Zhou, H. & White, R. A. A putative serine/threonine kinase encoding gene BTAK on chromosome 20q13 is amplified and overexpressed in human breast cancer cell lines. *Oncogene* **14**, 2195–2200 (1997).
138. Tanaka, T. *et al.* Centrosomal Kinase AIK1 Is Overexpressed in Invasive Ductal Carcinoma of the Breast. *Cancer Res.* **59**, 2041–2044 (1999).
139. Aradottir, M. *et al.* Aurora A is a prognostic marker for breast cancer arising in BRCA2 mutation carriers. *J. Pathol. Clin. Res.* **1**, 33–40 (2015).
140. Koh, H. M. *et al.* Aurora kinase A is a prognostic marker in colorectal adenocarcinoma. *J. Pathol. Transl. Med.* **51**, 32–39 (2017).
141. Wang, J. *et al.* Aurora-A as an independent molecular prognostic marker in gastric cancer. *Oncol. Rep.* **26**, 23–32 (2011).
142. Liu, Z.-G. *et al.* Aurora-A is an efficient marker for predicting poor prognosis in human nasopharyngeal carcinoma with aggressive local invasion: 208 cases with a 10-year follow-up from a single institution. *Oncol. Lett.* **3**, 1237–1244 (2012).
143. Hoar, K. *et al.* MLN8054, a Small-Molecule Inhibitor of Aurora A, Causes Spindle Pole and Chromosome Congression Defects Leading to Aneuploidy. *Mol. Cell. Biol.* **27**, 4513–4525 (2007).

144. Liu, Q. *et al.* Aurora-A Abrogation of p53 DNA Binding and Transactivation Activity by Phosphorylation of Serine 215. *J. Biol. Chem.* **279**, 52175–52182 (2004).

145. Katayama, H. *et al.* Phosphorylation by aurora kinase A induces Mdm2- mediated destabilization and inhibition of p53. *Nat. Genet.* **36**, 55–62 (2004).

146. Xia, Z. *et al.* AURKA Governs Self-Renewal Capacity in Glioma-Initiating Cells via Stabilization/Activation of b-catenin/Wnt Signaling. *Mol. Cancer Res.* **11**, 1101–1111 (2013).

147. Jacobsen, A. *et al.* Aurora kinase A (AURKA) interaction with Wnt and Ras-MAPK signalling pathways in colorectal cancer. *Sci. Rep.* **8**, 1–11 (2018).

148. Dar, A. A., Belkhiri, A. & El-Rifai, W. The aurora kinase A regulates GSK-3β in gastric cancer cells. *Oncogene* **28**, 866–875 (2009).

149. Meraldi, P., Honda, R. & Nigg, E. A. Aurora-A overexpression reveals tetraploidization as a major route to centrosome amplification in p53-/- cells. *EMBO J.* **21**, 483–492 (2002).

150. Zhang, D. *et al.* Aurora A overexpression induces cellular senescence in mammary gland hyperplastic tumors developed in p53-deficient mice. *Oncogene* **27**, 4305–4314 (2008).

151. Chen, S. S., Chang, P. C., Cheng, Y. W., Tang, F. M. & Lin, Y. S. Suppression of the STK15 oncogenic activity requires a transactivation-independent p53 function. *EMBO J.* **21**, 4491–4499 (2002).

152. Nikonova, A. S., Astsaturov, I., Serebriiskii, I. G., Dunbrack, R. L. & Golemis, E. A. Aurora A kinase (AURKA) in normal and pathological cell division. *Cell. Mol. Life Sci.* **70**, 661–687 (2013).

153. Sells, T. B. *et al.* MLN8054 and Alisertib (MLN8237): Discovery of Selective Oral Aurora A Inhibitors. *ACS Med. Chem. Lett.* **6**, 630–634 (2015).

154. Brockmann, M. *et al.* Small Molecule Inhibitors of Aurora-A Induce Proteasomal Degradation of N-Myc in Childhood Neuroblastoma. *Cancer Cell* **24**, 75–89 (2013).

155. Gustafson, W. C. *et al.* Drugging MYCN through an Allosteric Transition in Aurora Kinase A. *Cancer Cell* **26**, 414–427 (2014).

156. Brunner, A. M. *et al.* Alisertib plus induction chemotherapy in previously untreated patients with high-risk, acute myeloid leukaemia: a single-arm, phase 2 trial. *Lancet Haematol.* **7**, e122–e133 (2020).

157. O'Connor, O. A. *et al.* Randomized phase III study of alisertib or investigator's choice (selected single agent) in patients with relapsed or refractory peripheral T-cell

lymphoma. *J. Clin. Oncol.* **37**, 613–623 (2019).

158. Matulonis, U. A. *et al.* Phase II study of MLN8237 (alisertib), an investigational Aurora A kinase inhibitor, in patients with platinum-resistant or -refractory epithelial ovarian, fallopian tube, or primary peritoneal carcinoma. *Gynecol. Oncol.* **127**, 63–69 (2012).
159. Friedberg, J. W. *et al.* Phase II Study of Alisertib, a Selective Aurora A Kinase Inhibitor, in Relapsed and Refractory Aggressive B-and T-Cell Non-Hodgkin Lymphomas. *J. Clin. Oncol.* **32**, 44–50 (2014).
160. Barr, P. M. *et al.* Phase II Intergroup Trial of Alisertib in Relapsed and Refractory Peripheral T-Cell Lymphoma and Transformed Mycosis Fungoides: SWOG 1108. *J Clin Oncol* **33**, 2399–2404 (2015).
161. Melichar, B. *et al.* Safety and activity of alisertib, an investigational aurora kinase A inhibitor, in patients with breast cancer, small-cell lung cancer, non-small-cell lung cancer, head and neck squamous-cell carcinoma, and gastro-oesophageal adenocarcinoma: a fi ve-arm phase 2 study. *Artic. Lancet Oncol* **16**, 395–405 (2015).
162. Fujii, M. *et al.* A Colorectal Tumor Organoid Library Demonstrates Progressive Loss of Niche Factor Requirements during Tumorigenesis. *Cell Stem Cell* **18**, 827–838 (2016).
163. Van De Wetering, M. *et al.* Prospective derivation of a living organoid biobank of colorectal cancer patients. *Cell* **161**, 933–945 (2015).
164. Rausch, V. & Hansen, C. G. The Hippo Pathway, YAP/TAZ, and the Plasma Membrane. *Trends Cell Biol.* **30**, 32–48 (2020).
165. Schutgens, F. & Clevers, H. Human Organoids: Tools for Understanding Biology and Treating Diseases. *Annu. Rev. Pathol. Mech. Dis.* **15**, 211–234 (2020).
166. Drost, J. & Clevers, H. Organoids in cancer research. *Nat. Rev. Cancer* **18**, 407–418 (2018).
167. Fujii, M., Matano, M., Nanki, K. & Sato, T. Efficient genetic engineering of human intestinal organoids using electroporation. *Nat. Protoc.* **10**, 1474–1485 (2015).
168. Sachs, N. *et al.* A Living Biobank of Breast Cancer Organoids Captures Disease Heterogeneity. *Cell* **172**, 373–386 (2018).
169. Dekkers, J. F. *et al.* Long-term culture, genetic manipulation and xenotransplantation of human normal and breast cancer organoids. *Nat. Protoc.* **16**, 1936–1965 (2021).
170. Boj, S. F. *et al.* Organoid models of human and mouse ductal pancreatic cancer. *Cell* **160**, 324–338 (2015).

171. Neal, J. T. *et al.* Organoid Modeling of the Tumor Immune Microenvironment. *Cell* **175**, 1972–1988 (2018).
172. Dijkstra, K. K. *et al.* Generation of Tumor-Reactive T Cells by Co-culture of Peripheral Blood Lymphocytes and Tumor Organoids. *Cell* **174**, 1586–1598 (2018).
173. Ooft, S. N. *et al.* Patient-derived organoids can predict response to chemotherapy in metastatic colorectal cancer patients. *Sci. Transl. Med.* **11**, 1–10 (2019).
174. Camp, R. L., Rimm, E. B. & Rimm, D. L. Met expression is associated with poor outcome in patients with axillary lymph node negative breast carcinoma. *Cancer* **86**, 2259–2265 (1999).
175. Dietinger, V. *et al.* Wnt-driven LARGE2 mediates laminin-adhesive O-glycosylation in human colonic epithelial cells and colorectal cancer. *Cell Commun. Signal.* **18**, 102 (2020).
176. Jung, P. *et al.* Isolation and in vitro expansion of human colonic stem cells. *Nat. Med.* **17**, 1225–1227 (2011).
177. KGaA, M. Western Blot Protocols. https://www.merckmillipore.com/DE/de/life-science-research/protein-detection-quantification/western-blotting/protocols/q9ib.qB.710AAAFBRP0RRkww,nav?ReferrerURL=https%3A%2F%2Fwww.google.com%2F (2021).
178. Landrum, M. J. *et al.* ClinVar: Improving access to variant interpretations and supporting evidence. *Nucleic Acids Res.* **46**, D1062–D1067 (2018).
179. Vosberg, S. *et al.* Close Correlation of Copy Number Aberrations Detected by Next-Generation Sequencing with Results from Routine Cytogenetics in Acute Myeloid Leukemia. *Genes. Chromosomes Cancer* **55**, 553–567 (2016).
180. Rigaill, G. J. *et al.* A regression model for estimating DNA copy number applied to capture sequencing data. *Bioinformatics* **28**, 2357–2365 (2012).
181. Parekh, S., Ziegenhain, C., Vieth, B., Enard, W. & Hellmann, I. The impact of amplification on differential expression analyses by RNA-seq. *Sci. Rep.* **6**, (2016).
182. Macosko, E. Z. *et al.* Highly parallel genome-wide expression profiling of individual cells using nanoliter droplets. *Cell* **161**, 1202–1214 (2015).
183. Love, M. I., Huber, W. & Anders, S. Moderated estimation of fold change and dispersion for RNA-seq data with DESeq2. *Genome Biol.* **15**, (2014).
184. Grossmann, R. L. *et al.* Toward a Shared Vision for Cancer Genomic Data. *N. Engl. J. Med.* **375**, 1109–1112 (2016).
185. Satoh, T. *et al.* Pharmacokinetic assessment of irinotecan, SN-38, and SN-38-

glucuronide: A substudy of the FIRIS study. *Anticancer Res.* **33**, 3845–3854 (2013).

186. Mathijssen, R. H. J. *et al.* Irinotecan pharmacokinetics-pharmacodynamics: The clinical relevance of prolonged exposure to SN-38. *Br. J. Cancer* **87**, 144–150 (2002).
187. Abe, Y. *et al.* Evaluation of the 5-fluorouracil plasma level in patients with colorectal cancer undergoing continuous infusion chemotherapy. *Mol. Clin. Oncol.* **11**, 289–295 (2019).
188. Tan, A. R. *et al.* Pharmacokinetics of cetuximab after administration of escalating single dosing and weekly fixed dosing in patients with solid tumors. *Clin. Cancer Res.* **12**, 6517–6522 (2006).
189. Subramanian, A. *et al.* Gene set enrichment analysis: A knowledge-based approach for interpreting genome-wide expression profiles. *Proc. Natl. Acad. Sci. U. S. A.* **102**, 15545–15550 (2005).
190. Liberzon, A. *et al.* The Molecular Signatures Database Hallmark Gene Set Collection. *Cell Syst.* **1**, 417–425 (2015).
191. Gong, K. *et al.* EGFR inhibition triggers an adaptive response by co-opting antiviral signaling pathways in lung cancer. *Nat. Cancer* **1**, 394–409 (2020).
192. Lu, Y. *et al.* Hypoxia induces resistance to EGFR inhibitors in lung cancer cells via upregulation of FGFR1 and the MAPK pathway. *Cancer Res.* **80**, 4655–4667 (2020).
193. Jing, X. *et al.* Role of hypoxia in cancer therapy by regulating the tumor microenvironment. *Mol. Cancer* **18**, 1–15 (2019).
194. Garraway, L. A. & Jänne, P. A. Circumventing cancer drug resistance in the era of personalized medicine. *Cancer Discov.* **2**, 214–226 (2012).
195. Gottesman, M. M., Lavi, O., Hall, M. D. & Gillet, J. P. Toward a Better Understanding of the Complexity of Cancer Drug Resistance. *Annu. Rev. Pharmacol. Toxicol.* **56**, 85–102 (2016).
196. Zhang, C. *et al.* Copy number increase of aurora kinase A in colorectal cancers: A correlation with tumor progression. *Acta Biochim. Biophys. Sin. (Shanghai).* **42**, 834–838 (2010).
197. Sillars-Hardebol, A. H. *et al.* TPX2 and AURKA promote 20q amplicon-driven colorectal adenoma to carcinoma progression. *Gut* **61**, 1568–1575 (2012).
198. Goos, J. A. C. M. *et al.* Aurora kinase A (AURKA) expression in colorectal cancer liver metastasis is associated with poor prognosis. *Br. J. Cancer* **109**, 2445–2452 (2013).
199. Jung, J. *et al.* Increased expression levels of AURKA and KIFC1 are promising

predictors of progression and poor survival associated with gastric cancer. *Pathol. Res. Pract.* **224**, 153524 (2021).

200. Guo, M. *et al.* Increased AURKA promotes cell proliferation and predicts poor prognosis in bladder cancer. *BMC Syst. Biol.* **12**, 11–17 (2018).
201. Al-Khafaji, A. S. K. *et al.* AURKA mRNA expression is an independent predictor of poor prognosis in patients with non-small cell lung cancer. *Oncol. Lett.* **13**, 4463–4468 (2017).
202. Zhou, X., Wang, P. & Zhao, H. The association between AURKA gene rs2273535 polymorphism and gastric cancer risk in a Chinese population. *Front. Physiol.* **9**, 1–9 (2018).
203. Michl, M. *et al.* Biomarker alterations associated with distinct patterns of metastatic spread in colorectal cancer. *Virchows Arch.* (2020) doi:10.1007/s00428-020-02983-6.
204. Kim, S. K. *et al.* A nineteen gene-based risk score classifier predicts prognosis of colorectal cancer patients. *Mol. Oncol.* **8**, 1653–1666 (2014).
205. Michl, M. *et al.* Expression of cancer stem cell markers in metastatic colorectal cancer correlates with liver metastasis, but not with metastasis to the central nervous system. *Pathol. - Res. Pract.* **211**, 601–609 (2015).
206. Matly, A., Quinn, J. A., McMillan, D. C., Park, J. H. & Edwards, J. The relationship between β-catenin and patient survival in colorectal cancer systematic review and meta-analysis. *Crit. Rev. Oncol. Hematol.* **163**, 103337 (2021).
207. Misale, S. *et al.* Vertical suppression of the EGFR pathway prevents onset of resistance in colorectal cancers. *Nat. Commun.* **6**, (2015).
208. Russo, M. *et al.* Adaptive mutability of colorectal cancers in response to targeted therapies. *Science* **366**, 1473–1480 (2019).
209. van der Flier, L. G. *et al.* Transcription Factor Achaete Scute-Like 2 Controls Intestinal Stem Cell Fate. *Cell* **136**, 903–912 (2009).
210. van der Flier, L. G., Haegebarth, A., Stange, D. E., van de Wetering, M. & Clevers, H. OLFM4 Is a Robust Marker for Stem Cells in Human Intestine and Marks a Subset of Colorectal Cancer Cells. *Gastroenterology* **137**, 15–17 (2009).
211. Zhang, X., Huang, Q., Yang, Z., Li, Y. & Li, C. Y. GW112, A Novel Antiapoptotic Protein That Promotes Tumor Growth. *Cancer Res.* **64**, 2474–2481 (2004).
212. Ohkuma, R. *et al.* High expression of olfactomedin-4 is correlated with chemoresistance and poor prognosis in pancreatic cancer. *Oncol. Rep.* **15**, 252–262

(2020).

213. Davis, E. *et al.* Ectopic Tbx2 expression results in polyploidy and cisplatin resistance. *Oncogene* **27**, 976–984 (2008).
214. Wang, Q., Lu, F. & Lan, R. RNA-sequencing dissects the transcriptome of polyploid cancer cells that are resistant to combined treatments of cisplatin with paclitaxel and docetaxel. *Mol. Biosyst.* **13**, 2125–2134 (2017).
215. Tasaka, R., Fukuda, T., Shimomura, M. & Inoue, Y. TBX2 expression is associated with platinum - sensitivity of ovarian serous carcinoma. *Oncol. Lett.* **15**, 3085–3090 (2018).
216. Lu, J. *et al.* TBX2 Expression predicts Tumor Recurrence and Adjuvant Chemotherapy Benefits in Gastric Cancer Patients following R0 Resection : a proposed approach for risk stratification. *J. Cancer* **11**, 3172–3179 (2020).
217. Zhang, Z. *et al.* Loss of CHD1 Promotes Heterogeneous Mechanisms of Resistance to AR-Targeted Therapy via Chromatin Article Loss of CHD1 Promotes Heterogeneous Mechanisms of Resistance to AR-Targeted Therapy via Chromatin Dysregulation. *Cancer Cell* **37**, 584-598.e11 (2021).
218. Pastor-Anglada, M. & Pérez-Torras, S. Who Is Who in Adenosine Transport. *Front. Pharmacol.* **9**, (2018).
219. Stief, S. M. *et al.* Loss of KDM6A confers drug resistance in acute myeloid leukemia. *Leukemia* **34**, 50–62 (2020).
220. Liu, M. *et al.* ZIP4 Increases Expression of Transcription Factor ZEB1 to Promote Integrin α3β1 Signaling and Inhibit Expression of the Gemcitabine Transporter ENT1 in Pancreatic Cancer Cells. *Gastroenterology* **158**, 679-692.e1 (2020).
221. Hyun, J., Chansu, K., Hyun, L., Cheong, S. & Koh, Y. SLC29A1 (ENT1) polymorphisms and outcome of complete remission in acute myeloid leukemia. *Cancer Chemother. Pharmacol.* **78**, 533–540 (2016).
222. Kugimiya, N. *et al.* The c-MYC-ABCB5 axis plays a pivotal role in 5-fluorouracil resistance in human colon cancer cells. *J. Cell. Mol. Med.* **19**, 1569–1581 (2015).
223. Lee, K. *et al.* MYC and MCL1 Cooperatively Promote Chemotherapy-Resistant Breast Cancer Stem Cells via Regulation of Mitochondrial Oxidative Phosphorylation. *Cell Metab.* **26**, 633–647 (2017).
224. Pyndiah, S. *et al.* c-MYC Suppresses BIN1 to Release Poly(ADP-Ribose) Polymerase 1: A Mechanism by Which Cancer Cells Acquire Cisplatin Resistance. *Sci. Signal.* **4**, (2011).

225. Banck, M. S. & Grothey, A. Biomarkers of resistance to epidermal growth factor receptor monoclonal antibodies in patients with metastatic colorectal cancer. *Clin. Cancer Res.* **15**, 7492–7501 (2009).
226. Carter, C. A. *et al.* Selumetinib with and without erlotinib in KRAS mutant and KRAS wild-type advanced nonsmall-cell lung cancer. *Ann. Oncol.* **27**, 693–699 (2016).
227. Hook, K. E. *et al.* An integrated genomic approach to identify predictive biomarkers of response to the Aurora kinase inhibitor PF-03814735. *Mol. Cancer Ther.* **11**, 710–719 (2012).
228. Sun, C. *et al.* Intrinsic resistance to MEK inhibition in KRAS mutant lung and colon cancer through transcriptional induction of ERBB3. *Cell Rep.* **7**, 86–93 (2014).
229. Ebi, H. *et al.* Receptor tyrosine kinases exert dominant control over PI3K signaling in human KRAS mutant colorectal cancers. *J. Clin. Invest.* **121**, 4311–4321 (2011).
230. van Geel, R. M. J. M. *et al.* Phase 1 study of the pan-HER inhibitor dacomitinib plus the MEK1/2 inhibitor PD-0325901 in patients with KRAS-mutation-positive colorectal, non-small-cell lung and pancreatic cancer. *Br. J. Cancer* **122**, 1166–1174 (2020).
231. Huijberts, S. C. F. A. *et al.* Phase I study of lapatinib plus trametinib in patients with KRAS-mutant colorectal, non-small cell lung, and pancreatic cancer. *Cancer Chemother. Pharmacol.* **85**, 917–930 (2020).
232. Shah, K. N. *et al.* Aurora kinase A drives the evolution of resistance to third-generation EGFR inhibitors in lung cancer. *Nat. Med.* **25**, 111–118 (2019).
233. Adhikari, B. *et al.* PROTAC-mediated degradation reveals a non-catalytic function of AURORA-A kinase. *Nat. Chem. Biol.* **16**, 1179–1188 (2020).
234. Lindsey Davis, S. *et al.* Combined inhibition of MEK and Aurora A kinase in KRAS/PIK3CA double-mutant colorectal cancer models. *Front. Pharmacol.* **6**, (2015).
235. Otto, T. *et al.* Stabilization of N-Myc Is a Critical Function of Aurora A in Human Neuroblastoma. *Cancer Cell* **15**, 67–78 (2009).
236. Diaz, L. A. J. *et al.* The molecular evolution of acquired resistance to targeted EGFR blockade in colorectal cancers. *Nature* **486**, 537–540 (2012).
237. Sottoriva, A. *et al.* A Big Bang model of human colorectal tumor growth. *Nat. Genet.* **47**, 209–216 (2015).
238. Roerink, S. F. *et al.* Intra-tumour diversification in colorectal cancer at the single-cell level. *Nature* **556**, 457–462 (2018).

239. Boumahdi, S. & de Sauvage, F. J. The great escape: tumour cell plasticity in resistance to targeted therapy. *Nat. Rev. Drug Discov.* **19**, 39–56 (2020).

10 Acknowledgements

First of all, I would like to thank Dr. Peter Jung for the chance to perform my Ph.D. project in his laboratory. His knowledge, ideas, and experience helped me to shape my project and I learned a lot of new techniques. He introduced me into the world of PDTOs, which I still find fascinating.

I am thankful to Prof. Dr. Hermeking for agreeing to supervise my thesis. In addition, I am grateful for the productive discussions concerning my project during lab meetings and institute seminars.

I am also grateful to Prof. Dr. Kirchner and Prof. Dr. Neumann for their collaboration, which gave us access to patient material for our living biobank of PDTOs as well as the human M0-M1 cohort. Special thanks go out to the Diagnostics Department of the Institute of Pathology, Dr. Kumbrink, and Prof. Dr. Jung for the pyrosequencing and panel sequencing of our samples. Thank you to Dr. Öllinger, Thomas Engleitner, and Prof. Dr. Rad for their collaboration concerning the RNA sequencing. I appreciate the collaboration with Dr. Vosberg and Dr. Greif for the whole exome sequencing analysis. I would also like to thank Dr. Rokavec for the analyses of the public RNA sequencing data sets.

Ursula Götz supported me with protocols and chemicals. Thanks also to the rest of the Hermeking lab not only for support in the lab and ideas during lab meetings but also good times during lunch and coffee breaks. The same goes for my office colleagues from the Ormanns lab: Thank you!

A special thank you goes out to the other members of our group: We always supported each other and had a lot of fun. Vanessa Dietinger who was there from the start: I am glad we complemented each other so well. Dr. Cira García de Durango brought her cheerfulness and knowledge with her into the lab. Finally, our lab was completed by Leon who I could always count on.

Additionally, I would like to thank my friends, especially These, my parents and sister, as well as my husband for all the love, support, and motivation during my Ph.D.